5-2015

Characterization of Silicon Phosphorus Alloy for Device Applications

Larry C. Cousar
University of Arkansas, Fayetteville

Characterization of Silicon Phosphorus Alloy for Device Applications

Characterization of Silicon Phosphorus Alloy for Device Applications

A thesis submitted in partial fulfillment
of the requirements for the degree of
Master of Science in Microelectronics-Photonics

by

Larry Cousar
University of Arkansas
Bachelor of Science in Electrical Engineering, 2013

May 2015
University of Arkansas

This thesis is approved for recommendation to the Graduate Council.

_____
Dr. Hameed A. Naseem
Thesis Director

_____
Dr. Shui-Qing (Fisher) Yu
Committee Member

_____
Dr. Gregory Salamo
Committee Member

_____
Dr. Rick Wise
Ex-Officio Member

The following signatories attest that all software used in this thesis was legally licensed for use by Larry Cousar for research purposes and publication.

_____   _____

Mr. Larry Cousar   Dr. Hameed A. Naseem, Thesis Director

This thesis was submitted to http://www.turnitin.com for plagiarism review by the TurnItIn company's software. The signatories have examined the report on this thesis that was returned by TurnItIn and attest that, in their opinion, the items highlighted by the software are incidental to common usage and are not plagiarized material.

_____   _____

Dr. Rick Wise, Program Director   Dr. Hameed A. Naseem, Thesis Director

Abstract

A new material of highly-phosphorus doped silicon for device applications was characterized and analyzed for new material properties. Devices such as NMOS transistors and other CMOS compatible devices may benefit from new materials that reduce external resistances and increase drive currents.

Material characterization requires numerous techniques and technologies to determine electrical, optical, and physical characteristics. For this work, Hall measurement, X-ray Diffraction, Raman Spectroscopy, Photoluminescence Characterization, and Spectroscopic Ellipsometry were used to better understand this new material. The results may lead to new models for silicon phosphorus alloys.

Acknowledgments

Ghetmiri's leadership and example, as well as his technical instruction and his extreme honorable respect for people, caused me to achieve even more. Mr. Yiyin Zhou gave countless time for training on Hall measurement, class tutoring, and thesis preparation. Mr. Omar Alzoubi made possible many learning experiences with computer modeling software and great discussions on electromagnetics. Mr. Khaled Al-Shurman provided superb instruction on IC technology and was always encouraging to achieve more than I thought I could achieve. Ms. Huong Tran gave much effort to ensure the reliability of the Hall measurement system and was helpful with the learning of spectroscopic ellipsometry.

Some research was made possible through the use of the High-Density Electronics Center at the University of Arkansas, Fayetteville campus, and all the staff made every effort to ensure great experiences in the lab. Dr. Vasyl Kunets was instrumental in recognizing many obstacles that came with Hall measurements. His training and regular discussions increased confidence in the Hall measurement results. And finally, all the other students not listed that in some way added to the great experience of this work.

A special group of people who had little knowledge of my thesis yet impacted the outcome greatly must be mentioned. Dr. Michael Hendren was at one time the only one outside of academics that pointed me in the direction of such great academic success. Dr. Susan Shackelford provided an education greater than even this thesis work. Dr. Angela Chapman brought the greatest of inspirations. My son Josh, from whom I cannot express the incredible encouragement I received that went far beyond that of a son, lit a parallel path of progress and achievement while consistently encouraging my success.

Dedication

This work is dedicated to all my family; my mother, who's love, care, and concern never ceases; my siblings who help me find my way; and my two sons, Josh and Kory. These two men I am the proudest.

Table of Contents

List of Figures

List of Tables

1. Introduction

1.1. Area of Research

The progression of science and technology continues at a record pace. Many technology modalities driving the record pace are communications, healthcare, military and extraterrestrial research. Each of these depend on the current electronic technology that had its beginning in the middle 20th century with the invention of the transistor, the foundational device made from semiconductors.

Semiconductors are the materials that give the transistor its properties. Electronics depend on three primary types of materials. First, conductors allow the free flow of electricity and are normally made from metals such as aluminum, copper, gold, or tin to name a few. Second, insulators restrict the flow of electricity and are made from materials such as plastics, glass, ceramics or rubber. Third, semiconductors are materials that fall in between conductors and insulators. Although not a perfect conductor or insulator, this special property makes electronic technology possible.

The innovations that followed the invention of the transistor required a decade of research and improvements before a substantial growth rate was observed. Improvements in materials and processes along with cost reductions were the key factors driving growth. These improvements enabled the invention of the integrated circuit, a device that incorporates transistors and other electronic components in one package.

Integrated circuits were innovative, but the real innovation came by increasing the number of components on the integrated circuit. By the middle 1960's, Gordon Moore observed that the number of components on an integrated circuit would double approximately every two years. This observation continued with such accuracy that industry leaders and experts across the

globe began using the observation to plan future research directions. This observation became known as "Moore's Law".

Moore's Law consistently followed the growth trend for more than forty years as innovation continued to drive down the size of components. Although each decade experts would predict an end to the observation due to technology limits within ten years, breakthroughs always occurred. Now, a physical limit is approaching that cannot be overcome. Features within the integrated circuit are approaching sizes near the wavelength of the electron itself, the fundamental particle that gives all electronics the ability to perform the designed function. Prior to this limit, quantum effects such as electron tunneling will likely disable the technology. The trend as it relates to feature size is shown in Figure 1.1.
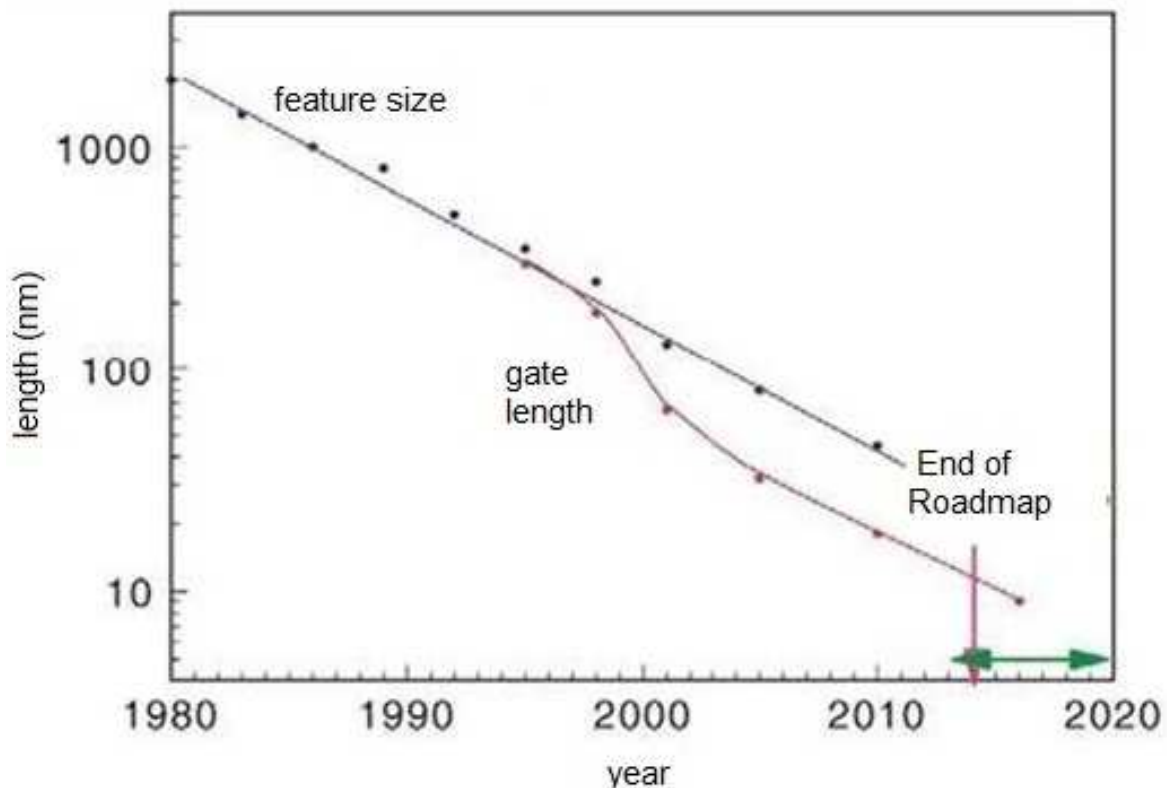
Figure 1:1: Moore's Law [1]

Complementary Metal Oxide Semiconductors (CMOS) is the dominant technology used to construct integrated circuits. Innovations in this technology have made possible the feature size reductions that enable increased number of transistors on the integrated circuit. The feature size is characterized by the minimum line width of the lateral dimension in the integrated circuit.

The current CMOS technology requires greater than 100 process steps for the construction of particular integrated circuits. Many aspects of integrated circuit technology are being researched to continue improvements of doubling of information speed that previously had occurred about every two years through process and material enhancements such as new materials to improve carrier mobility. Silicon Germanium materials [2] were introduced into CMOS technology for the improvement of carrier mobility and other device enhancements. New materials of highly phosphorus doped silicon are being considered for similar uses. [2] It has been shown that phosphorus concentrations above 3 x 10^{20} cm^{-3}are needed to induce strain for mobility enhancements. [3] Moreover, as CMOS technology approaches the 22 nm process node, the "series resistance component for nMOS would be higher than the channel on resistance and hence becomes the performance limiter". [3]

Creating new materials for CMOS technology presents new challenges not yet overcome. To understand some of these challenges, a solid understanding of the foundational material, silicon, is required.

Silicon is the second most plentiful element in the earth's crust which is clearly one of the driving factors in the proliferation of electronic technology. Because of this, it is the most researched and refined element for all electronics. Once purified and refined to its crystalline state for CMOS technology, silicon takes on the diamond lattice crystalline form. An example is shown in Figure 1.2.
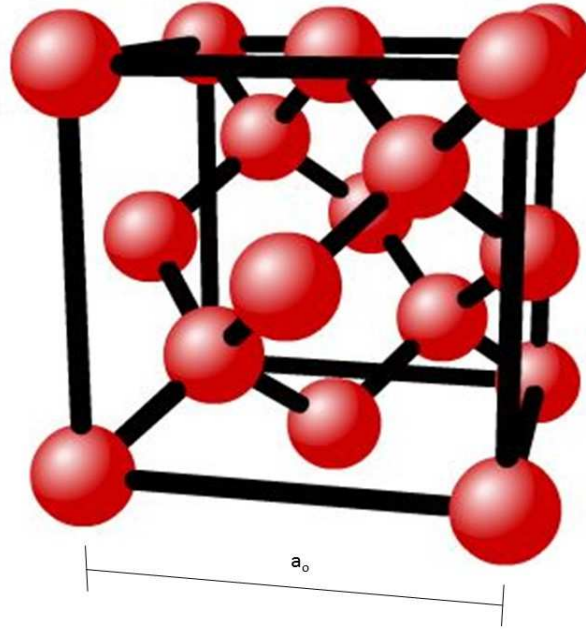
Figure 1:2: Silicon Crystal Lattice [5]

The lattice constant, shown as a_o, for silicon in the diamond lattice crystalline form is 0.5431 nanometers (nm). This lattice is characterized by four covalently bonded atoms within the unit cell with each atom spaced $\frac{\sqrt{3}}{4} a_o$ apart. There are four atoms that are completely inside the unit cell. There are eight atoms at each corner of the unit cell that are each shared with seven other cells thereby making these eight atoms count as one atom. There are six face-centered atoms that are each shared with one other cell and thereby counting as three atoms within the cell. This makes the total number of atoms in one unit cell equal to eight atoms.

The cell volume for any crystal lattice is $(a_o)^3$. For silicon, this equates to 1.6×10^{-22} cm^3. The density of silicon atoms is (atoms per unit cell) / (cell volume) which equates to 5×10^{22} atoms/cm^3. The solid solubility limit of phosphorus in silicon using traditional growth methods is 1.7×10^{21}/cm^3 as indicated in Figure 1.3. This limit equates to 3.4 atomic percent (a.t. %) incorporation as shown in the relation in Equation 1.1.

4

Atomic % = (Number of Atoms of Element) / (Density of atoms) * 100

$$= (1.7 \times 10^{21}) / (5 \times 10^{22}) * 100 = 3.4\% \qquad \text{(Equation 1.1)}$$
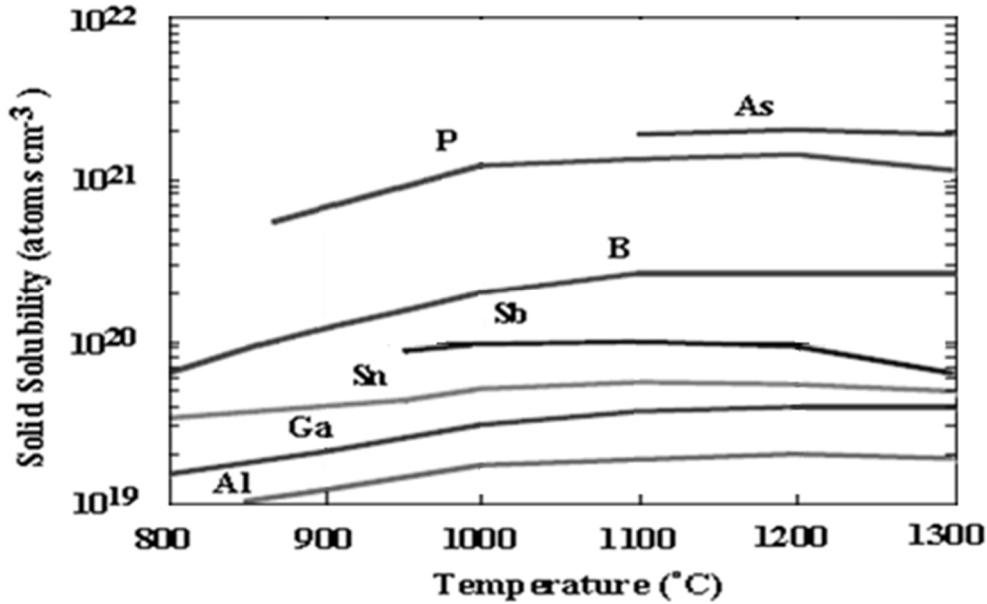
Figure 1:3: Solid Solubility Limits [7]

Phase segregation would normally occur beyond this limit and would make for a useless material in electronic technology. It has been shown that phosphorus can be added in concentrations up to 12 a.t. % using specialized techniques. [4] Moreover, high concentrations can increase tensile strain for improved carrier mobility and reduce resistivity.

ASM America generated Si:P epitaxial films using the ASM EpsilonTM 300 mm chemical vapor deposition system. The films were deposited on silicon (100) substrates with traditional precursors of $SiCl_2H_2$ – Dichlorosilane (DCS) for silicon and PH_3-Phosphine for the phosphorus dopant at temperatures between 600 and 700°C and process pressures between 1.33 and 101 kPa.[6] The films deposited ranged in compositions of phosphorus from one to twelve atomic percent. Samples acquired from ASM America for this work were produced using similar processes, precursors, and techniques.

1.2. Research Goals

The search for new materials that benefit CMOS technology and propel the so-called "Moore's Law" is an area of much research. The use of silicon phosphide alloys takes advantage of current materials in industry which make them more likely to be incorporated into current technology streams. It has been widely known that increasing dopants in semiconductors can reduce resistivity, a benefit that may be significant, as scaling of devices will lead to a greater need for reduced contact resistances and a reduction in current density. Increasing dopants beyond the standard solid solubility limit, though, has previously had little success as poor material quality prevails.

The highly-phosphorus doped crystalline silicon films currently being produced in research facilities raise several questions of importance. The assessment of material quality may determine the viability of such materials. In the assessment of material quality, a basic understanding of the molecular structure would seem to be of great importance. Is this material SiP, SiP_2, or some other molecular structure? Are the high phosphorus concentration films high-quality crystalline films or are there substantial precipitates? What are the electrical and optical properties of this material? These questions define the research goals of this work.

2. Literature Review

Material characterization has been an important part of electronic technology from the early days of the transistor invention. Those directly involved with the invention also had an influence on many areas of material research that continue to drive new technologies today. Particularly, the effects of mechanical strain on semiconductor crystals were first experimentally shown by C. Smith in 1954 in his paper titled "Piezo resistance effect in germanium and silicon". [8] Smith detailed the effects uniaxial tensile strain has on resistance through either charge mobility or charge carrier concentration changes. Strain engineering continues to be useful in current CMOS technology. It has been shown that mobility enhancements by strain engineering have played an important role in the reduction of external resistances below the 45 nm technology node will become paramount. [9] Simple discoveries such as piezo resistance can continue to push technology forward for decades.

The material characterization of electronic materials requires more expertise to identify effects of strain engineering as structure sizes in complementary metal oxide semiconductor (CMOS) technology continue to reduce. Characterization technology is utilized at every step of semiconductor research and development, and future technology progression will depend upon it. One of the greatest challenges to future technology is the quality of electrical contacts. This is a factor in every area of electronic manufacturing areas such as CMOS and power driven technologies like photovoltaic cells. [10]

The applications previously mentioned require innovations to move forward the current technology. The foundational CMOS technology has many obstacles for continued increased speed as has been predicted by Moore's Law. Driving down feature sizes present many complications. Two of the greatest of these are the increased resistivity that occurs in the

contacts made and the parasitic resistance that occurs in the source and drain of CMOS devices.

Cross sections of CMOS devices are shown in Figures 2.1 and 2.2.

Figure 2:2: CMOS Transistor Technology
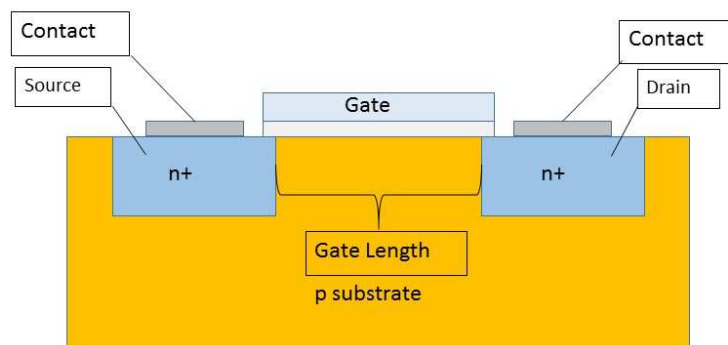
Figure 2:1: n-MOS Transistor

The contact resistance of CMOS devices is given in units of $\Omega \bullet cm^2$. This unit identifies the influence the area of the contact has on the resistance. As the area is reduced, the contact resistance will increase. As feature sizes continue to reduce in CMOS technology, the contact resistance will become an even greater parameter of concern.

The primary method of reducing contact resistance in CMOS technology has been to increase doping density. As the doping density is increased, more free carriers are produced which reduce resistance. The increase of free carriers occurs only to a certain level. This level presents another obstacle to reducing contact resistance. For phosphorus, the concentration profile and the carrier concentration result of doping are shown in Figure 2.3. The result shown indicates a carrier saturation density of $n_c \approx 2.68 \times 10^{20}$ cm^{-3}. With this limit, there is a limit as to how much phosphorus doping can be achieved with current technology.
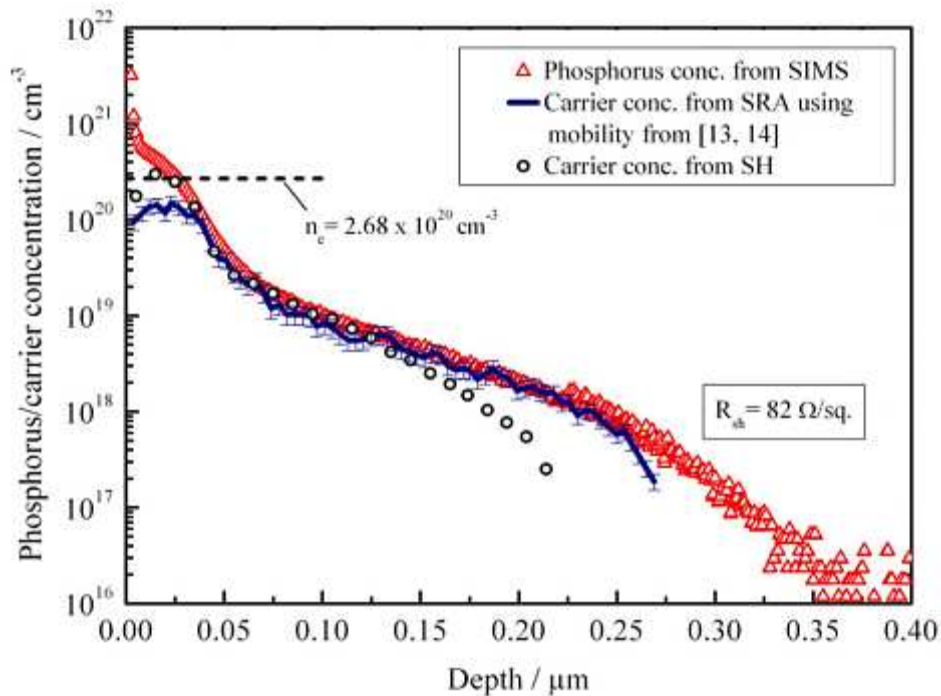
Figure 2:3: Phosphorus/Carrier Concentration Profile [10]

One method of material growth that has seen an increase in use for high-volume manufacturing is low-pressure chemical vapor deposition (LPCVD). This method uses precursor gases flown into a low-pressure chamber that leads to the material being deposited on substrates. This method can be used for deposition of doped materials using precursors such as silane and phosphine. An example of an LPCVD chamber is shown in Figure 2.4.
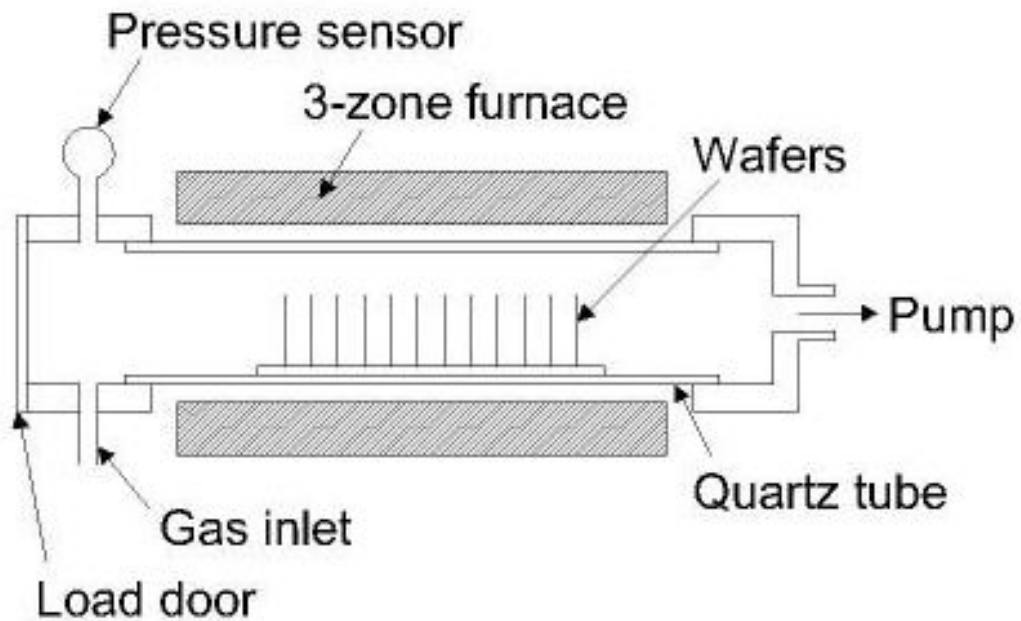
Figure 2:4: LPCVD Chamber [11]

3. Experimental Design

3.1. Experimental Design Introduction

The experimental plan was devised to explore many optical and electrical characteristics of the phosphorous doped silicon material. There were thirty-one samples acquired from ASM America, Inc. that ranged in phosphorus concentrations from 0.23% to 10.35%. These samples were received in quarter-sections of 8 inch wafers.

The first characterization to be considered was Hall measurement to acquire the resistivity, carrier density, and Hall mobility. The second characterization used was X-Ray diffraction analysis (XRD). The primary technique used for XRD was the coupled scan, two theta omega. Following the XRD characterization, the electrochemical capacitance-voltage profiling was investigated. It was discovered that this characterization was primarily used on samples greater in thickness than 500 nm.

Raman Spectroscopy characterizations were the next tool used to investigate the material qualities of the samples. Spectroscopic ellipsometry characterizations followed to determine some of the optical properties of the samples. Photoluminescence characterization of the samples followed next and finally, the samples were used to simulate and fabricate and characterize a device.

The characterizations in the experimental design were an attempt to learn as many physical properties of the samples as possible to better understand and possibly suggest new applications for such materials. The samples are a thin layer of highly phosphorus doped silicon on a p-type substrate. Together, these two form a p-n junction with emitter depths ranging from 12 nm to more than 200 nm. This p-n junction could be used to construct a device and

characterize it to discover even more about this new material. For this work, it was decided to simulate, fabricate, and characterize a solar cell using the samples.

The first step in the experimental design was to label the samples in a format that simplified the tracking of data and experiments. The lowest phosphorus concentration sample was labeled P1 followed by the next higher concentration sample labeled with P2. This was continued for all samples to the final, P31. The preliminary plan was to select seven samples from across the concentration spectrum. The initial samples selected are listed in Table 2.

Table 1: Initial Wafers Selected

Wafer Number	% Phosphorous Concentration
P10	1.96
P20	5.83
P21	6.13
P22	6.34
P26	7.01
P27	7.20
P31	10.35

The next step for the experimental design was to prepare the samples for characterizations. The large quarter-sections required cleaving sample sizes to two centimeters by two centimeters. It was decided to identify the cleaved samples by the location on the original quarter-section in the event that uniformity across the wafer was to be considered. This

requirement was met by the following labeling format of the quarter-section wafer as shown in Figure 3.1.
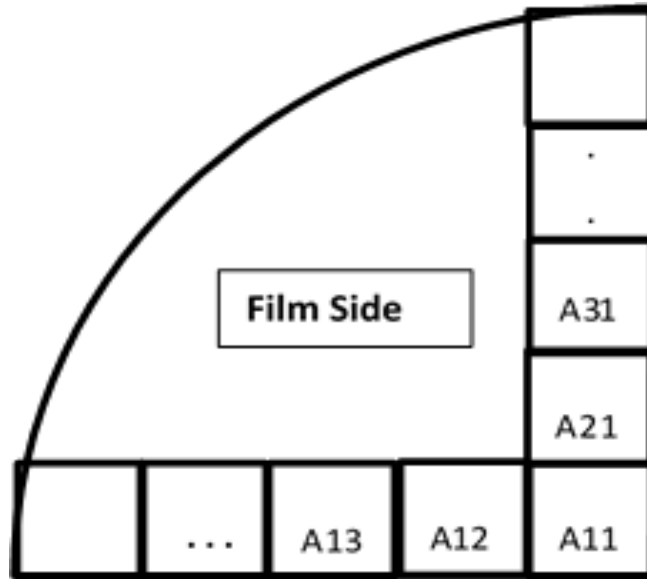
Figure 3:1: Sample Label

The labeling of the samples would then be identified along with the sections shown in Figure 3.1, e.g. P1A11. Some characterizations, such as photoluminescence, required sample sizes of five millimeter by five millimeter. In this case, the two centimeter by two centimeter sample was cleaved to the proper size without further distinction in labeling.

3.2. Hall Measurement Characterization

The Hall measurement is made possible by the Lorentz force. The Lorentz force is the force a moving charge experiences in the presence of a magnetic field. This force is given by the Equation 3.1.

$$F_{lorentz} = -q \cdot v \times \mathbf{B},$$
(Equation 3.1)

In this equation, q is the moving charge, v is the velocity of the charge and **B** is the magnetic field. The vector cross product makes the force on the charge perpendicular to the charge's velocity and to the magnetic field that the charge is moving through. Applying this concept to the flow of current through a semiconductor, the Lorentz force will cause the flow of current through the semiconductor to build up excess negative charges of electrons on one side of the semiconductor. Similarly, hole flow in the opposite direction will cause excess positive charges to accumulate on the opposite side of the semiconductor due to the Lorentz force. This buildup of charges will produce a net potential difference and is called the Hall voltage, V_H. The concept of the Hall voltage measurement is shown in Figure 3.2.
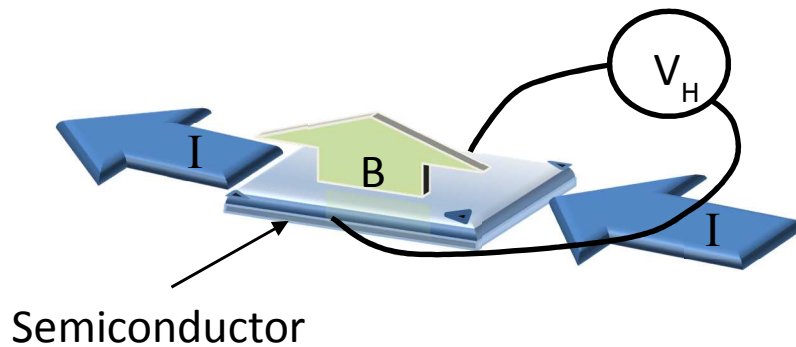
Figure 3:2: Hall Voltage Measurement Concept

The magnitude of the Hall voltage is given by Equation 3.2.

$$|V| = I * B / (q * n_{s)}$$ (Equation 3.2)

In Equation 3.2, I is the current, B is the magnetic field, q is the elementary charge, and n_s is the sheet density. The polarity of the Hall voltage can determine the material type, *n* or *p*. For the configuration shown in Figure 3.3, if the Hall voltage V_{24} is negative for a current I_{12} injected into contact 1, the semiconductor is *n*-type. If the Hall voltage is positive, the semiconductor is *p*-type.

The sheet density of the carriers which is defined as the number of electrons multiplied by the thickness of the layer. If the layer thickness d is known, the bulk density n can be calculated using Equation 3.2.
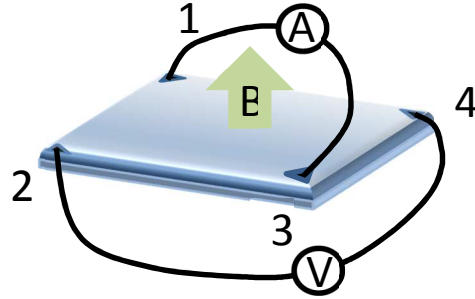
Figure 3:3: Hall Voltage Measurement

$$n = n_s / d \qquad \text{(Equation 3.3)}$$

The Hall voltage can be used to solve for the sheet density by the following relation given in Equation 3.3.

$$n_s = I * B / (q * |V|) \qquad \text{(Equation 3.4)}$$

Using the van der Pauw technique, the sheet resistance R_s can easily be found in a uniform sample. The technique applies to any particular shape as long as there are no non-conducting sections or holes and is a thin-plate with four contacts equally spread out on the perimeter of the sample. The diameter of the contacts, d, must be significantly small compared to the distance between the contacts, D. The error produced by the size of the contact is on the order of d/D. A schematic of the van der Pauw configuration is shown in Figure 3.4.

Using the configurations in Figure 3.4, the characteristic resistances R_a and R_b can be calculated using the relations shown in Equations 3.5 and 3.6. The current is applied into contact one and out of contact two while the voltage V_{43} is measured to solve for R_a. The current is

applied into two and out of contact three while the voltage V_{14} is measured to solve for R_b. The

characteristic resistances are used to solve numerically for the sheet resistance, R_s, through the

van der Pauw equation, Equation 3.7.
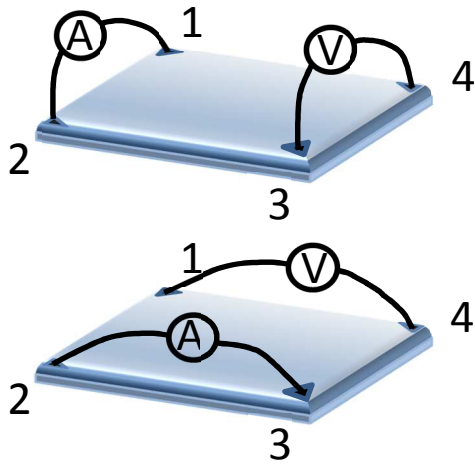
$$R_a = V_{43} / I_{23} \qquad \text{(Equation 3.5)}$$

$$R_b = V_{14} / I_{23} \qquad \text{(Equation 3.6)}$$

Figure 3:4: van der Pauw Configuration

$$e^{\wedge}(-\pi * R_a / R_s) + e^{\wedge}(-\pi * R_b / R_s) = 1 \qquad \text{(Equation 3.7)}$$

The Hall voltage along with the sheet resistance can be used to calculate the Hall

mobility, μ, by the relation shown in Equation 3.8.

$$\mu = |V| / (R_s * I * B) \qquad \text{(Equation 3.8)}$$

In summary, the Hall measurement provides electrical characterizations that give specific

parameters that define semiconductor material. The primary parameters acquired are sheet

resistivity, sheet density, Hall mobility, and material type.

The resistivity and Hall measurement results must be verified for internal consistency to

ensure ohmic contact and sample uniformity. For the Hall measurement system located in the

Bio-photonics lab at the Engineering Research Center, the operational procedure provides for

16

verification of results. Recommendations for sample sizes between 1 cm^2 and 2.5 cm^2 ensure optimal measurement geometries.

The magnet controller is switched on along with the water cooling system to allow twenty minutes for stabilization before measurements are completed. Contact preparation is the single most important step in all of the Hall measurement procedures. For this system, the sample is required to be cleaned in a three minute acetone bath followed immediately by a three minute methanol bath. Once the sample is dry, indium contacts are applied to each of the four corners of the sample using a soldering iron, preferably in a triangular shape as shown in Figure 3.5.
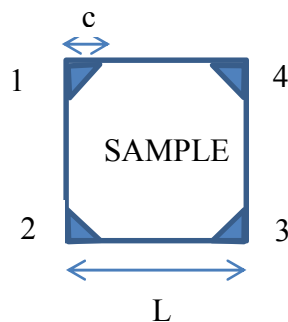
Figure 3:5: Contact Preparation

The technique for applying the indium to the sample is crucial. While applying the indium to the sample, a circular motion with the soldering tip insures temperature uniformity and assists in degassing of the liquid indium. The contact should be as small as possible as the measurement error is increased by a factor of c/L. It is critical that the indium does not go beyond the sample edge as shorting to the substrate can occur and will give erroneous errors in the measurement results. Additionally, the solder tip should not come in contact with the sample directly as damage could occur to the sample.

The properly prepared sample can be checked for internal consistency by verifying ohmic

contact quality and sample uniformity. An ohmmeter is used to measure the diagonal contacts,

R_{13} and R_{24}. The results must be $R_{13} = R_{24}$ within 5%. If the results are outside this limit, no

further measurements should be done until the sample problem is resolved. Once an acceptable

resistance measurement is acquired, the maximum allowable test current, I, can be determined by

the relation in Equation 3.9.

$$I < (200R)^{-0.5} \hspace{3cm} \text{(Equation 3.9)}$$

This limit is to ensure heating does not occur due to higher currents. For the previously

mentioned system, the maximum current produced is 2 mA and, therefore, any samples lower

than 1300 Ω will not exceed the maximum allowable current.

The sample is ready for placement in the Hall measurement system. The first step in the

measurement is a routine that adds a layer to the verification of internal consistency. The

connectivity test runs as many iterations as determined by the user. The minimum recommended

number of iterations is five. The High/Low resistivity selection is set to Low for all samples with

resistance lower than 1 MΩ. The test current range selected is preferred to be as close to the

maximum allowable current for the sample. Once the connectivity test completes, four graphs

indicate the linearity of the measurement at each of the four contacts. If all four graphs display a

linear curve, then the measurement should continue to the resistivity measurement.

The resistivity routine requires the same setup as was selected for the connectivity routine

with the addition of a field to enter the film thickness. Once this completes with linear graphs,

the final routine, Hall measurement, is selected. For this routine, a few additional steps are

required. The meter for the measurement of the magnetic field is zeroed. The magnet controller

is switched to a field using a positive current and is set to twenty amperes. The field is measured

18

and entered into the system in units of kGauss. The routine steps through the number of user selected iterations for the field with positive current and then pauses, allowing the user to switch the controller to a negative field. This routine completes with linear graphs for result verification.

3.3. X-ray Diffraction Characterization

The characterization of materials using X-ray diffraction is made possible by Bragg's Law. This law applies to a periodic array such that occurs in a crystal lattice. This law defines the angles that are produced from scattering of electromagnetic waves that are incident on the crystal lattice. The parallel planes of the periodic array with spacing d_{hkl} will produce constructive interference from the incident beam when the angle θ satisfies Bragg's law shown in Equation 3.6. This geometry is shown in Figure 3.6.

For a fixed wavelength λ, a family of planes will produce a diffraction peak at a specific angle θ as determined by the spacing d_{hkl}. Moreover, the diffraction vector Diff, the vector that bisects the angle between the incident and diffracted beam, and the plane normal [hkl], the direction perpendicular to the plane of atoms, must be parallel. Bragg's law is shown mathematically in Equation 3.10.

$$2dsin\theta = m\lambda \qquad \text{(Equation 3.10)}$$

From Figure 3.6, the lower wave travels 2dsinθ farther than the upper wave. When this distance equals an integer multiple, m, of the wavelength, λ, Bragg's law is satisfied.

X-ray diffraction scans normally measure the scattered X-ray intensity as a function of the two-theta angle, omega, or both. A scan that measures X-ray intensity as a function of the two-theta angle without changing omega is called a detector scan. In this configuration, the detector moves varying the two-theta angle only. A scan that measures the X-ray intensity as a function of ω is called a rocking curve. In this configuration, the two-theta angle is kept constant

19

while ω is varied, or "rocking" the sample. This type of scan is used primarily to study defects within the crystal lattice. These defects include dislocation density, mosaic spread, curvature, mis-orientation, and inhomogeneity.
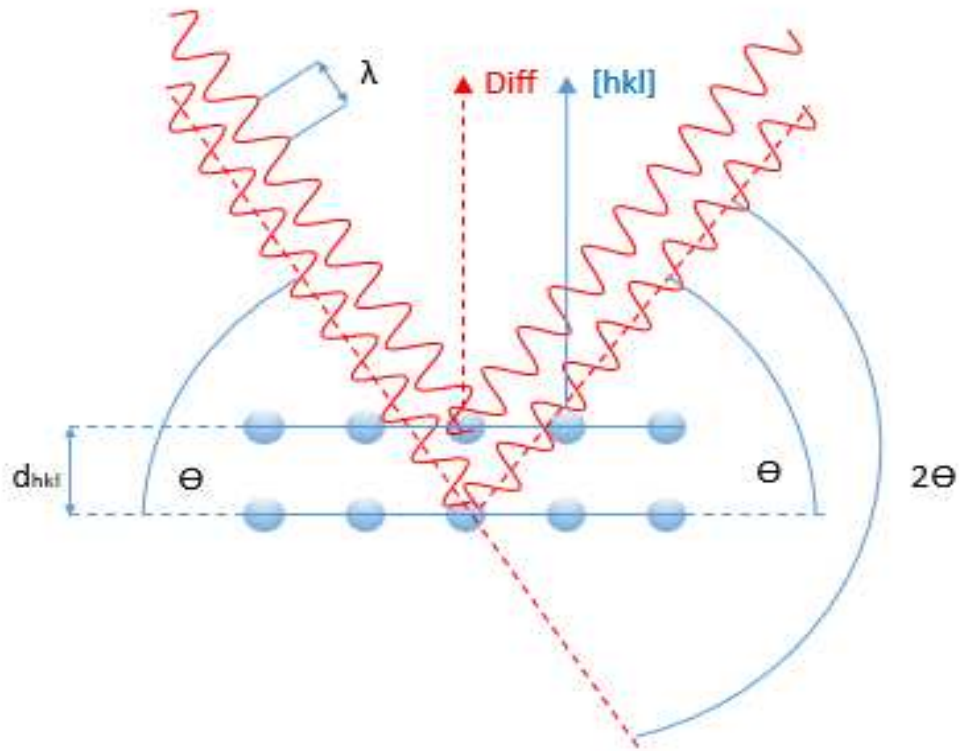
Figure 3:6: Bragg's Law

A scan that measures the X-ray intensity as a function of both two-theta and omega is called a coupled scan. For this scan, the X-ray Tube and detector move in such a way keeping the two-theta angle twice omega. The coupled scan is used to measure the Bragg diffraction angle. Furthermore, the coupled scan is used to determine lattice mismatch, relaxation, ternary composition, thickness, and super-lattice period. The geometry of each of these scans is demonstrated from the configuration shown in Figure 3.7.
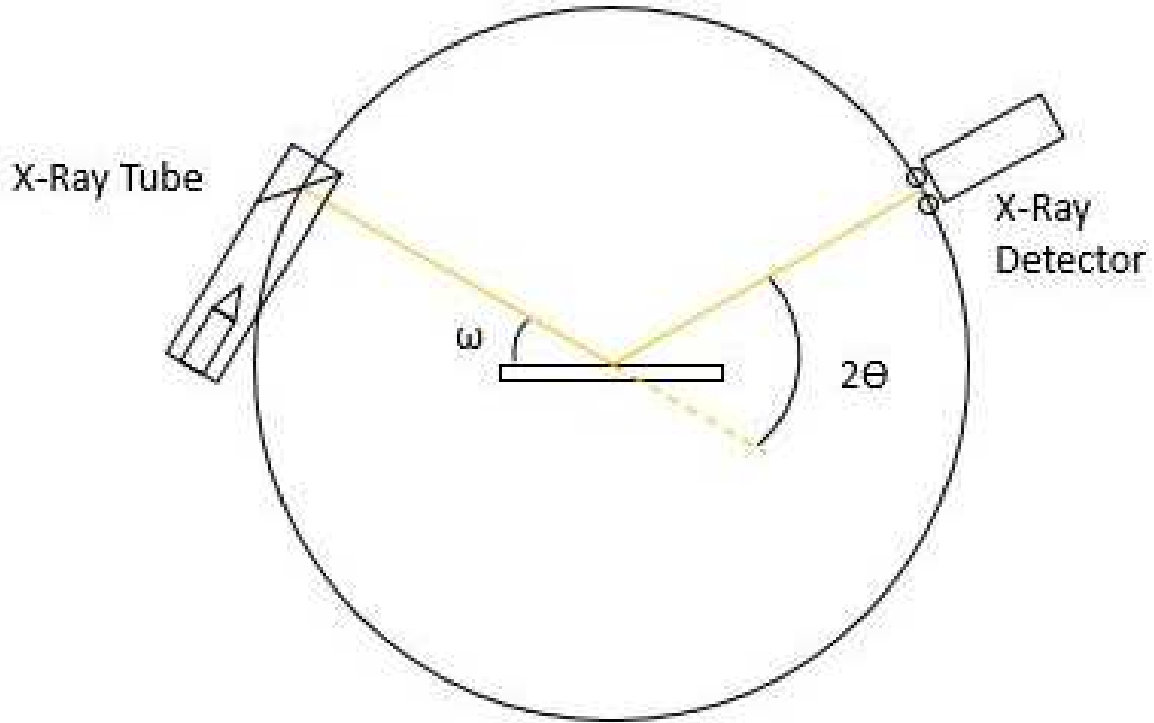
Figure 3:7: X-ray Diffraction Configuration

The coupled scan can provide the d_{hkl} spacing for the Bragg peak. This will identify changes in the lattice spacing in one direction only but will be an indicator of composition and strain-relaxation changes. For materials of high crystal quality, the coupled scan will reveal interference fringes. Interference fringes are observed in the scattering pattern because of the different optical paths caused by the interface at the layer. From the interference fringes, the thickness can be estimated based on Equation 3.11.

$$t = (n_1 - n_2)\lambda / 2(\sin \omega_1 - \sin \omega_2) \qquad \text{(Equation 3.11)}$$

Interference fringes are shown in the coupled scan in Figure 3.8.

21

3.4. Electrochemical Capacitance-Voltage Profiling
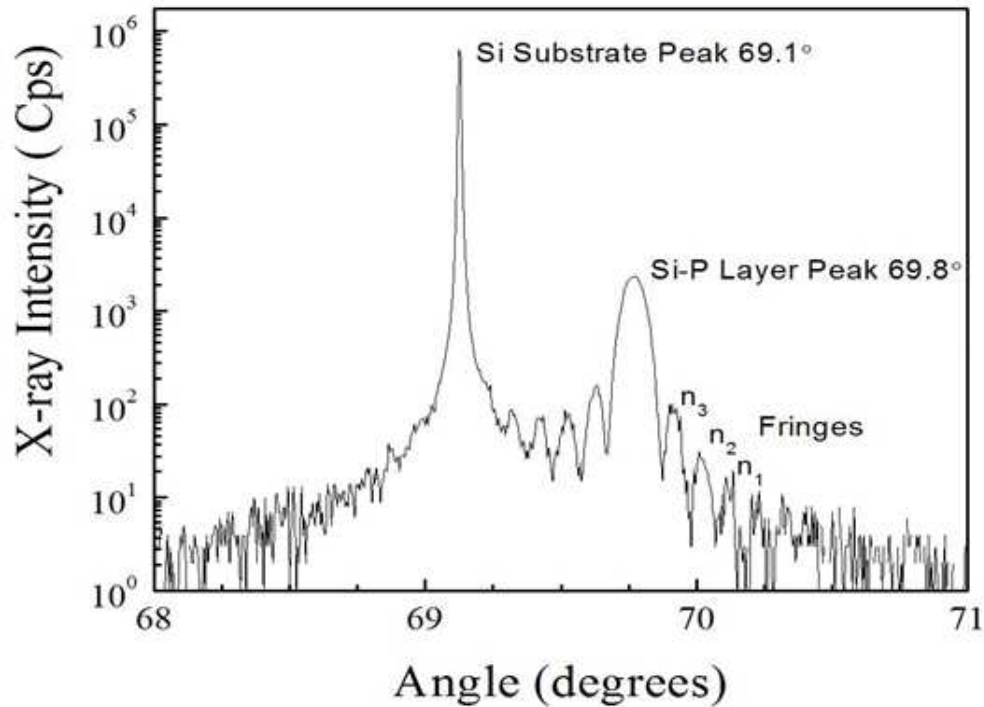
Figure 3:8: Interference Fringes

Electrochemical Capacitance-Voltage (EC-V) profiling is a method primarily used to identify carrier concentrations with depth in a semiconductor material. This particular technique employs a method of creating a depletion region that enables capacitance measurements. The depletion region can be created using a Schottky contact. This contact is created by a metal-semiconductor interface that produces a barrier potential. This barrier potential creates a separation of charges much like that of a capacitor composed of two parallel plates. The capacitance measurements of this Schottky contact allow the EC-V method to extract dopant profile information.

The depth profiling occurs through a process where the semiconductor is electrolytically etched followed by a capacitance measurement. The sample being measured is placed in an electrochemical cell that contains an electrolyte and a sealing ring makes contact with the

semiconductor. The area within the sealing ring is the contact area. A schematic description is shown in Figure 3.9. The depletion region is created within the contact area when a potential is applied to the semiconductor and the platinum electrode with a reference to the saturated calomel electrode.

The carriers are attracted or repelled in the depletion region based on the charge of the ions in the solution next to the interface, and the polarity of the bias applied to the semiconductor. The depleted region then, is created on p-type semiconductors by positive ions in the solution that repel the holes, the majority carriers for p-type semiconductors. The depleted region is created on the n-type semiconductors by negative ions in the solution that repel the electrons. Therefore, for n-type semiconductors, the semiconductor must be biased positive thereby attracting the negative ions. Moreover, for p-type semiconductors, the semiconductor must be biased negative and thereby attracting the positive ions. These configurations enable the measurement of the capacitance and the depletion width.

The width and the capacitance of the depletion region are determined by the relations shown in Equation 3.12 and 3.13.

$$W_d = [2(\Phi - V)\,\varepsilon_o\,\varepsilon_s\,\sigma / (q\,N)]^{1/2} \qquad\qquad \text{(Equation 3.12)}$$

$$C = A / 2\,[q\,N\,\varepsilon_o\,\varepsilon_s\,\sigma / (\Phi - V)]^{1/2} \qquad\qquad \text{(Equation 3.13)}$$

For these equations, W_d is the depletion width, Φ is the contact potential or built-in voltage, V is the applied voltage, ϵ_o is the permittivity of free space, ϵ_s is relative permittivity of the semiconductor, q is the electron charge, N is the carrier concentration, C is capacitance, and A is the area of the depletion region. It can be shown that there is a linear relationship between the applied voltage V and $1 / C^2$. This relationship enables the carrier concentration N to be determined using the relation in Equation 3.14.

$$1 / C^2 = 2(\Phi - V) / (q\, N\, \varepsilon_o\, \varepsilon_s\, \sigma\, A^2) \qquad \text{(Equation 3.14)}$$

From this relation, the carrier density at the depletion layer edge is given by Equation 3.15.

$$N = 1 / (q\, \varepsilon_o\, \varepsilon_s\, \sigma\, A^2) \times C^3 / (dC/dV) \qquad \text{(Equation 3.15)}$$
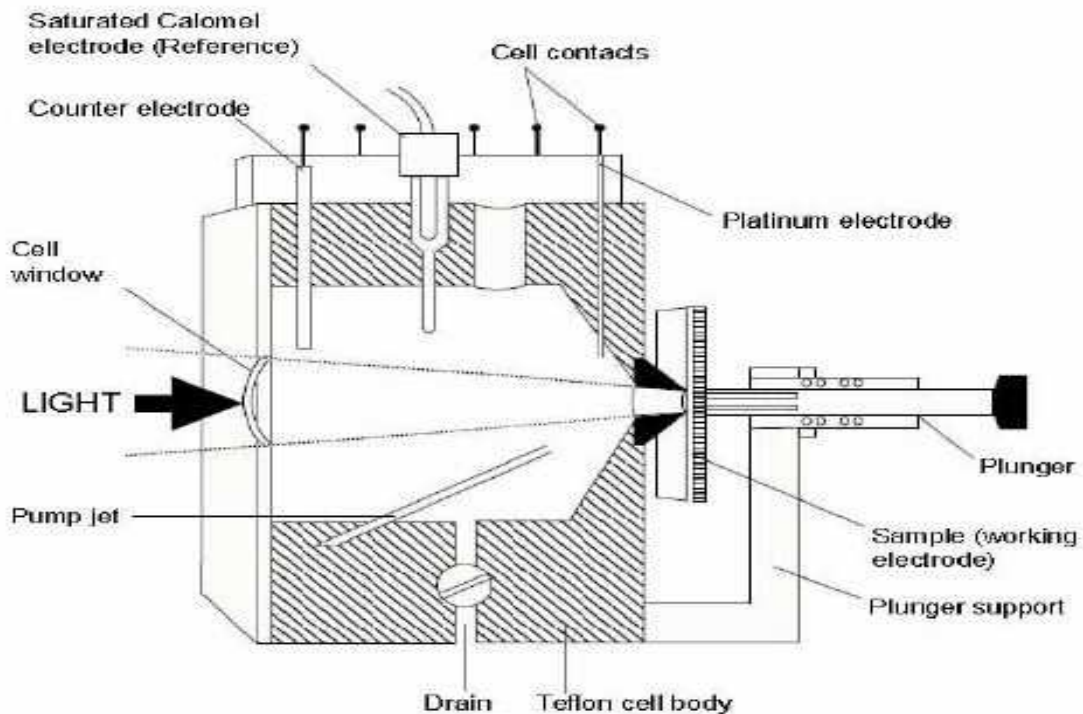
Figure 3:9: Electrochemical C-V Measurement System [12]

Equation 3.15 only requires the measurement of the area A, the capacitance C, and the change in capacitance with respect to the voltage, dC/dV to determine the charge carriers, N. Once the charge carriers are determined, the depth profile can be evaluated.

The depth profiling occurs through the process of dissolving the semiconductor electrolytically. As the semiconductor is dissolved, a further separation of charge occurs. The dissolving process is dependent on the presence of holes and, therefore, p-type semiconductors require only the forward biasing of the electrolyte-semiconductor junction. The process of

24

dissolving the n-type semiconductor requires the sample to be illuminated with a particular wavelength of light that will stimulate the electrons in the valence band to the conduction band and create the needed holes. The reverse biasing then attracts the holes to the surface. The specific requirement for the wavelength of light, λ, is given in Equation 3.16.

$$\lambda \leq h_c / E_g \qquad \text{(Equation 3.16)}$$

The final parameter to be considered is the etch depth, W_r. For most semiconductors, this parameter is determined by Faraday's law of electrolysis. This law is used to derive the etch depth as shown in Equation 3.17.

$$W_r = M / (z \, F \, \rho \, A) \int I \, dt \qquad \text{(Equation 3.17)}$$

In Equation 3.17, M is the molecular weight of the semiconductor, z is the valency number of ions, F is the Faraday constant, ρ is the semiconductor density, A is the area of the contact, and $\int I \, dt$ is the total charge with I being the dissolution current. From the relation above, it may be obvious what impact the measurement of the area may have on the result, but for clarity, the contact area measurement is extremely impactful to the accuracy of the carrier concentration and etch depth results. As previously mentioned, this process is applicable to most semiconductors, but for silicon, Faraday's law of electrolysis does not hold true in the general sense. To overcome this, a modified technique must be used.

The etching of silicon is required to be done using a process known as pulse anodization. An electrolyte solution in contact with the silicon has a current driven through it to oxidize a small layer of the silicon. The oxide is then removed in a subsequent etching step to remove the silicon material. For the highly-phosphorus doped silicon samples, further adjustments to the technique may be required.

25

3.5. Raman Spectroscopy Characterization

Raman spectroscopy characterization is a technique used to investigate the properties of semiconductor materials. For semiconductor materials, the layer thickness can be estimated up to several hundred nanometers, the crystallinity and composition of the material can be estimated, and whether the material is under compressive or tensile strain. These properties can be determined because of a particular type of scattering that occurs.

Light incident on a semiconductor surface is reflected, transmitted, absorbed or scattered. Two types of scattering are Rayleigh scattering and Raman scattering. Rayleigh scattering is the elastic scattering of visible light or other forms of electromagnetic radiation that occurs when the total kinetic energy is conserved, and, therefore, no energy is lost to the process. Raman scattering is inelastic scattering as the total kinetic energy is not conserved, and energy is lost to the process as vibrations in the form of either heat or sound. The resultant wavelength of the scattered light is therefore shifted up or down.

A monochromatic light source of a known wavelength incident on a semiconductor will produce Raman scattering. The Raman scattering can then be characterized based on the light source wavelength and the vibrational states of the semiconductor. The vibrational states are dependent on temperature and the chemical bonds of the semiconductor. They can be understood as diatomic vibrations, but the complete analogy must include the interaction of a large collection of atoms to properly characterize the vibrational states. From these vibrational states, Raman bands have been produced that indicate specific chemical bonds and vibrational energies. From these bands, a determination of the previously mentioned properties can be determined. [13]

The Raman spectroscopy used for this work consisted of five main components. The first main component was the excitation source. For this system, two different wavelength lasers were available for sample excitation, green at 532 nm and red at 633 nm. The second main components consisted of the sample illumination and light collection optics. The third component was the wavelength selector which consists of a filter or a spectrophotometer. The fourth was the detector which could be a photodiode, charged coupled device (CCD), or a photomultiplier tube (PMT). The fifth main component was the computer for display and analysis of the Raman data. A schematic diagram is shown in Figure 3.10.

The spectrometer used in this setup was a Horbia model iHR 550. The specifications for this spectrometer are shown in Table 2.

Table 2: Horbia iHR 550 Spectrometer Specifications

Focal Length:	550 mm	Spectral Range:	150 to 1500 nm
Aperture:	f/6.4	Flat Field Size:	30 mm x 12 mm
Grating Size:	76 mm^2	Resolution:	0.025 nm
Magnification:	1.1	Repeatability:	+/- 0.075 nm
Spectral Dispersion:	1.34 nm/mm	Stray Light:	1x10^{-5}
Scan Speed:	160 nm/second	Step Size:	0.002 nm

The grating selection was selected based on the desired resolution. A selection of 1800 provides high resolution and a narrow shift range. A selection of 600 provides a lower resolution and a wide shift range. The center wavelength is calculated using the relation shown in Equation 3.18.

$$\lambda_{cent} = \frac{1}{1/\lambda_{laser} - \Delta \upsilon_{(Raman\,shift)} \times 10^7}$$
(Equation 3.18)

This relation takes into account the wavelength of the laser used. For this work, the 532 nm green laser was used. For crystallized silicon, the center wavelength using this laser is 547

27

nm. Once this wavelength was determined, it was entered into the spectrometer program. The room lights were turned off at this point to eliminate any artifacts from this light, and the *Run* button was selected. The display was adjusted to match the correct center wavelength due to inherent inaccuracies in the setup and then the focus was adjusted to obtain the maximum intensity of the Raman shift peak.

The peak intensity of the Raman shift peak was in some cases low. This situation required the voltage on the laser controller to be increased while observing the power meter. This was accomplished by several ancillary steps. The power meter detector was installed in the light path, and the meter's power was turned on. The light was then blocked in front of the detector while the meter was zeroed. The block was then removed, and the voltage was adjusted slowly ensuring that five volts was not exceeded. For silicon samples, the power was adjusted to
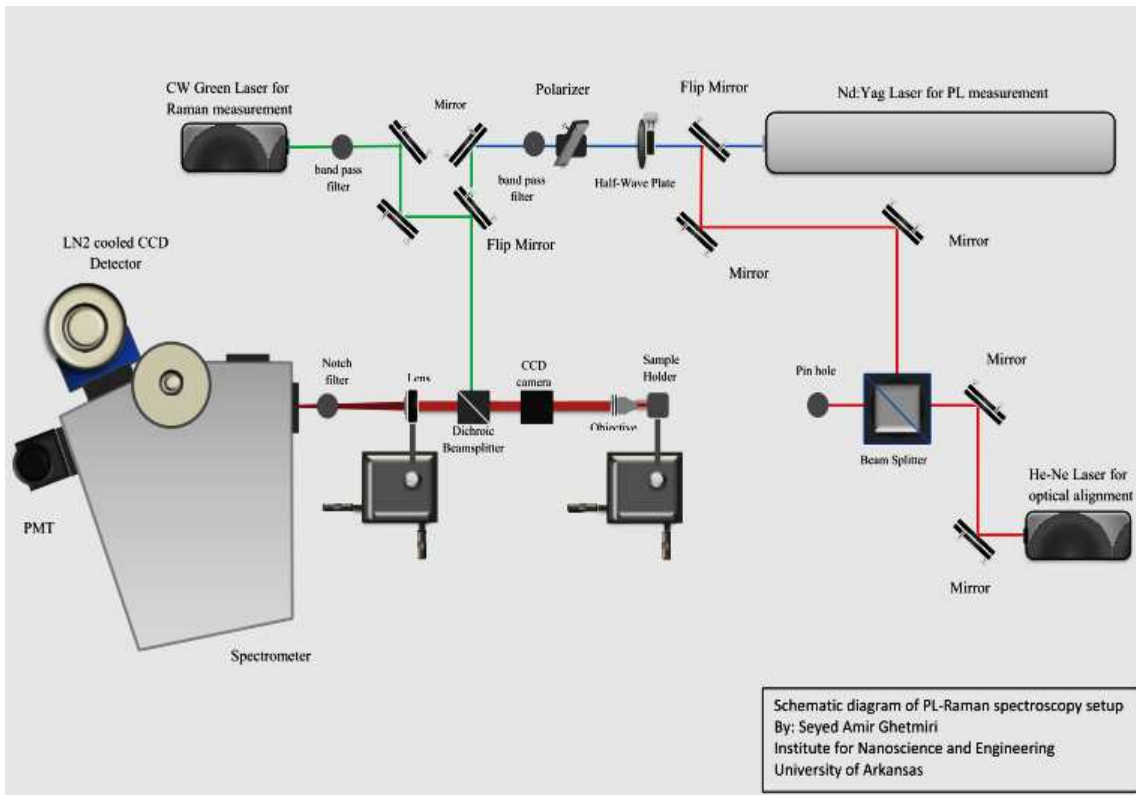
Figure 3:10: Schematic Diagram of Raman Spectroscope [14]

approximately 0.03 Watts. Once this was set, the detector was removed from the light path and the focus was once again adjusted.

3.6. Photoluminescence Characterization

Photoluminescence (PL) characterization is an optical characterization tool for understanding the electronic structure of materials. Some of the properties that can be examined are impurity and defect levels, inherent recombination mechanisms, and material bandgap. This tool was an obvious choice of methods to study the Si:P samples used for this work and to complete a direct comparison of these samples with a standard silicon crystalline sample.

Photoluminescence occurs when an excitation source such as a laser provides photon excitation for hole carrier injection that may lead to radiative recombination. The emission spectrum can indicate the electronic bandgap of the material. The sensitivity of PL characterization can indicate levels of impurities that can impact material quality. The quality of the PL signal is directly related to recombination rates and can be determined by the PL peak intensity and broadening of the PL signal. For this work, the plan was to compare the PL of a standard crystalline silicon sample to the Si:P samples. The PL used was a setup created in the lab. The laser was set to operate at a wavelength of 532 nm with a spot size of 100 μm diameter with the chopper operating at a frequency of 377 Hz. The configuration of the PL system is shown in Figure 3.11.

3.7. Spectroscopic Ellipsometry Characterization

Ellipsometry utilizes polarized light to determine material characteristics such as lattice constant, film strain, crystallinity, film thickness, and composition. Material microstructure, surfaces, and thin films can be evaluated with ellipsometry with accuracy relative to the wavelength and the sensitivity inherent in the measurement of the relative phase change of the
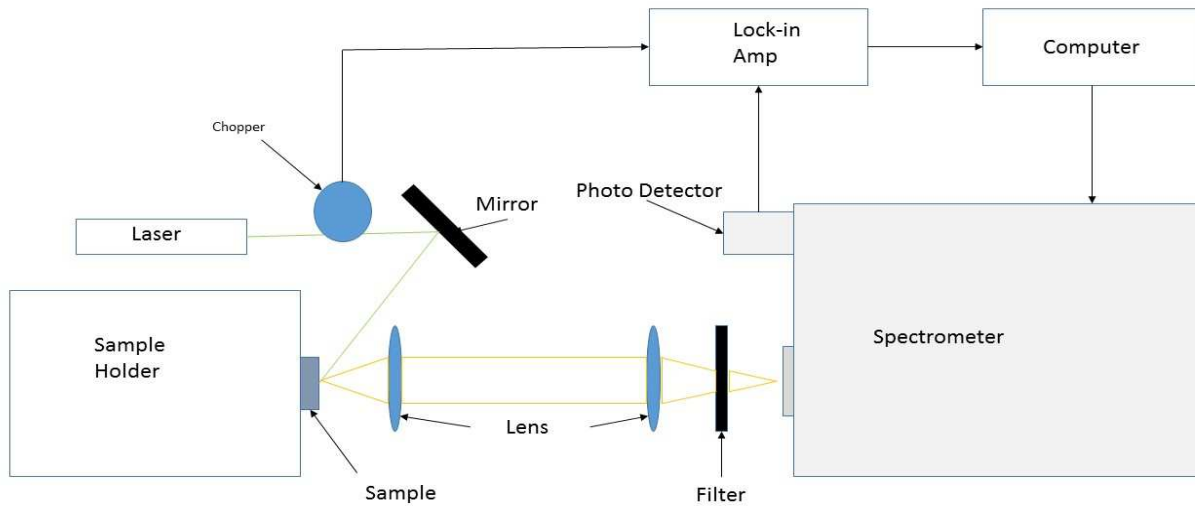
Figure 3:11: PL Configuration

reflected light that is polarized. Furthermore, ellipsometry does not require the absolute intensity of the reflected light to be measured thereby eliminating the need for special reference samples that are typically required for intensity reflectance measurements.

Ellipsometry has been used for the determination of numerous material properties such as alloy ratio, crystallinity, optical anisotropy and various process variables such as growth and etch rates. The more common use has been for the measurement of optical constants and thin film thicknesses. These common uses were the primary focus in this work for use in characterizing highly-phosphorus doped silicon samples.

The ellipsometry system used for this work was the VASE Ellipsometer made by the J.A. Woollam Company [15]. VASE stands for variable angle spectroscopic ellipsometry, and the variable angle is the versatile strength of this system. Other systems employ a fixed angle as well as a fixed wavelength that limits the amount of information acquired in one scan. This may have some benefit in cases where a single wavelength of light is the primary area of concern. For

broader evaluations to determine such things as thin film thicknesses and the complex refractive index and the dielectric function tensor, a broad band light source is employed for a greater wavelength range. This leads to a spectral range of samples determined with greater accuracy.

This tool is capable of measuring the psi (Ψ) and delta (Δ) parameters in the spectral range of 300 to 2500 nm. This range was expected to be sufficient for the samples in this work as they are assumed to be similar to bulk silicon as silicon is the primary element of the material. The wavelength of interest for silicon is typically in the range of 1100 nm.

This introduction of ellipsometry makes a number of assumptions about the reader's knowledge of electromagnetic radiation and specifically, polarized light. Polarized light is at the core of what enables ellipsometry and, therefore, a more rigorous understanding of polarized light will bring a more detailed understanding of the results of ellipsometry measurements. The first step of this rigorous understanding is to review the electromagnetic plane wave that is defined by Maxwell's equations for electromagnetic fields.

Maxwell's equations that apply to a non-conducting and non-dispersive medium must apply to any propagating light beam. The equations are shown in the following form in Equations 3.19 through 3.22.

$$\underline{\nabla} \bullet \underline{E} = 0 \qquad \text{(Equation 3.19)}$$

$$\underline{\nabla} \bullet \underline{B} = 0 \qquad \text{(Equation 3.20)}$$

$$\underline{\nabla} \times \underline{E} + \frac{1}{c} \frac{\partial \underline{B}}{\partial t} = 0 \qquad \text{(Equation 3.21)}$$

$$\underline{\nabla} \times \underline{B} - \frac{\mu\epsilon}{c} \frac{\partial \underline{E}}{\partial t} = 0 \qquad \text{(Equation 3.22)}$$

For these equations, $\underline{E}$ is the electric field, $\underline{B}$ is the magnetic field, c is the speed of light, μ is the permeability, and ϵ is the dielectric function.

31

Equations 3.19 through 3.22 are the basis of the wave equation that is shown in Equation 3.23.

$$\underline{V^2 E} - \frac{1}{v^2} \frac{\partial^2 \underline{E}}{\partial t^2} = 0 \qquad \text{(Equation 3.23)}$$

Equation 3.23 is the wave equation with the optical impedance v defined in equation 3.24.

$$v = \frac{c}{\sqrt{\epsilon \mu}} \qquad \text{(Equation 3.24)}$$

The electric field wave equation has a specific solution that is defined as the electromagnetic plane wave. This plane wave can then be shown mathematically in Equation 3.25.

$$\underline{E}(\underline{r},\underline{t}) = \underline{E}_o \, e^{-i\frac{2\pi \tilde{n}}{\lambda} \check{z} \bullet \hat{r}} \, e^{i\omega t} \qquad \text{(Equation 3.25)}$$

The electromagnetic plane wave consists of the variables $\check{z}$ for the unit vector along the wave propagation direction, λ is the wavelength of light, $\tilde{n}$ is the complex index of refraction, *n-ik*, ω is the angular frequency of the wave, and $\underline{E}_o$ is the constant specifying the amplitude and polarization state of the wave. The electric field, the magnetic field, and the direction of propagation are perpendicular to one another. Because of this relationship, typically the electric field and the direction of propagation are used to define the plane wave.

The defined plane wave can have many states as it propagates through space. The state is defined as the polarization state. The determining factor as to how the direction of the electromagnetic plane wave propagates is the complex index of refraction. A graphical representation of the electromagnetic plane wave is shown in Figure 3.12.

The complex index of refraction in the electromagnetic plane wave expression can cause the amplitude of the wave to decrease exponentially if the imaginary part (extinction coefficient) is non-zero. This effect is shown more clearly in the expression of Equation 3.26.

$$E \propto e^{\frac{-2\pi k z}{\lambda}}$$ (Equation 3.26)

For the relation in Equation 3.21, k is the extinction coefficient, λ is the wavelength, and z is the distance of propagation. This relation shows as the plane wave propagates in the z direction, the amplitude E will reduce. When the reduction of the amplitude becomes 1/e of the initial amplitude at a propagation length of L_p, this becomes known as the penetration length and is given by the relation in Equation 3.27.

$$L_p = \frac{\lambda}{2\pi k}$$ (Equation 3.27)

In the relation in Equation 3.27, it is noteworthy to emphasize the impact the extinction coefficient, k, has on the depth of penetration of the plane wave. For materials that have a large extinction coefficient, the plane wave may likely not penetrate the layer and would give an invalid result in the measurement. This is particularly important when measuring metal films greater than 50 nm in thicknesses as the maximum is 100 nm. [17]

3.8. Device Simulation

Solar cell simulation is primarily associated with crystalline silicon solar cells as this is the majority of solar cells that are currently fabricated. These cells are basic p-n junctions yet their modeling cannot easily be accomplished due to the optical coupling. This complexity does not allow for description by analytical methods and, therefore, has to be dealt with by a more rigorous physically-based process.
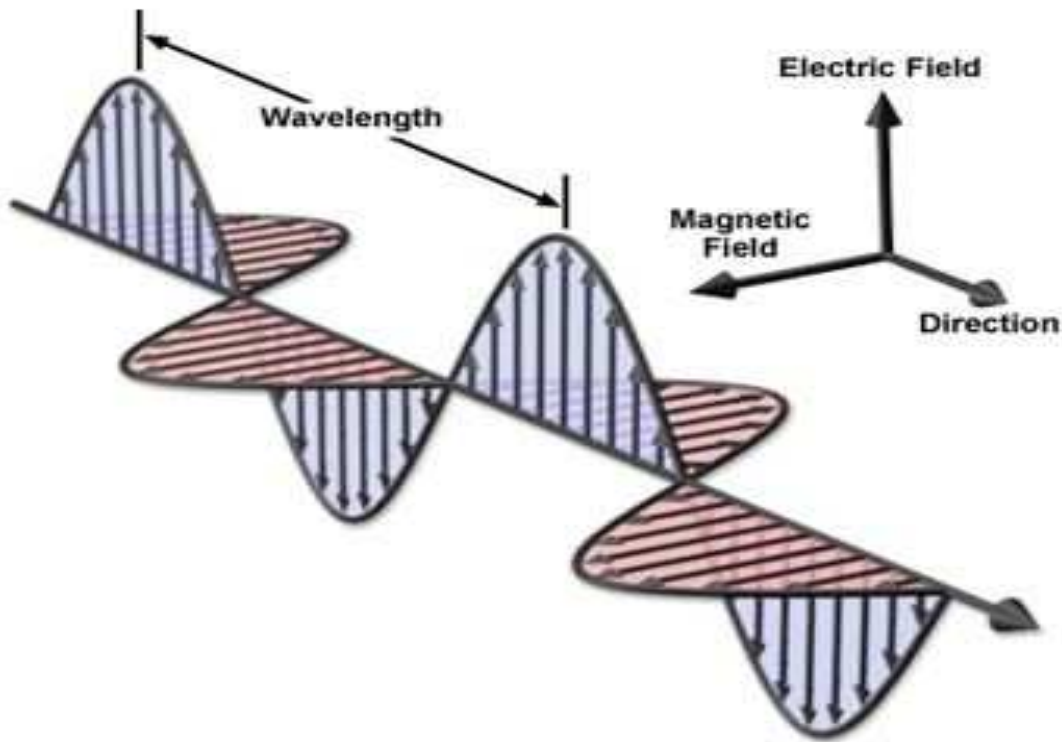
Figure 3:12: Electromagnetic Plane Wave [16]

Solar cell simulation can be divided into two specific areas for simulation, fabrication process simulation and device simulation. Fabrication process simulation can include many features and capabilities. Some basic capabilities include deposition, diffusion, implantation, oxidation, etching, and epitaxial growth. Silvaco [18] provides a process simulator called ATHENA with these basic capabilities and more. This physically-based process simulator can be used to predict what type of structures will be created based on sequences of semiconductor processes.

Device simulation of solar cells was first accomplished using analytical formulas that mimic empirical data with accuracy and simplicity. Empirical methods such as this could provide close approximations but were not able to provide predictive behavior or any real insight into the

34

device being simulated. A more robust and predictive method of device simulation requires a physically-based device simulator.

A simulator based on a more robust and predictive method can effectively produce the electrical characteristics of devices based on the physical structures and the relevant bias conditions. Silvaco provides a device simulator that is based on physical models. This simulator is Atlas. Atlas can provide modeling of many physically-based electrical parameters such as DC, AC small-signal, and time-dependency. Additionally, optoelectronic interactions with general ray tracing can be accomplished. Many more features and capabilities are possible with one primary caveat. Such physically-based models require that all physics involved in the simulation must be accounted for and included in the simulator. Furthermore, numerical techniques are required to solve the equations that describe the physical model.

The first solar cell example used both fabrication process simulation and device simulation to give a basic understanding of the simulation software. A mesh was defined within ATHENA that gives the needed numerical resolution to provide for correct simulation at all boundaries. The code defined a process for p-type boron doping of the (100) oriented substrate to 1014 cm-3. A layer of oxide is grown to 50 nm followed by an implantation of phosphorus using a dose of 1x1015 cm-2 at an energy of 30keV. This implantation is followed by a drive-in step at 900°C for 10 minutes. These steps form the p-n junction of the solar cell and are followed by contact formation. Once the contacts are formed, the electrodes are created to enable characterizations.

Characterization begins with the starting of Atlas to get the short-circuit current and the open circuit voltage. The first step is to set the material constants for both the contacts and the

substrate. This is followed by the setting of the light beam to the solar spectrum. This setting

allows for the proper short-circuit current and the open-circuit voltage to be calculated.

Following this characterization, Atlas is set to run spectral response of the device.

Following the initial settings, the light beam is set for a monochromatic light for the spectral

analysis. The spectral analysis produces the internal and external quantum efficiencies

(IQE/EQE) and plots the available photocurrent. This photocurrent accounts for absorption in the

semiconductor regions only. To determine the overall absorption, the EQE must be solved for as

shown in Equation 3.28.

$$\text{EQE} = \frac{Ianode}{Isourcecurrent} * absorption \qquad \text{(Equation 3.28)}$$

Following the spectral analysis, the I-V characterizations are completed. Again, this

began with starting Atlas and running the same initial device settings. This allowed for the

calculation of I-V characteristic. The code was set to also calculate the short-circuit current

density, maximum power, and the fill factor associated with this device. Errors occurred at this

point of the code that was later attributed to conflicts with the Windows operating system. This

code can be run in a UNIX environment without error or change to the code. This is a common

occurrence with the ATHENA and Atlas programs of Silvaco, Inc.

The second solar cell simulation did not include device fabrication requiring process

functions and therefore did not require the use of ATHENA as was the case for the first solar cell

example. This example utilized the function of 'auto meshing' to create the device with the

proper numerical resolution for correct simulation at the boundaries. The substrate was n type

and doped to a uniform concentration of 1x1014 cm-3. The device was crystalline silicon

bounded top and bottom by Tin-doped Indium Oxide (ITO) electrodes.

The device was defined as a a-N diode. The material parameters were modified from the default parameters to describe a crystalline material. The changes made included the following parameters: Mun= 20cm2/V•s, Mup= 1.5cm2/V•s , Nc300=2.5x1020 cm-3, Nv300=2.5x1020 cm-3, Eg300=1.9eV. The complex index of refraction for the ITO electrodes was given by the data from the Sopra database. Additionally, the recombination models implemented were Shockley-Read-Hall and Auger recombination. The optical source was specified from above with normal incidence using a transfer matrix model for optical characteristics. The beam was set to AM1.5. With these parameters set, the characterizations were able to be completed.

The first build and characterization was considered a solar cell without defects. Following the first build, identical script was run with the addition of code that introduced defects into the solar cell. The defects were defined by many different parameters. These parameters describe the density of states (DOS) for these defects. The total DOS is modeled in Atlas with four DOS bands. There are two tail bands that consist of a donor-like valence band and an acceptor-like conduction band and are modeled with an exponential tail distribution. Two deep level bands consist of one acceptor-like band and one donor-like band and are modeled with a Gaussian distribution.

The first defined parameters describe an exponential tail distribution by the valence and conduction band edge intercept densities. The parameters were defined as NTA=1x1021cm-3/eV and NTD=1x1021cm-3/eV. The characteristic decay energy is defined by the parameters WTA and WTD. For this example, these parameters were set to WTA=0.033eV and WTD=0.049eV. For a Gaussian distribution of the DOS, the parameters NGA and NGD define the total density of states, WGA and WGD define the characteristic decay energy, and EGA and EGD define the peak energy distribution.

37

These parameters were set to NGA=1.5x1015 cm-3, NGD=1.5x1015cm-3, WGA=0.15eV, and WGD=0.15eV. The remaining parameters, SIGTAE through SIGGDH, are related to the electron and hole cross-section and the equivalent donor states. The parameters impact the probability of occupation of a trap level at energy E in the steady-state case. These parameters were set to SIGTAE=1x10-17 cm2, SIGTAH = 1x10-15 cm2, SIGTDE=1x10-15 cm2, SIGTDH=1x10-17 cm2, SIGGAE=2x10-16 cm2, SIGGAH=2x10-15 cm2, SIGGDE=2x10-15 cm2, and SIGGDH=2x10-16 cm2.

3.9. Device Fabrication

The basis of the silicon solar cell is the p-n junction. The p-n junction provides the needed mechanism for the separation of charges for a solar cell to develop an electrical potential that can provide a flow of electricity. Before this flow of electricity can occur, electrical contacts must be devised in some fashion that does not significantly reduce the developed potential while at the same time provides a good connection to an external circuit. Here in lies one of the greatest challenges to improving solar cell efficiency.

The plan for this work was to take a sample and construct a solar cell by fabricating contacts onto the sample. For a basic crystalline silicon solar cell, a top grid is designed such that the minimum amount of metal is used to collect the charges and provide a path for current flow while minimizing the area coverage to reduce the shadowing effect. Generally, the backside is not subject to light penetration and therefore shading is not a problem for this particular design. For this reason, the back contact may cover the entire back surface.

Initially, a simple top grid and back contact for the p-n junction was constructed using an application of indium for good contact adhesion. This plan required little resources and was easy

to fabricate. The characterization results were determined as outlined in the following section, Device Characterization.

3.10.   Device Characterization

Solar cell characterization consists of a wide range of measurements depending on the particular physical properties of interest. Mechanical, electrical, and optical properties can impact the operation of the solar cell and, therefore, numerous measurements are used to evaluate these properties. For the purpose of the work of characterizing highly-phosphorus doped silicon samples, the electrical and optical properties were of greatest interest. Solar cell efficiency is the core characterization tool for solar cells and is highly dependent on the electrical and optical characteristics.

Solar cell efficiency is the ratio of the electrical energy output to the energy input from the sun. The efficiency, η, is determined by the following relation shown in Equation 3.29.

$$\eta = \frac{PowerOutmax}{Solar\ Energy * Area} \qquad \text{(Equation 3.29)}$$

In Equation 3.29, $PowerOutmax$ is the power output of the solar cell at the maximum power point in Watts, $Solar\ Energy$ is the incident solar energy on the solar cell in Watts per meter squared, and $Area$ is the area of the solar cell exposed to the solar energy in meters squared.

The plan for this work was to measure the efficiency of the solar cell fabricated from the highly-phosphorus doped silicon sample and compare it to a similarly constructed crystalline solar cell.

4. Results and Discussion

4.1. Hall Measurement Results

Hall measurement was the first choice for characterization to determine the number of active charge carriers. Hall measurement was presented as a rather simple tool to utilize and understand the results. The initial training on this led to dismal first results. The initial Hall measurement results were not consistent from sample to sample. After further consultation with other Hall system users, some adjustments were made in the method of contact formation and the sweep current used during sample measurements.

Additional training and a properly operating system and meter led to improved results. It became apparent from the training and more measurements that contact formation was the limiting factor for optimal results. Contact formation was practiced on many types of materials such as aluminum, glass, and silicon substrates. The contact preparation of the Si:P samples was found to provide the most reliable contact. This was likely due to the high phosphorus content that tended to provide a metal-like surface for the contact to adhere as low resistivity materials such as the Si:P samples tended to be wetted more easily by the melted indium that was used for contact formation.

The process of contact formation was difficult, and many techniques were attempted to provide the best contact. A technique was found that produced a low profile contact that could not be removed without some form of etching. This technique was the final step in producing reliable results and a process that could provide a Hall measurement of a sample in less than thirty minutes.

Phosphorus is a donor in silicon. Because of this, it is expected that the resistivity would decrease monotonically with an increase in phosphorus concentration. For this reason, each

characteristic measured or calculated from the Hall measurement was plotted against atomic percent concentration determined by ASM Company. The resistivity and carrier concentration plotted with phosphorus concentration are shown in Figure 4.1.
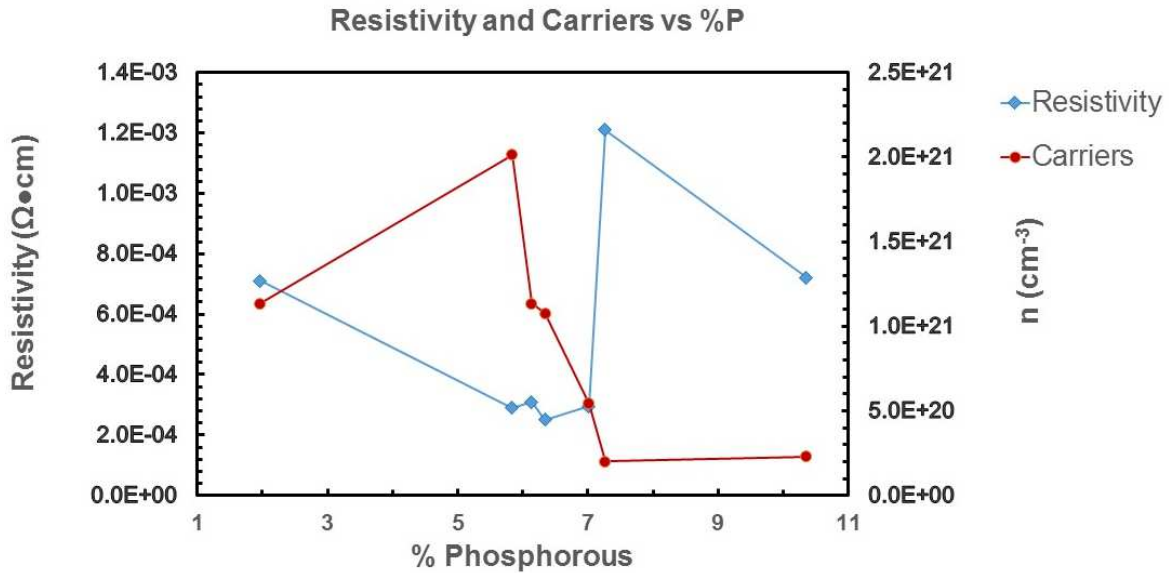
Figure 4:1: Resistivity and Carriers vs P Concentration

The expected result of resistivity and carrier concentration versus phosphorus concentration was a decrease in resistivity as the carrier concentration increased. This expectation was based on the relation that as active charge carriers are increased, the increased free electrons should decrease resistivity. From Figure 4.1, this expectation resulted with samples that contained two to seven atomic percent of phosphorus. A shift up in resistivity occurred near seven percent phosphorus and then another trend of decreasing resistivity with increasing phosphorus concentration occurred above seven percent phosphorus concentration. There may be several possibilities that explain this result.

One possibility that would explain an increase in resistivity with an increase in charge carriers is a change in material quality. If material defects were increased, such as precipitates formed, resistivity would increase due to a reduction in charge carriers that result from defects.

Another explanation may be related to sample thickness. As sample thickness is reduced, the four point probe could penetrate the sample and enter the bulk region, which would allow test current to flow directly through the substrate. For the Hall system measurements, the formation of the contact by soldering could also penetrate the sample for thinner samples. This explanation came from experience with multiple measurements where probe pressure was varied and a resistivity change was noted. This particular effect was avoided in later measurements by selecting samples with thicknesses closer to 100 nm.

Another consideration was the resistivity of the substrate. For a low resistivity substrate, a shunt resistance may dominate the resistivity measurements. The substrate resistivity measured 15.34 $\Omega \bullet$cm. The film resistivity ranged from 0.2 to 0.7 m$\Omega \bullet$cm. This was a difference of four orders of magnitude, a range that would indicate the substrate would not measurably impact the film measurements. Further consideration of the Hall measurement results is shown by plotting the mobility result versus atomic percent concentration of phosphorus. This result is shown in Figure 4.2.

The mobility plot follows a similar trend to that of resistivity which is to be expected. As phosphorus concentration increases, ionized impurities increase which decrease mobility. As previous plots have shown, the mobility plot also shows a shift in the trend near seven percent phosphorus concentration. Again, this would likely be attributed to an increase in material defects.

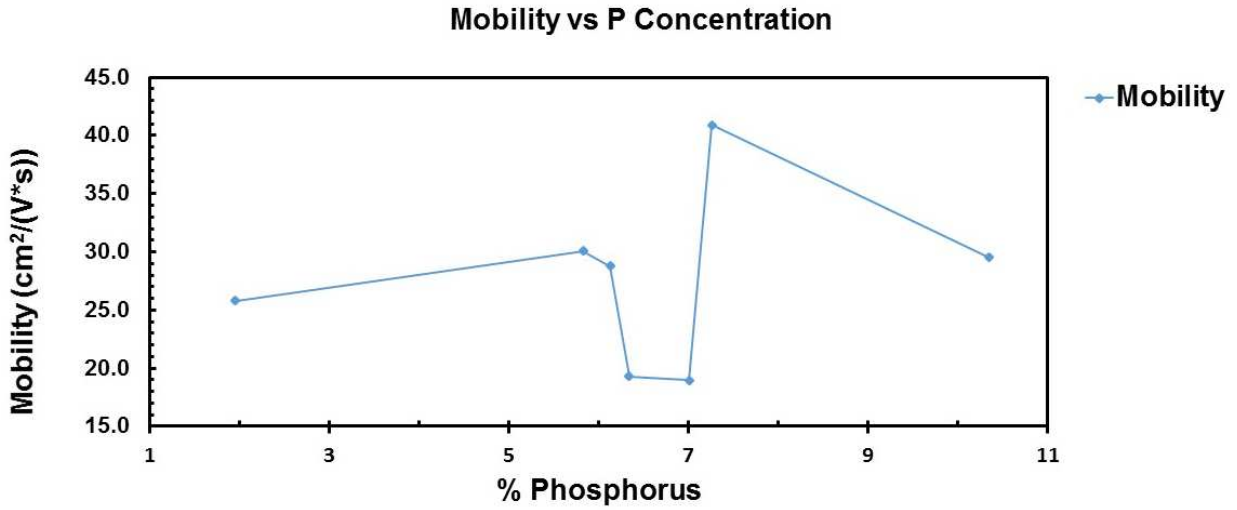Figure 4:2: Mobility vs P Concentration

The idea that sample thickness was a relevant factor seemed significant after many Hall measurements and resistivity measurements were made. In an attempt to better understand a possible relation to sample thickness, the sample thickness was plotted against atomic phosphorus concentration and is shown in Figure 4.3.
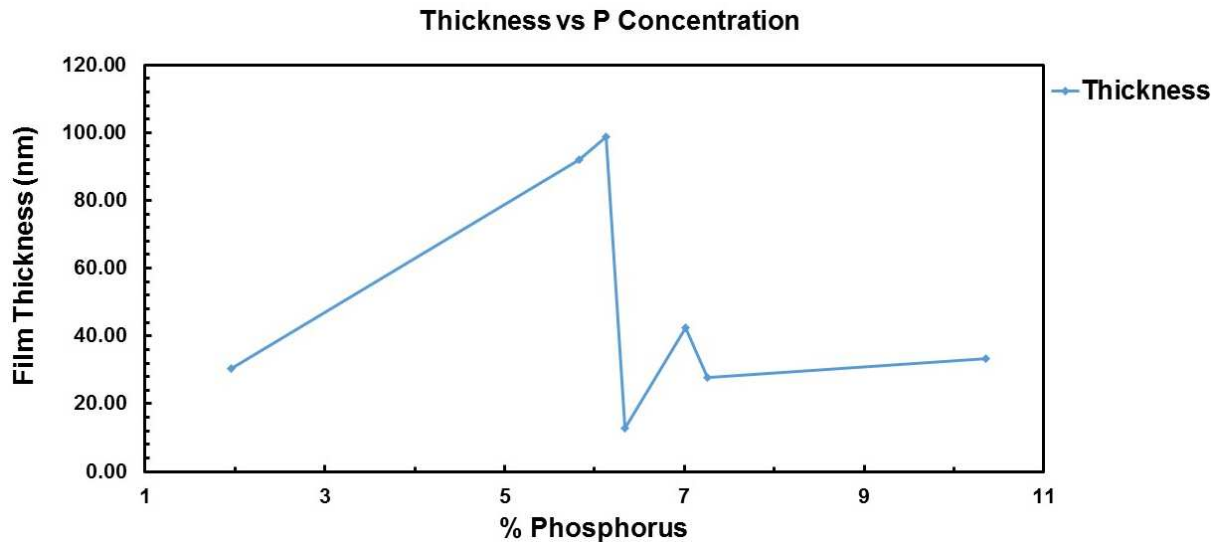

Figure 4:3: Film Thickness vs P Concentration

Figure 4.3 indicates a similar behavior to the plot of mobility versus phosphorus

concentration. Furthermore, the result appears to be a reciprocal likeness to the plot of charge

carriers versus phosphorus concentration. It may be difficult to explain this behavior, but it does

tend to give some credibility to the idea that the film thickness is an influencing factor.

The Hall measurement results from the seven samples were thought to be missing

additional trends due to the spacing and quantity of samples selected. For this reason, more

samples were selected that might add to possible trends. In selecting these samples, sample

thicknesses close to 100 nm and above were preferred as it was believed that below 100 nm,

measurement error increases dramatically.

A possible link to film thickness and the depletion region widths lead to some

calculations of the depletion regions. A hypothesis was made that for thin samples such as 12

nm, the depletion regions created at the p-n junction and the surface and contacts may dominate

by reducing the charge carriers in the film. If the n region of the layer region was within the same

order of magnitude as the film thickness, this might have an effect of reducing the charge carriers

within the film.

The depletion widths were calculated for the n+ films to assess the impact the depletion

region has on the total charge carriers for the films. Because the films are n+, the donor atoms,

N_d, are much greater than the acceptor atoms, N_a, and the relations in Equation 4.1 and Equation

4.2 applies.

$$N_d \gg N_a \qquad\qquad \text{(Equation 4.1)}$$

$$W_p \approx W_d \approx \sqrt{\frac{2\epsilon(Vc+Vr)}{qNa}} \qquad\qquad \text{(Equation 4.2)}$$

When the relation in Equation 4.1 is valid, the relation in Equation 4.2 applies. Equation

4.2 defines the width of the p region and the depletion region where ϵ is the permittivity of

silicon, Vc is the contact potential, Vr is the applied voltage, and q is the charge of the electron. The contact potential is given in Equation 4.3 where k is the Boltzmann constant, T is the temperature in Kelvin, and ni is the intrinsic concentration of silicon.

$$Vc = \frac{kT}{q[\ln(\frac{NdNa}{ni^2})]}$$ (Equation 4.3)

For the above relations, the width of the n region, Wn, is calculated using the relation in Equation 4.4.

$$Wn = W_d\frac{Na}{(Na+Nd)}$$ (Equation 4.4)

The results from the calculations are shown in Table 3. The n region of the layer is four orders of magnitude smaller than the layer and, therefore, would not likely have a noticeable effect on the charge carriers in the layer. This hypothesis was an attempt to establish a reason for the change in resistivity for samples of the same concentration but different layer thicknesses. Once this process of evaluating the effect of the depletion layers was completed, the additional Hall measurement results were tabulated and shown in Table 4.

Two sample results shown in Table 4 are highlighted for an emphasis of the samples with the highest carrier concentrations. Additionally, the substrate of sample P24A15 was also measured with the result shown in Table 4.

These results were compared to the atomic percent concentration of phosphorus in an effort to determine a trend that may explain the effect of increasing the concentration of phosphorus. The carrier concentration comparison is shown in Figure 4.4.

The results of expanding the sample space as shown in Figure 4.4 indicate an increasing carrier concentration as the phosphorus concentration is increased as previously expected along with a shift in the trend. The sample space included all of the previous samples along with

additional samples that were near or above 100 nm. The results of carrier concentration are

shown in Figure 4.4. The results are highlighted with trend lines for clarity as shown in Figure

4.5.

Table 3: Depletion Region Width Calculation Results

SAMPLE	N_D (cm^3)	N_A (cm^3)	V_C (V)	W_d (cm)	W_n (cm)	Layer Thick. (nm)
P04A11	3.529E+20	1.00E+15	0.9244	1.098E-04	3.113E-10	118.56
P10A12	5.781E+20	1.00E+15	0.9372	1.106E-04	1.913E-10	30.48
P11A11	3.383E+20	1.00E+15	0.9233	1.098E-04	3.245E-10	290.00
P14A11	5.410E+20	1.00E+15	0.9354	1.105E-04	2.043E-10	71.05
P16A11	7.905E+20	1.00E+15	0.9452	1.111E-04	1.405E-10	71.27
P18A11	1.104E+21	1.00E+15	0.9539	1.116E-04	1.011E-10	106.22
P20A12	7.294E+20	1.00E+15	0.9432	1.110E-04	1.521E-10	91.92
P21A11	7.424E+20	1.00E+15	0.9436	1.110E-04	1.495E-10	98.78
P22A11	1.350E+21	1.00E+15	0.9591	1.119E-04	8.288E-11	12.80
P24A11	9.237E+20	1.00E+15	0.9493	1.113E-04	1.205E-10	143.86
P26A11	8.580E+20	1.00E+15	0.9474	1.112E-04	1.296E-10	42.34
P27A11	2.151E+20	1.00E+15	0.9116	1.091E-04	5.071E-10	27.77
P28A11	6.656E+20	1.00E+15	0.9408	1.108E-04	1.665E-10	73.34
P30A11	7.874E+20	1.00E+15	0.9451	1.111E-04	1.411E-10	275.80
P31A11	5.015E+20	1.00E+15	0.9335	1.104E-04	2.201E-10	33.38

Table 4: Hall Measurement Results

Sample	P %	Sheet Rho	$\Omega * cm$	RH	n (cm^{-3})	Sheet Density (cm^{-2})	Hall Mobility
P04A11	0.99	38.4615	4.56E-04	-1.77E-02	3.529E+20	4.184E+15	38.79
P10A12	1.96	137.4039	4.19E-04	-1.08E-02	5.781E+20	1.762E+15	25.78
P11A11	2.03	15.6552	4.54E-04	-1.84E-02	3.383E+20	9.812E+15	40.64
P14A11	2.85	40.5348	2.88E-04	-1.15E-02	5.410E+20	3.844E+15	40.06
P16A11	4.25	34.7972	2.48E-04	-7.90E-03	7.905E+20	5.634E+15	31.84
P18A11	5.1	21.4649	2.28E-04	-5.65E-03	1.104E+21	1.173E+16	24.80
P20A12	5.83	30.9618	2.85E-04	-8.56E-03	7.294E+20	6.704E+15	30.07
P21A11	6.13	29.5874	2.92E-04	-8.41E-03	7.424E+20	7.334E+15	28.77
P22A11	6.34	187.0570	2.39E-04	-4.62E-03	1.350E+21	1.728E+15	19.31
P24A11	6.85	20.9718	3.02E-04	-6.76E-03	9.237E+20	1.329E+16	22.40
P26A11	7.01	90.6873	3.84E-04	-7.28E-03	8.580E+20	3.633E+15	18.95
P27A11	7.26	255.4433	7.09E-04	-2.90E-02	2.151E+20	5.974E+14	40.90
P28A11	8.85	39.6509	2.91E-04	-9.38E-03	6.656E+20	4.882E+15	32.25
P30A11	10.2	9.2893	2.56E-04	-7.93E-03	7.874E+20	2.172E+16	30.94
P31A11	10.35	126.2469	4.21E-04	-1.24E-02	5.015E+20	1.674E+15	29.54
P24A15 Substrat		383.5000	1.53E+01	6.56E+03	9.512E+14	3.805E+13	427.82

The carrier concentration had an increasing trend from 0.99 to 6.85%, then an abrupt shift downward, and then another shift upward. The previously described shift in the trend is near 7% phosphorus concentration.

The next parameter that was compared with phosphorus concentration was Hall mobility. The results are shown in Figure 4.6. The Hall mobility comparison with phosphorus concentration shown in Figure 4.6 indicates a downward trend for samples between 0.99 and 7.01% with an abrupt shift at 7.01 and 7.26% followed by another downward trend. The indicated trend is highlighted with trend lines in Figure 4.7.

The previous concerns with measurements were related to the film thickness and its impact on the measurement results. These concerns were addressed in later measurements with the calculation of the sheet density. The sheet density result is not dependent on the film thickness, and therefore it was thought that a trend may be evident from this parameter. The result of the sheet density comparison with the phosphorous concentration added no additional trends that have not clearly been described.

4.2. X-Ray Diffraction Results

The initial consideration for the X-ray Diffraction (XRD) measurements was setting the scan to detect a peak that would be related to the presence of phosphorus. During training on the XRD, multiple attempts led to little result. The decision was made to remove as much filtering as possible, such as k_α and k_β, to identify peaks. The result of the highest phosphorus doped sample is shown in Figure 4.8.

The measurement for the XRD was set to scan the two theta omega angle from 68 degrees to 83 degrees. The silicon peak is 69.1264 degrees and is the highest peak in Figure 4.8.
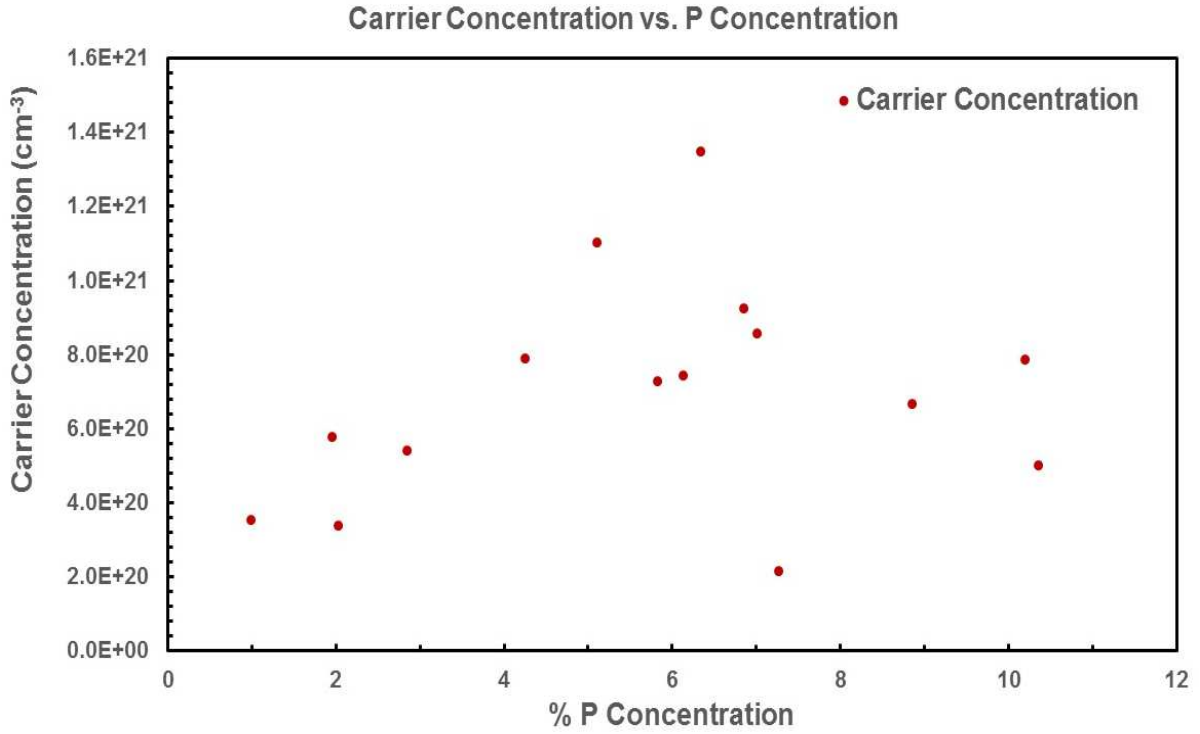
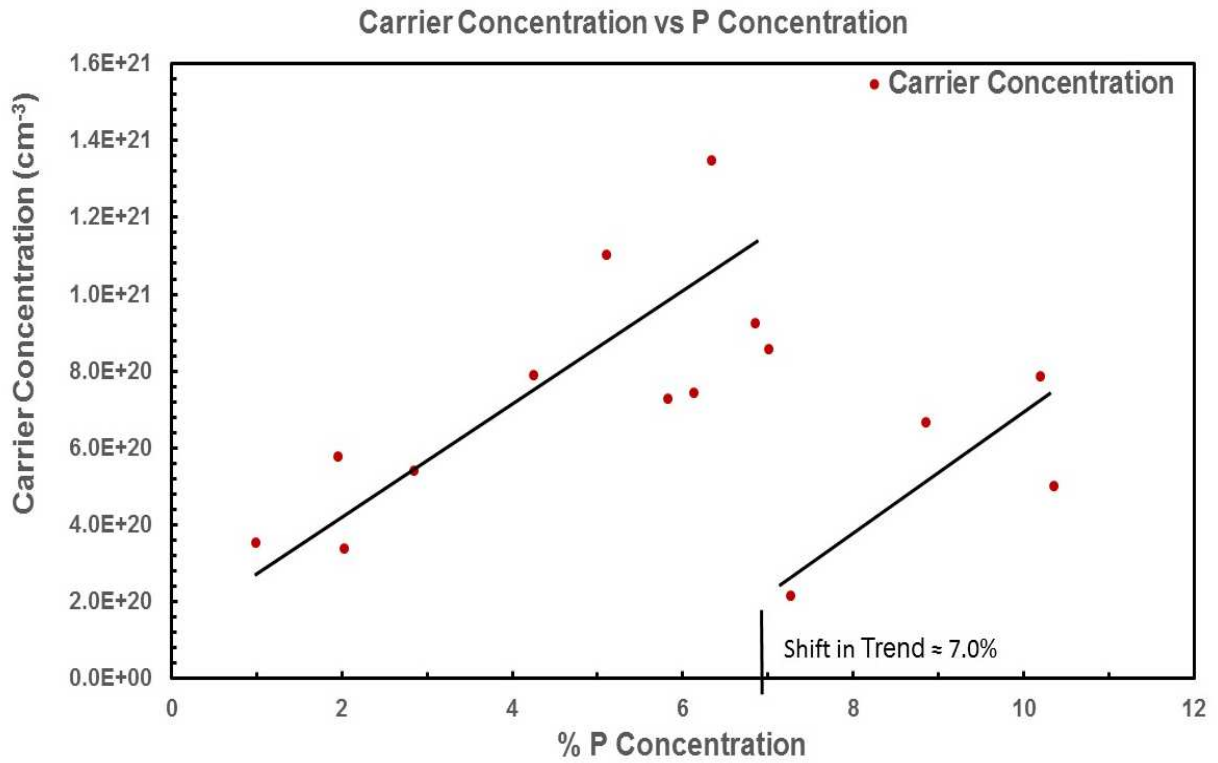Figure 4:4: Carrier Concentration vs P Concentration

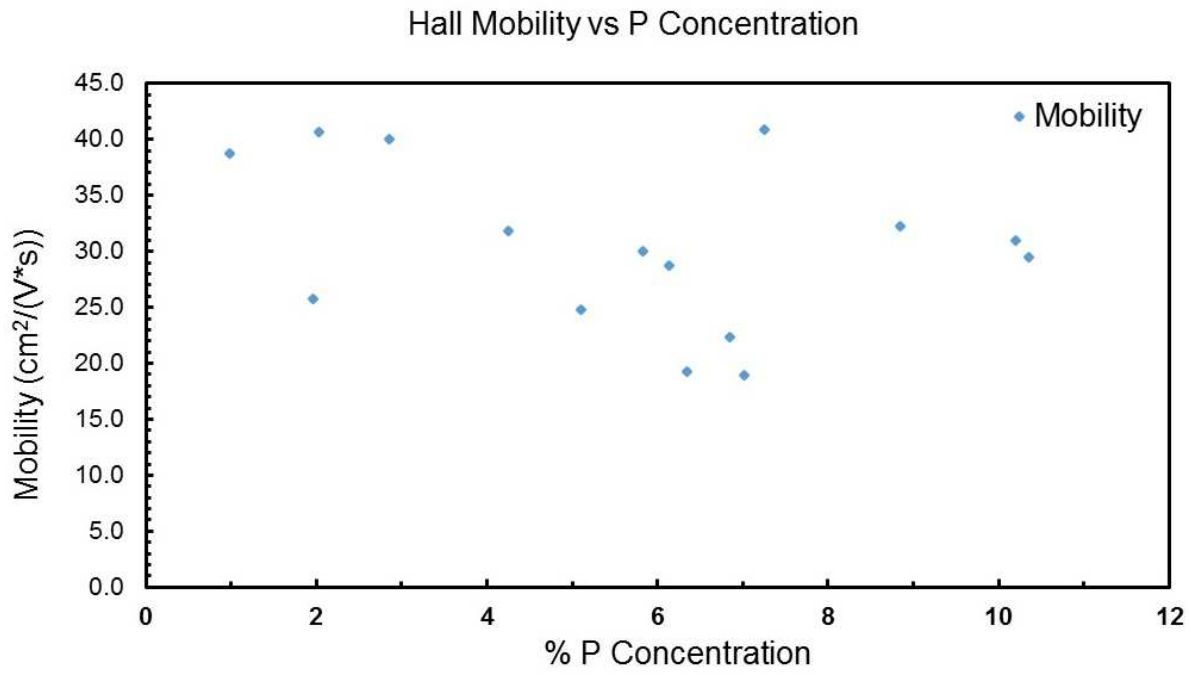Figure 4:5: Carrier Concentration vs P Concentration with Trend

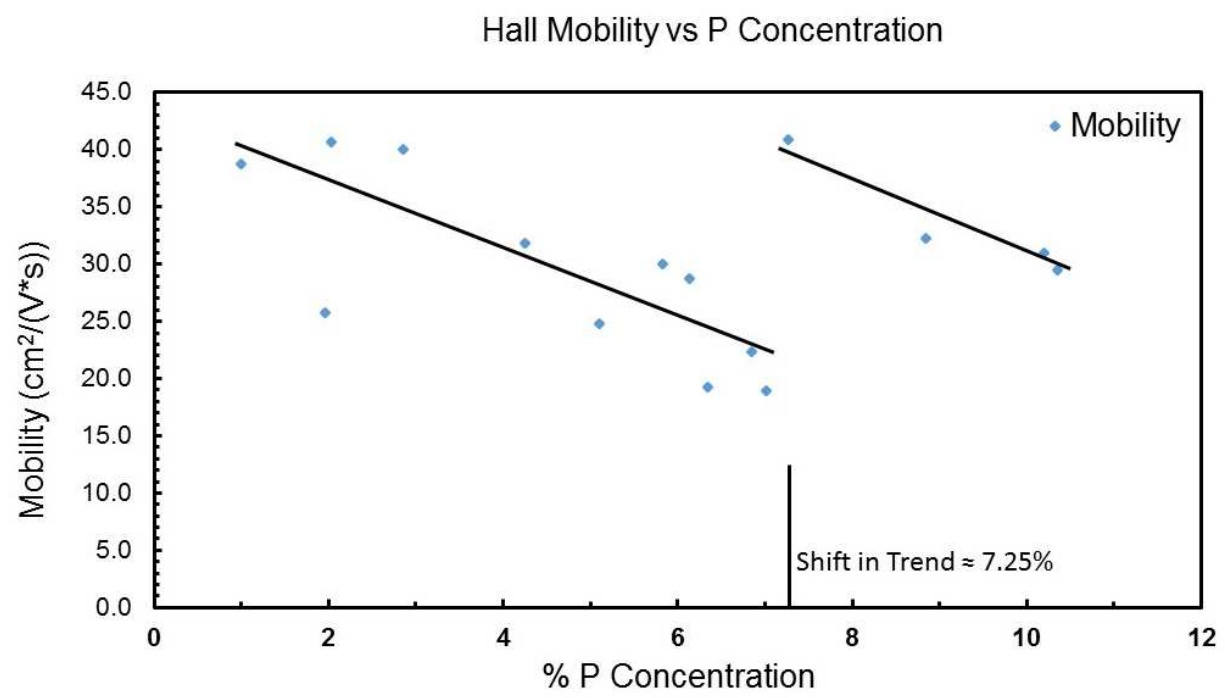Figure 4:6: Hall Mobility vs P Concentration

Figure 4:7: Hall Mobility vs P Concentration with Trend

Some of the remaining peaks were believed to be of various process characteristics with one being a possible result of the phosphorus content. A detailed description of the peaks is shown in Figure 4.9.

The k α and kβ peaks shown in Figure 4.9 were initially assumed to be caused by the filtering that was disabled for the scans. From an article on silicon phosphorus alloys that utilized first principles, [19] a two theta omega peak was expected to occur between 74 and 76 degrees. Further research without a definitive answer to the meaning of the peaks between 75 and 76 degrees motivated the scanning of intrinsic silicon using the same scan protocol that was used to produce the result in Figure 4.9. The purpose of this scan was to compare any characteristic peaks with those shown in Figure 4.9.

The result of comparing an intrinsic silicon sample with the silicon phosphorus sample was quite unexpected. The result of this scan proved to be directional in how the research on the samples continued. The result of this scan along with the scan of the silicon phosphorus sample is shown in Figure 4.10.

Figure 4:8: XRD of Sample P31A11

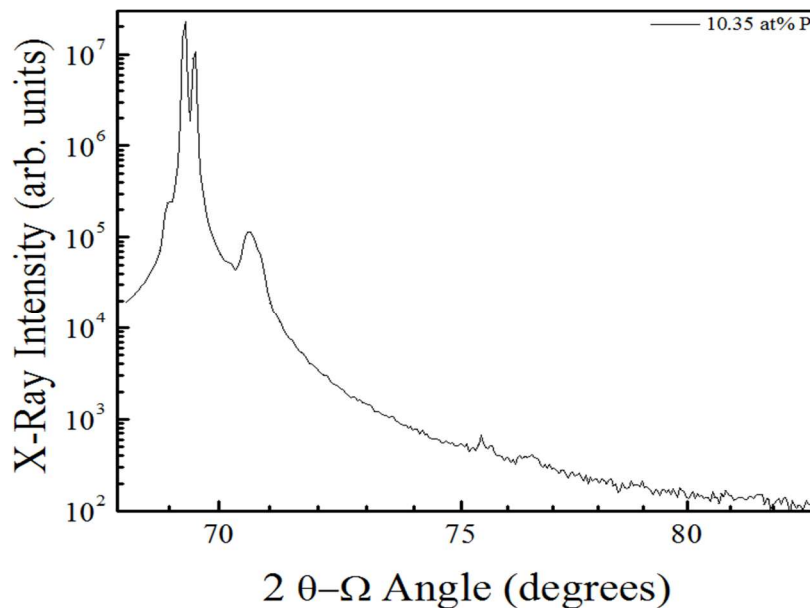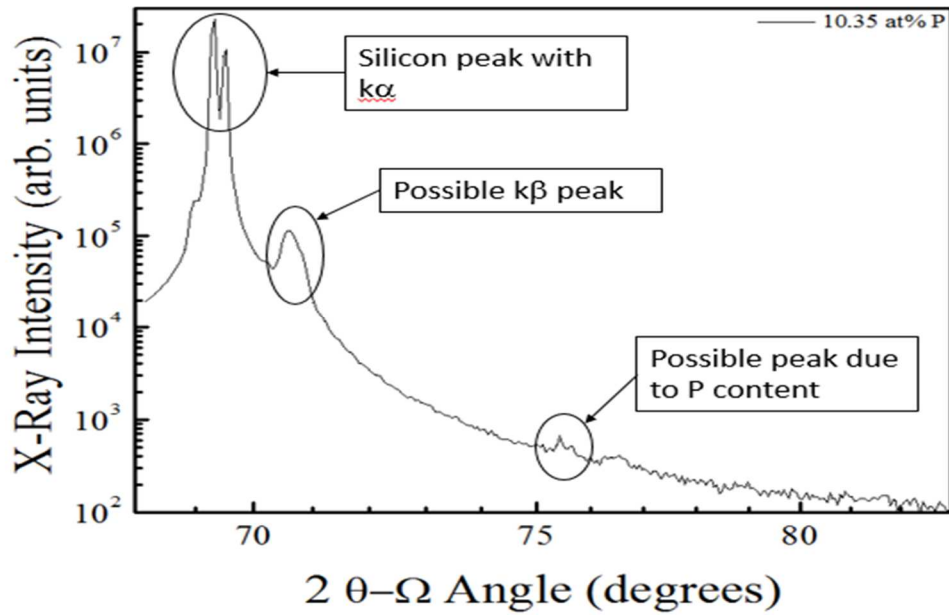Figure 4:9: XRD results with Peak Description

The XRD two-theta omega scan result shown in Figure 4.10 clearly identified the peaks
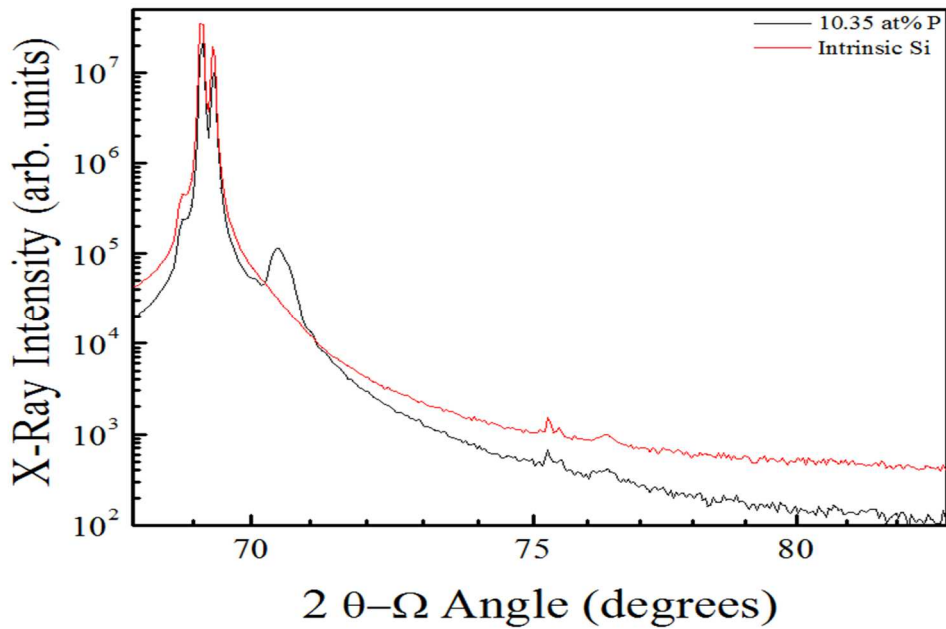
Figure 4:10: Comparison of XRD scans P31A11 and Intrinsic Silicon

near 75 degrees as characteristic of silicon, not the presence of phosphorus as initially suspected.

It was believed that these peaks were an artifact being produced from the high intensity of the

unfiltered scans. This result influenced the decision to look at other characterization tools for more understanding of this material.

The experience of work related to germanium tin alloy growth led to a greater understanding of XRD, its use in analyzing materials, and better techniques for discovering the details of the crystal structure of materials. Because of this experience, the samples were later scanned once more using the two theta omega scan. The outcome of this scan produced a more meaningful result and is shown in Figure 4.11.
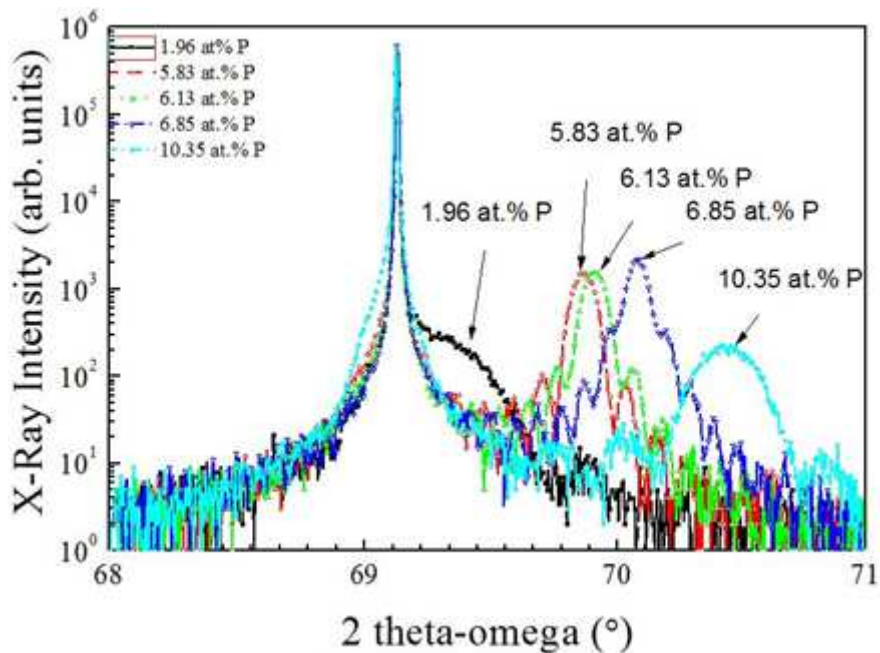
Figure 4:11: XRD Two Theta Omega Scan of Samples P10, P20, P21, P24, and P31

The results shown in Figure 4.11 provided a substantial amount of information which will be detailed. The first and likely the most applicable comment is the XRD two theta omega scan, the coupled scan, is a relatively simple technique, once learned, that can quickly and easily estimate elemental content, film thickness, strain, and crystal quality.

The silicon substrate peak is clearly shown as the sharpest peak for all samples at 69.1264°. These characteristics tend to describe a high-quality thick crystalline material. The larger, mid-intensity peaks are the Si:P film peaks.

These peaks have various intensities and peak widths that give some indication of crystal quality, film thickness, and percent of phosphorus content. The peaks below the mid-level peaks that show cyclic behavior are the interference fringe peaks. The fringe peaks indicate high-quality epitaxial films.

The application of Vegard's law can be used as an estimate of film thickness, and strain can be determined. The result in Figure 4.11 indicates an increase in phosphorus concentration as the two theta omega angle is increased. The results of this characterization are used to calculate the lattice constant and are shown in Figure 4.12.
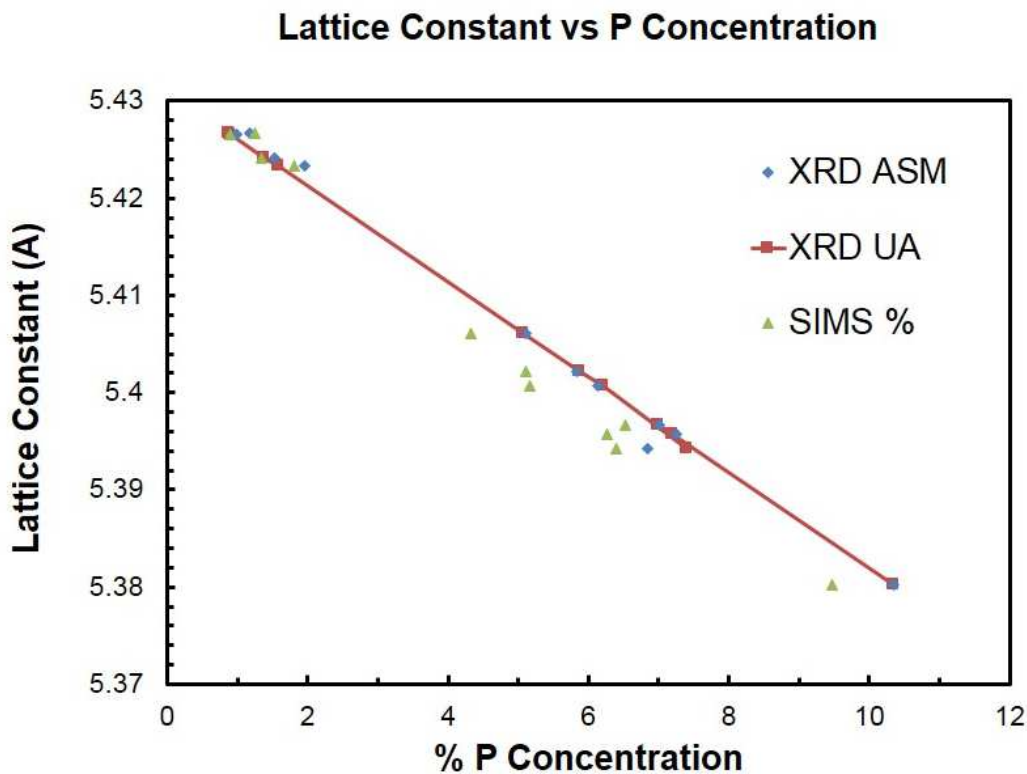
Figure 4:12 Lattice Constant vs. % P Concentration

4.3. Electrochemical Capacitive-Voltage Profiling Results

The electrochemical capacitive-voltage profiling was completed on one sample, number P24A13. The results are shown in Figure 4.13.

Figure 4.13 shows the carrier concentration in the top 33 nm layer is approximately $4.3 \times 10^{20}/cm^3$. At this depth, the carrier concentration drops distinctively to approximately $5 \times 10^{18}/cm^3$. There is another distinctive reduction in carrier concentration at 190 nm. The carrier concentration is near the estimated bulk of 10^{15} to $10^{16}/cm^3$ at approximately $3.1 \times 10^{16}/cm^3$. The results of EC-V profile are compared to other data in Table 5.

The carrier concentration result from the Hall Effect measurement for sample P24A13 is $9.23 \times 10^{20}/cm^3$. The carrier concentration result from the EC-V profiling of $4.3 \times 10^{20}/cm^3$ indicates a deviation of 73% from the Hall Measurement carrier concentration result. The

Figure 4:13: Sample P24A13 E-CV Profile

54

thickness result from the EC-V profile indicates a deviation of 125% from the thickness determined from ASM America.

There are a number of factors in the EC-V measurement that may have an impact on the carrier concentration results obtained. The Nanometrics system being used required a small sealing ring for the sample which increases the error due to the contact area measurement. As the size of the sealing ring is reduced, the percent of error is increased.
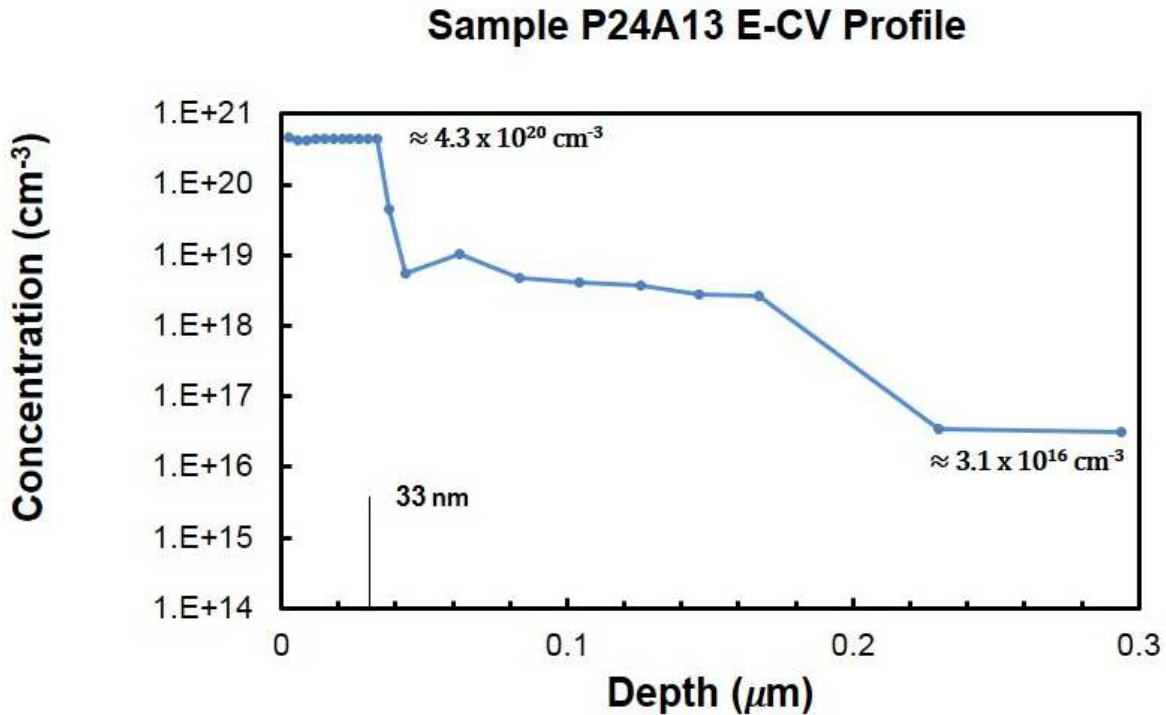
The results of the EC-V profiling did not agree with any other characterization that had been completed on the samples. As the results could not be explained, no further samples were characterized using EC-V profiling.

Table 5 Characterization Result Comparison

Characterization Type	Carrier Concentration	Sample Thickness
P24A13 Hall Measurement	$9.23 \times 10^{20}/cm^3$	Not Available
P24A11 EC-V Profiling	$4.3 \times 10^{20}/cm^3$	33 nm
P24 ASM America Result	Not Available	143.86 nm
Percent Difference	73%	125%

4.4. Raman Spectroscopy Results

The Raman characterization was completed on multiple samples multiple times. Initially, the results of the silicon phosphorus samples revealed nothing different from a scan of intrinsic silicon. It was believed that the resolution of the Raman system in the Bio-photonics lab was not adequate for detecting small differences in material properties. This assumption led to seeking Raman characterization in the Optoelectronics Laboratory. Multiple attempts were made at the

Optoelectronics Laboratory lab without any remarkable result. This result is shown in Figure 4.14.

Figure 4.14 is a comparison of the samples with an intrinsic silicon sample. The peak positions, intensities, and widths do not reveal any substantial differences. This result initially led to a belief that Raman characterization would not reveal anything remarkable. This led to a research focus away from Raman characterization and on to other material characterization methods. The previous results were modified to zoom in on the data near the Raman shift peak for intrinsic silicon. The result is shown in Figure 4.15.

Figure 4.15 reveals an additional peak for samples P18A13, 5.1% P, and P21A11, 6.13% P, near the Raman peak for intrinsic, unstressed, silicon. This additional peak could be attributed to silicon phosphorus bonds. A reduced Raman shift value would indicate lower energy bonds. It has been shown that the Si-P bond is slightly weaker than the Si-Si bond. [20] From the Raman result, a bond is formed at a slightly lower energy than the Si-Si bond which would indicate a Si-P bond. The peaks shown near 520 cm^{-1} were evaluated for changes in full width half maximum (FWHM) to infer any possible effects, as shown in Figure 4.16. The deviation shown is attributed to crystal quality.

4.5. Photoluminescence Characterization Results

The photoluminescence (PL) characterization results are shown in the following three figures. The first result, shown in Figure 4.17, is the PL intensity versus the wavelength of seven samples and an intrinsic silicon sample for a reference. The first remarkable characteristic was the peak intensity for sample P10A11. This peak was the highest of all samples. This sample was the only one that exceeded the intensity of intrinsic silicon. Initially, when this result was achieved, there was a concern that possibly the sample labeling was incorrect as it did not seem
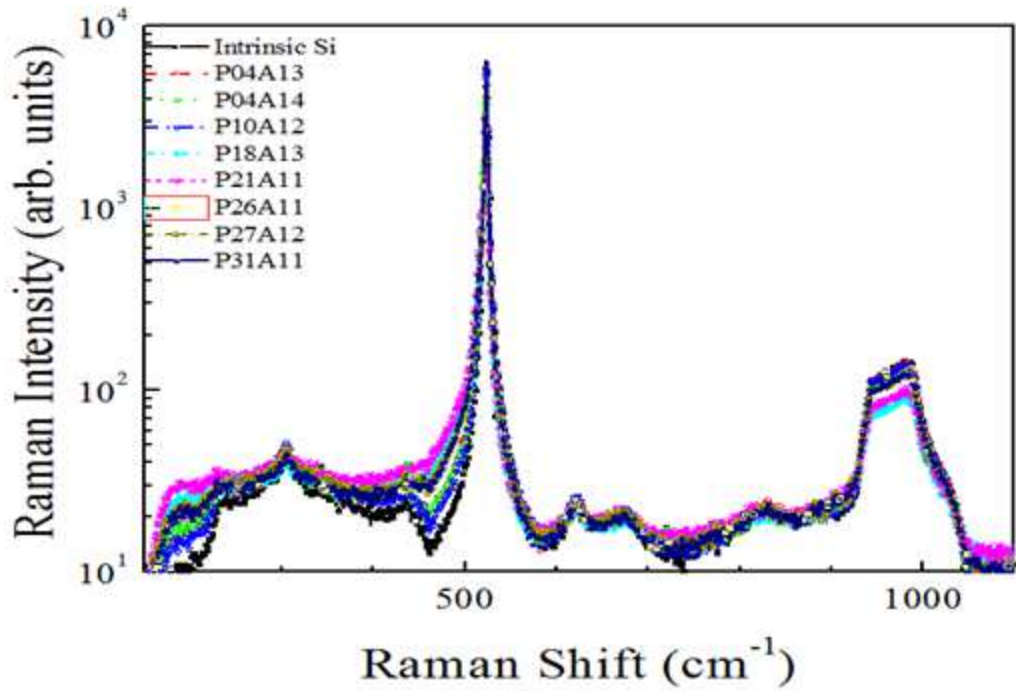
Figure 4:14: Raman Characterization for Intrinsic Silicon and samples
P4, P10, P18, P21, P26, P27 and P31
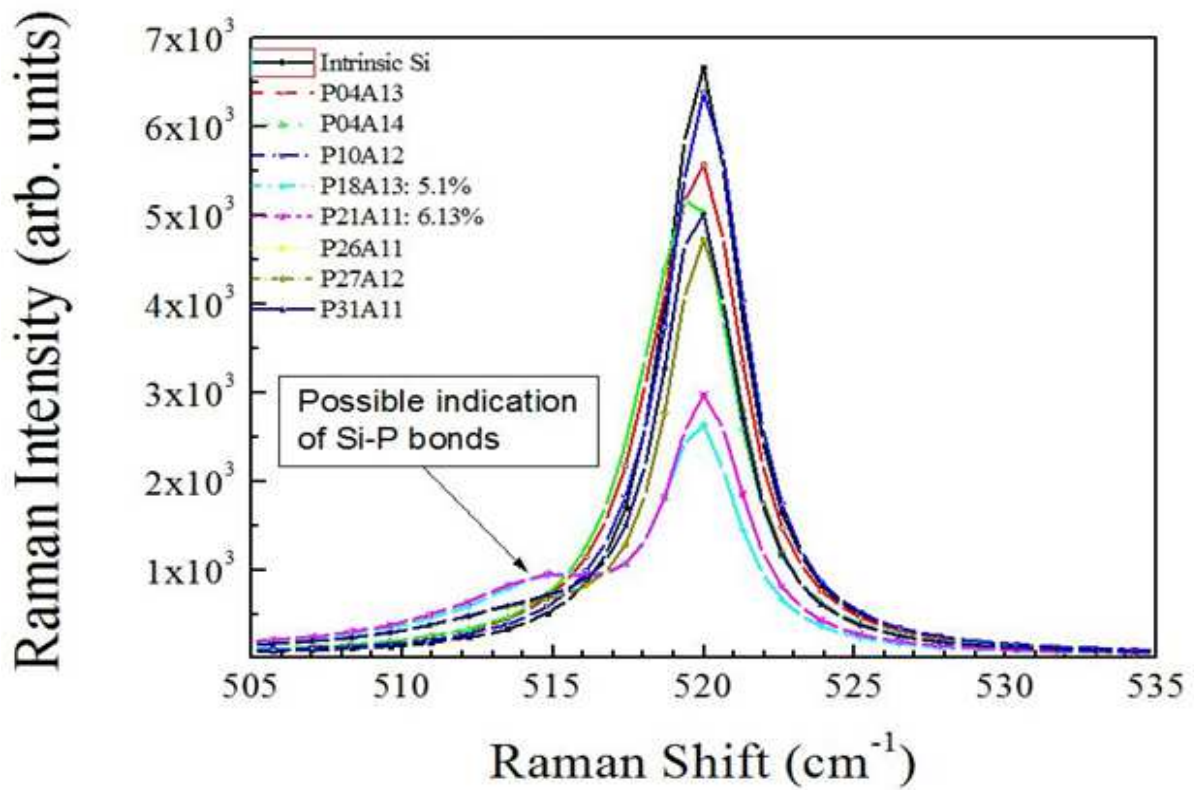
Figure 4:15: Raman Spectroscopy (Zoomed View)
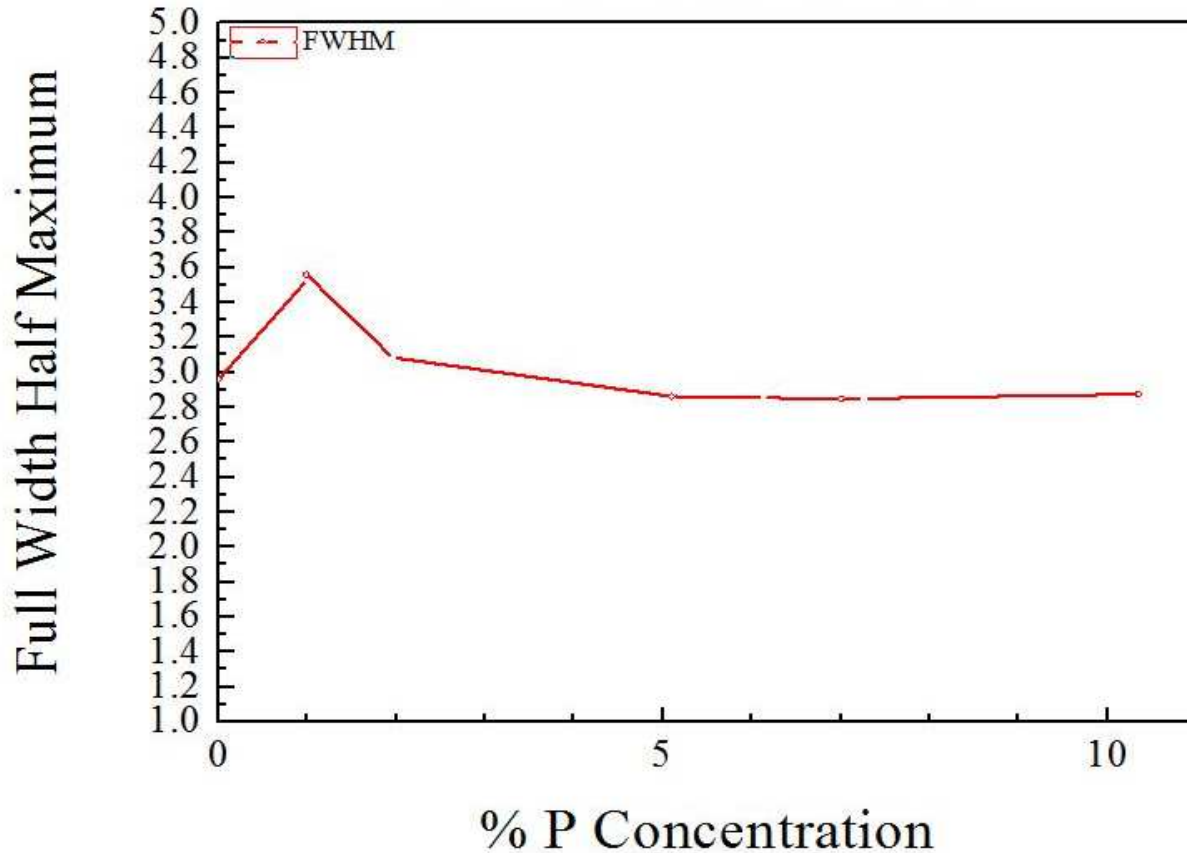
Figure 4:16: FWHM of Raman Shift

to make sense except that possibly the P10A11 crystal quality exceeded that of the intrinsic silicon sample. It is not clear how it is possible for such an alloy to have a higher crystal quality than intrinsic crystalline silicon. This result was repeated several times.

The form of the curves in Figure 4.17 were of interest as the asymmetry would typically indicate anisotropy. The fact that this also occurs for the intrinsic silicon sample may indicate some inherent measurement effect. Generally, other than intensity, the curves appear to follow the same trend. One tool to better visualize peak positions and widths, the curves can be normalized to remove effects caused by different signal intensities. The result of normalizing the data from Figure 4.17 is shown in Figure 4.18.
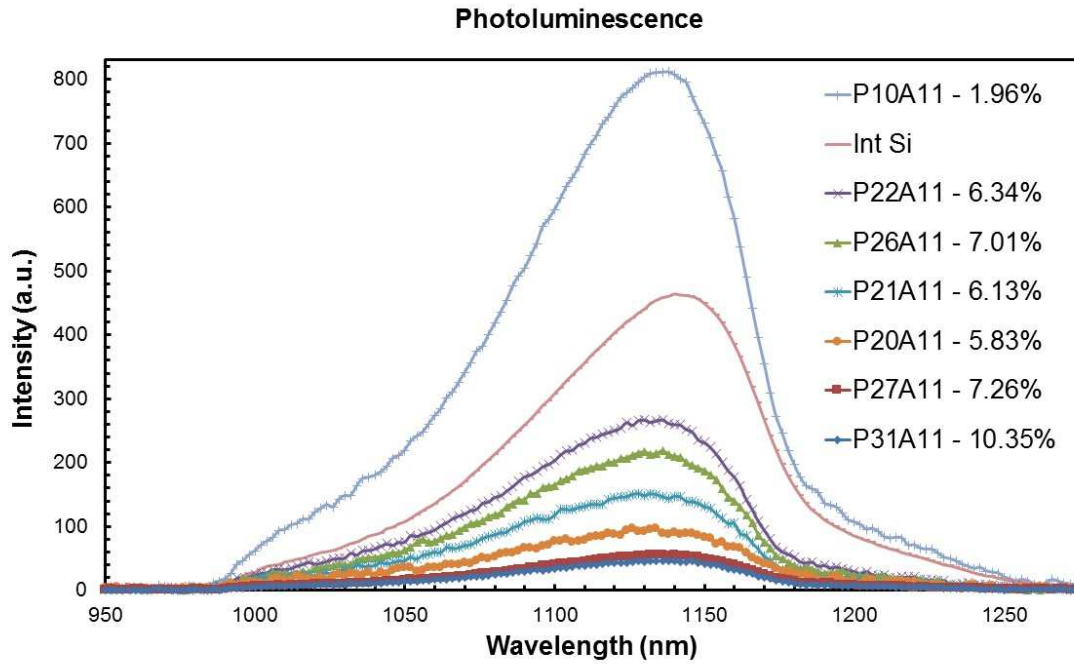
Figure 4:17: PL Intensity vs Wavelength
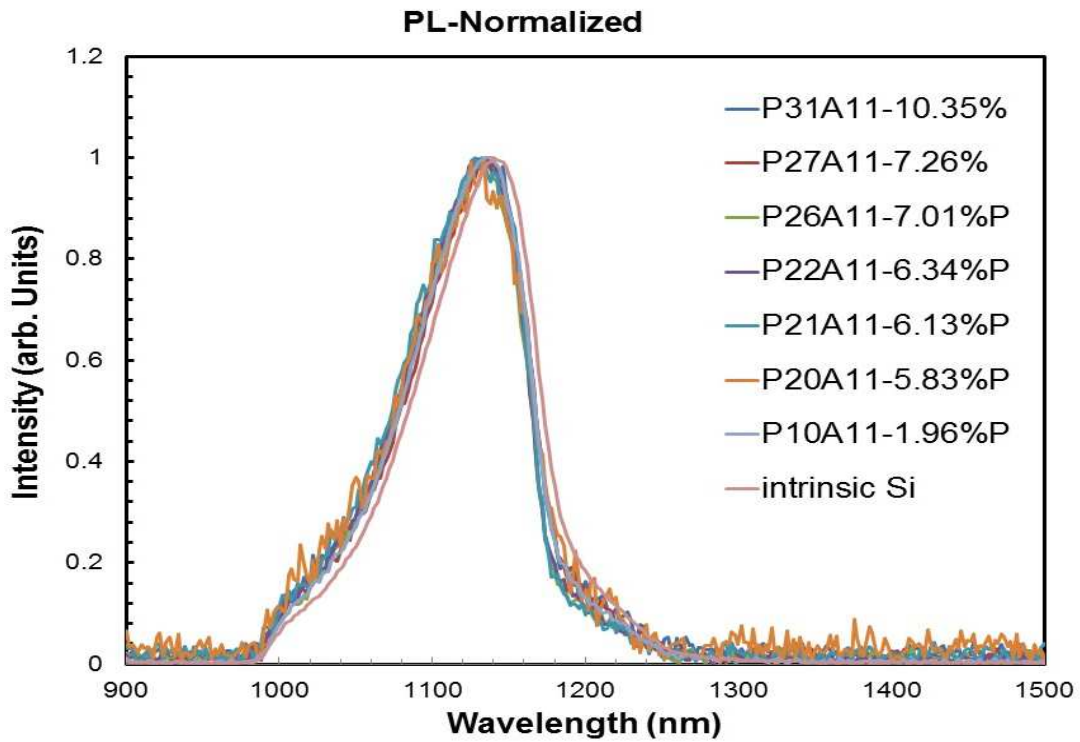
Figure 4:18: Normalized PL Intensity vs Wavelength

The result of normalizing the data shows that the curves are practically superimposed on top of each other. The shapes are identical and the peak positions are very nearly the same. From Figure 4.18, the intrinsic silicon peak is shifted by possibly only a few nanometers. This result would likely be unremarkable. To further understand this peak shift, the same data was normalized and plotted as a function of photon energy. The result of this normalization is shown in Figure 4.19.

The result of Figure 4.19 further emphasizes the minimal difference in peak position. The peak shift displayed is on the order of 0.005 to 0.01 eV. It was later discovered the PL system has a resolution of 0.2 nm, which is approximately 0.3 meV. Because of this, the peak energy of each sample was plotted with percent phosphorus concentration and is shown in Figure 4.20.

4.6. Spectroscopic Ellipsometry Results

The previous characterizations results were a determining factor in the decision on how to proceed with the ellipsometry characterizations. Although the learning process for completing a spectroscopic ellipsometry scan and the operational process was relatively simple, producing a useable result through data fitting is a complicated process to learn and then a time consuming process to complete the data fitting. Because of this, much consideration was made as to which samples would be measured using this characterization tool. Specifically, information from Hall measurement, X-ray diffraction, and Raman characterizations were used to decide which samples would be scanned with spectroscopic ellipsometry.

The results of Hall measurement shows a significant change in the trend of resistivity and carrier concentration as the atomic percent concentration of phosphorus is increased from 5.83% to 6.34% which are samples P20 and P22, respectively. Because of this, it was believed that the most useful information would come from samples on either side of this range.
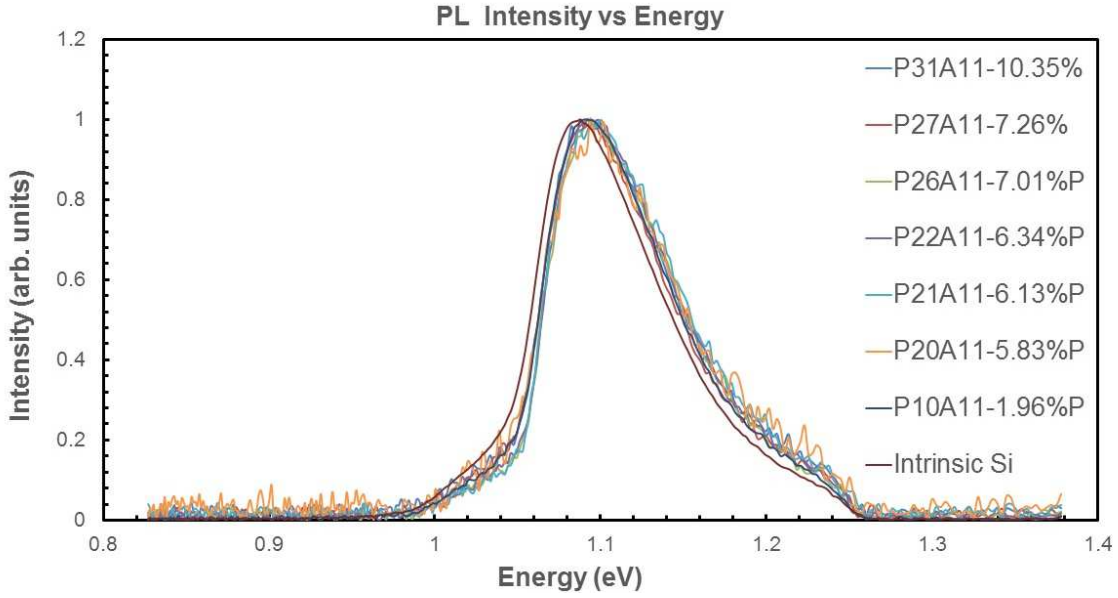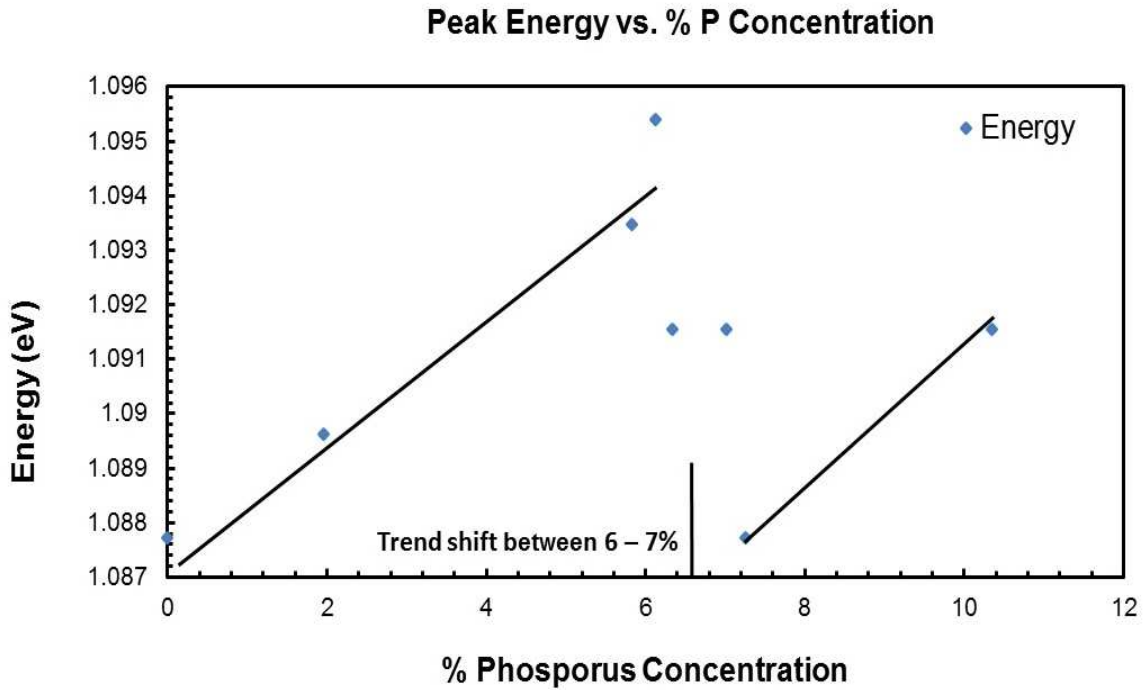
Figure 4:19: Normalized PL Intensity vs Energy

Figure 4:20: Trend Shift in Energy Transition

The X-ray diffraction result identified film thickness of samples. The film thickness proved to be an important factor with several characterization tools. As has been previously mentioned, the thinner samples, below 50 nm, proved to be difficult in providing remarkable results, and in some cases, repeatable results. For this reason, samples close to 100 nm and above were preferred.

The Raman results initially provided little indication of material characteristics that were not unlike intrinsic silicon. With a closer look, samples P18 and P20 revealed an additional peak that is certainly remarkable. For this reason, P18 was selected for spectroscopic ellipsometry. And finally, P24 was selected for its film thickness and a well-defined two theta omega peak. The data acquisition of the P18 and P24 samples was completed multiple times in the process of determining optimal scan conditions. The final obstacle to optimal scans was due to the double-sided polished samples. Because of the backside being polished, interference was occurring in the data due to the reflectance of the light from the back surface. Due to limited time, the samples were not able to be sandblasted to remove the shiny surface. The modeling software provided a filter for this reflectance the reduced this effect.

The acquired data was modeled within the Variable Angle Spectroscopic Ellipsometry (VASE) system to obtain the optical constants using a Kramers-Kronig consistent generalized oscillator layer. The ultraviolet (UV) light absorption related to electronic transition was modeled with a Cody-Lorentz oscillator and two Gaussian oscillators. A third Gaussian oscillator was attempted, but the result was not remarkable and therefore not included. The near infrared (NIR) absorption caused by free carrier absorption was modeled using a Lorentz oscillator. An additional layer was added to the model that improved the fitting process. This layer represents surface oxides, surface roughness, or both. [21]

The significance of the results can be understood by comparing them with a crystalline silicon sample as shown in Figure 4.21 and Figure 4.22. The abrupt changes or tapering of the curves to a point are called the critical points caused by high crystallinity material. The bandgap of crystalline silicon is approximately 1.12 eV, which is near 1000 nm wavelength. Below the bandgap, crystalline silicon is transparent as indicated by an extinction coefficient of k equal to zero. [21] The first ellipsometry result shown in Figure 4.23 is for sample P18A13. This result gives a spectroscopic view of the index of refraction, n, of this sample.

The comparison of the c-Silicon and the P18A13 sample indicate some specific areas that deviate from each other. In Figure 4.23, it can be seen that similar curvature continues as the wavelength is increased until just beyond 600 nm. The crystalline silicon sample curve continues a decay that began around 400 nm to an n value of approximately 3.4. Sample P18A13 does not follow a decay path beginning at 600 nm and then continues to an n value below 3.0. The fact
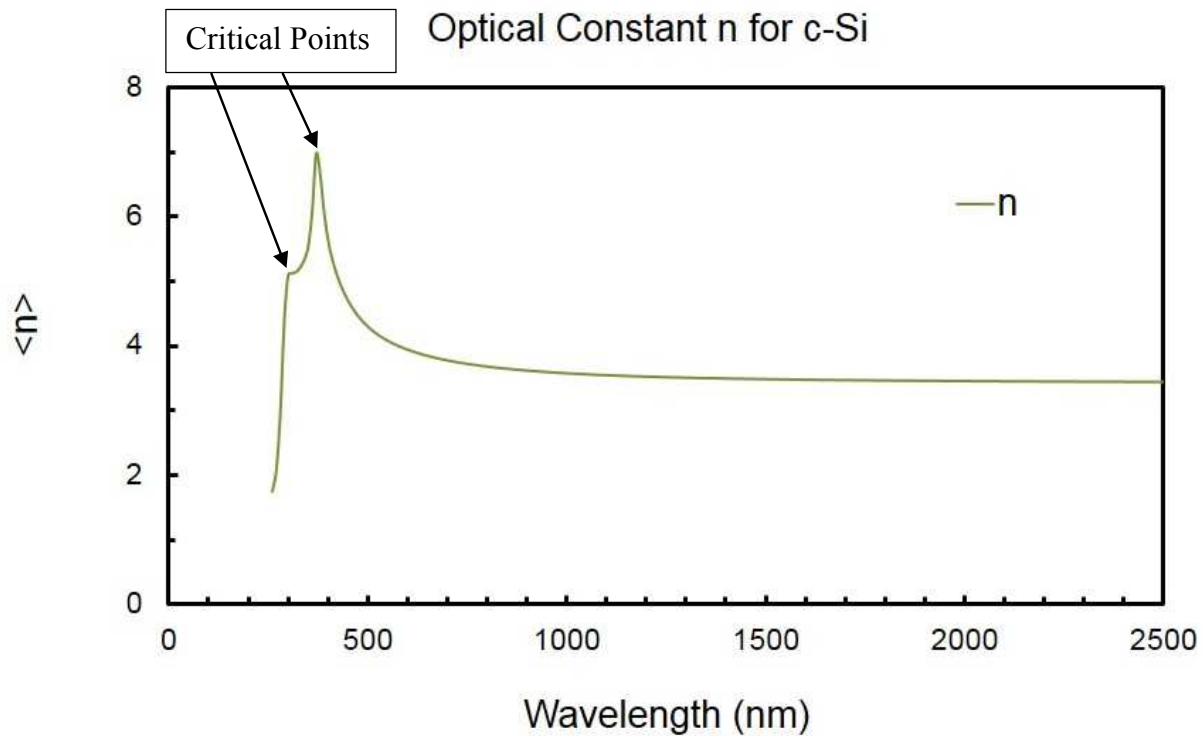
Figure 4:21: c-Silicon Index of Refraction

63
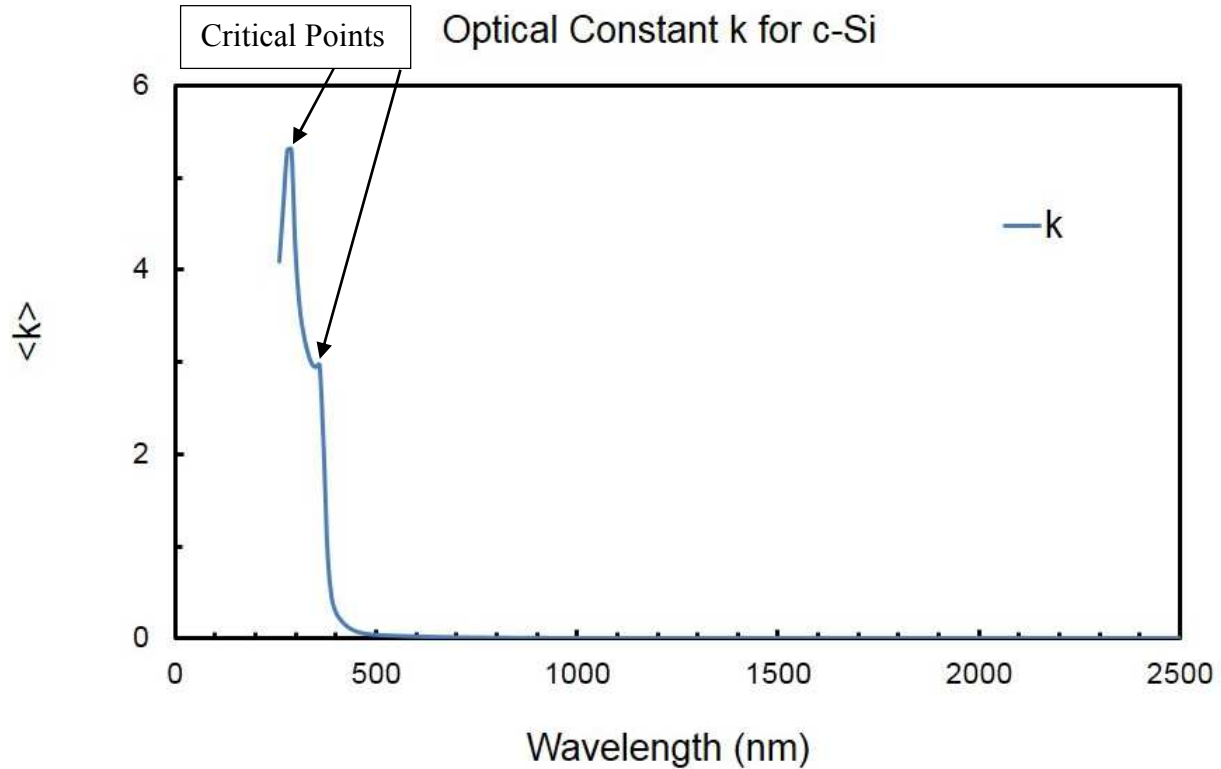
Figure 4:22: c-Silicon Extinction Coefficient

that the absorption increases as the wavelength increases indicates a Drude like absorption that is due to free carriers. Additionally, the broadening of the index of refraction curve of P18A13 is likely due to UV light absorption indicating the presence of nanocrystalline. [21]

The spectroscopic ellipsometry result for P24A13 sample is shown in Figure 4.24. Initially, the results look quite similar to the results for sample P18A13. After further consideration, there appears to be a reduction in the broadness of the index of refraction for P24A13 which would indicate less nanocrystalline material.

The two sample results have been considered at length, and a general comment may be beneficial in understanding what might be relevant. The selected samples may be on either side of a phosphorus concentration range where some phase segregation occurred.
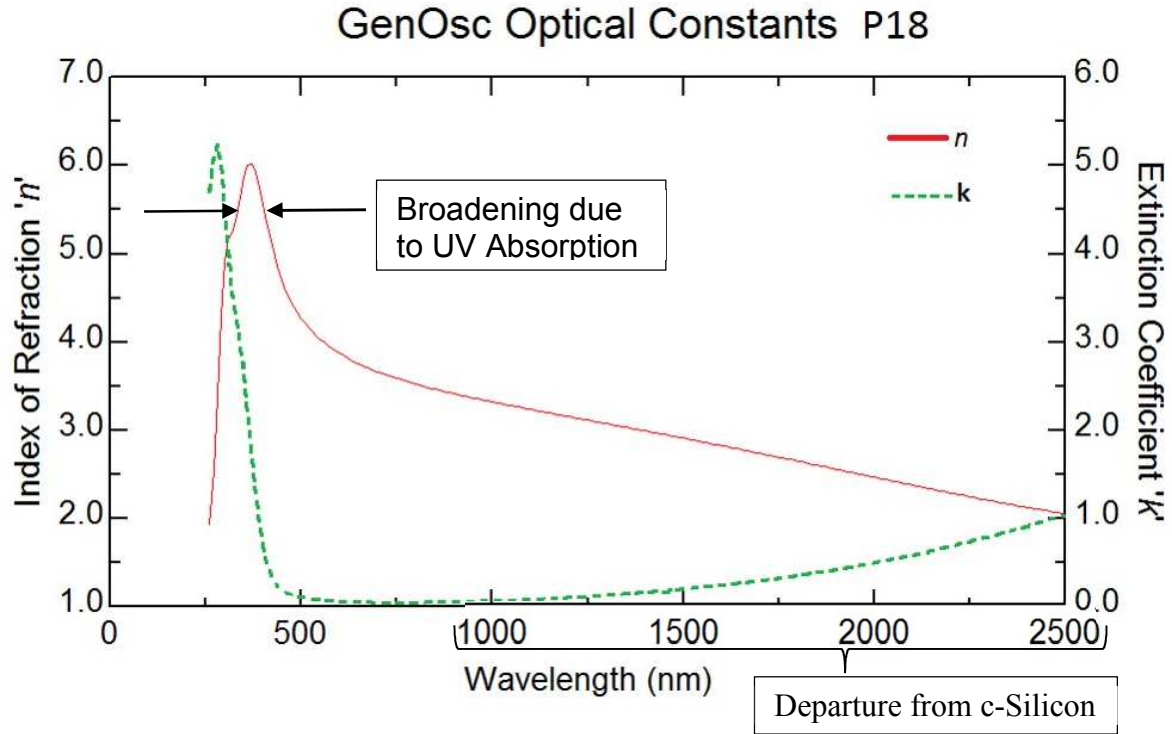
Figure 4:23: Optical Constants for Sample P18A13

4.7. Device Simulation Results

The Silvaco software has been shown to be an effective physically-based simulator. The limit for simulation is knowing the physical characteristics that may not always be available, particularly with new materials. The plan for this project was to acquire some physical characteristics of the new highly-phosphorus doped silicon and incorporate these characteristics into a solar cell simulation.

The ellipsometry scan and data fitting provided the n and k values for the Si:P material, sample P18. The plot for the n and k values are shown in Figure 4.23 and for comparison, a plot of the n and k values for crystalline silicon are shown in Figure 4.21 and Figure 4.22, respectively.

The n and k values were copied into to a text file and named SiP_real for the n data and SiP_imaginary for the k data. These two text files were included in the Si:P solar cell simulation.

GenOsc Optical Constants P24
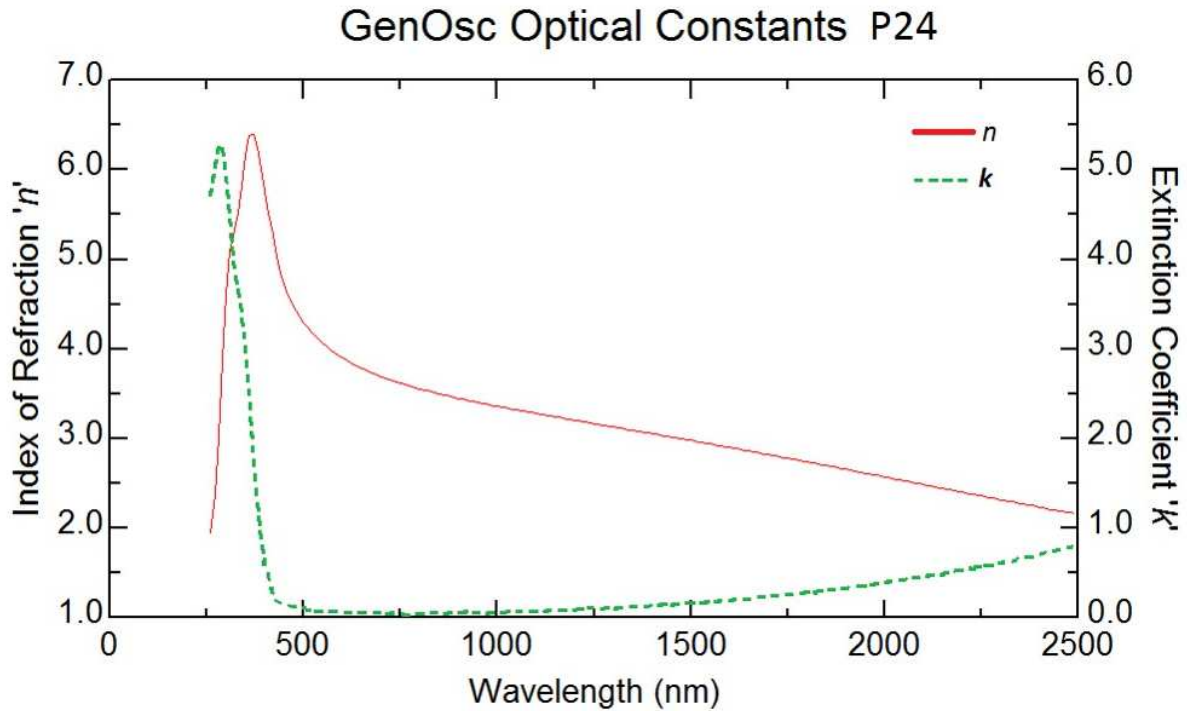
Figure 4:24: Optical Constants for P24A13

The Si:P solar cell simulation did not include device fabrication requiring process functions and therefore did not require the use of ATHENA as was the case for the first solar cell example. This example utilized the function of 'auto meshing' to create the device with the proper numerical resolution for correct simulation at the boundaries. The substrate was p-type and doped to a uniform concentration of $1x10^{14}$ cm^{-3}. The device was silicon bounded top and bottom by Tin-doped Indium Oxide (ITO) electrodes.

The device was defined as a P-i-N diode. The material parameters were modified from the default parameters to describe a crystalline silicon material with optical properties of highly-phosphorus doped silicon. The changes made included the following parameters: $Mu_n=$ 20cm^2/V·s , $Mu_p=$ 1.5cm^2/V·s , $N_c300=2.5x10^{20}$ cm^{-3}, $N_v300=2.5x10^{20}$ cm^{-3}, $E_g300=0.9$eV. The complex index of refraction for the ITO electrodes was given by the data from the Sopra database. Additionally, the recombination models implemented were Shockley-Read-Hall and

Auger recombination. The optical source was specified from above with normal incidence using

the transfer matrix method to model the optical propagation. The beam was set to AM1.5. With

these parameters set, the characterizations were able to be completed. The first output plot is

shown in Figure 4.25.
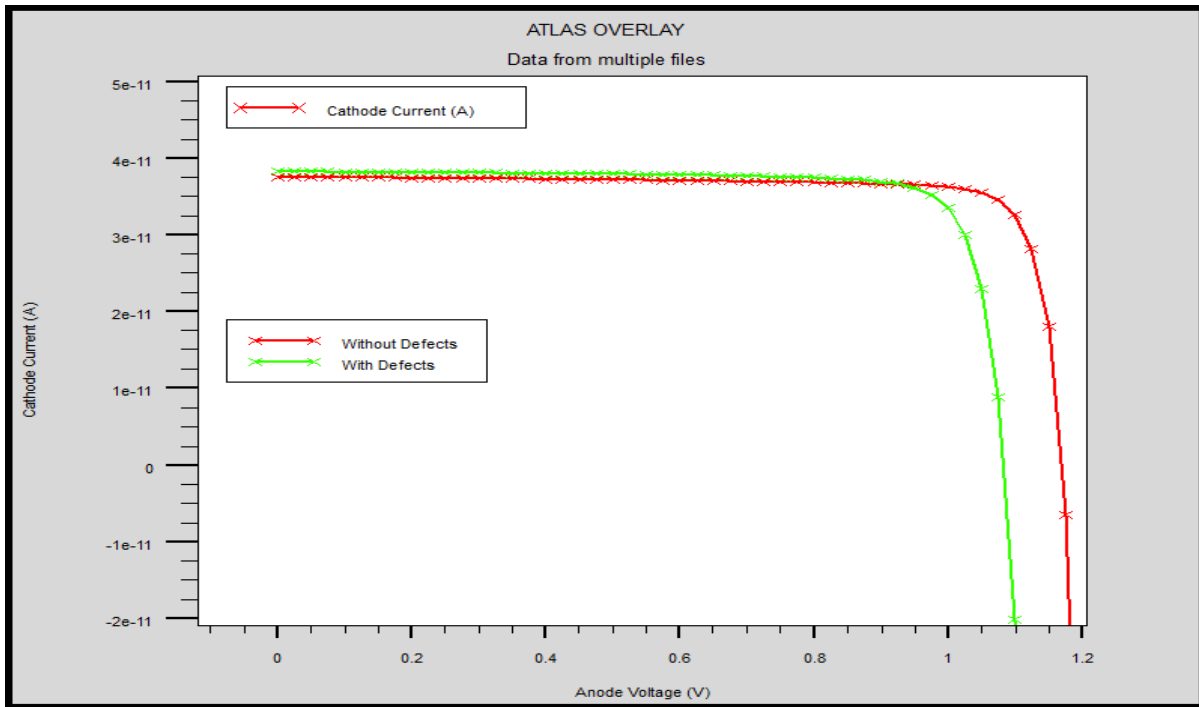
Figure 4:25: Si:P Solar Cell I-V Characteristic

The I-V curve did not show any noticeable difference with the Si:P n and k values.

Further attempts to modify the n and k values to evaluate any changes associated resulted in

errors within Atlas. An attempt was made to incorporate external quantum efficiency

measurements. This attempt produced code that failed to complete and therefore no results were

produced.

The Si:P solar cell simulation code included a section that simulated a silicon solar cell

with multiple device properties. This was used in the code to provide a comparison with the Si:P

solar cell. To simulate this cell, the following values were set to override the default crystalline silicon values: The mobility values were modified to $\mu_n = 20$ cm^2/V·s and $\mu_p = 1.5$ cm^2/V·s, the charge carrier densities were modified to $N_{c300} = 2.5\times10^{20}$ cm^{-3} and $N_{v300} = 2.5\times10^{20}$ cm^{-3}, and finally, the bandgap energy was set to $E_{g300} = 1.9$ eV. The comparison with the Si:P solar cell was not remarkable due the lack of noticeable difference when the Si:P n and k optical constants were incorporated as previously mentioned. The crystalline silicon simulation code enabled the ability to modify material characteristics such as mobility, charge carrier densities, and the bandgap.

The modification of the previously mentioned characteristics produced some noticeable results in the I-V characteristic. In Figures 4.26, 4.27, and 4.28, a change in the I-V curves with a change in bandgap energy is indicated. It should be noted that the labels for the plots were not modified due to code structure under the Window OS environment. The plot associated with the change in bandgap energy is label 'without defects'.

4.8. Device Fabrication and Characterization Results

Solar cell fabrication began with a simple application of a top-grid front contact and a square rear contact, both made of indium. The application of indium was done be heating the indium and sample near 170 °C. A cross section diagram is shown in Figure 4.29.

The process was a bit crude but initially seemed to be a simple solution for contacts, as the technique was successfully used to create contacts for Hall measurement characterization. Once the contacts were formed, the first I-V characterization completed was Dark I-V. The results are shown in Figure 4.30.

The results in Figure 4.30 were extraordinarily contorted from what was expected. A dark I-V curve of a solar cell is simply the diode curve produced by electrical stimulation. What is
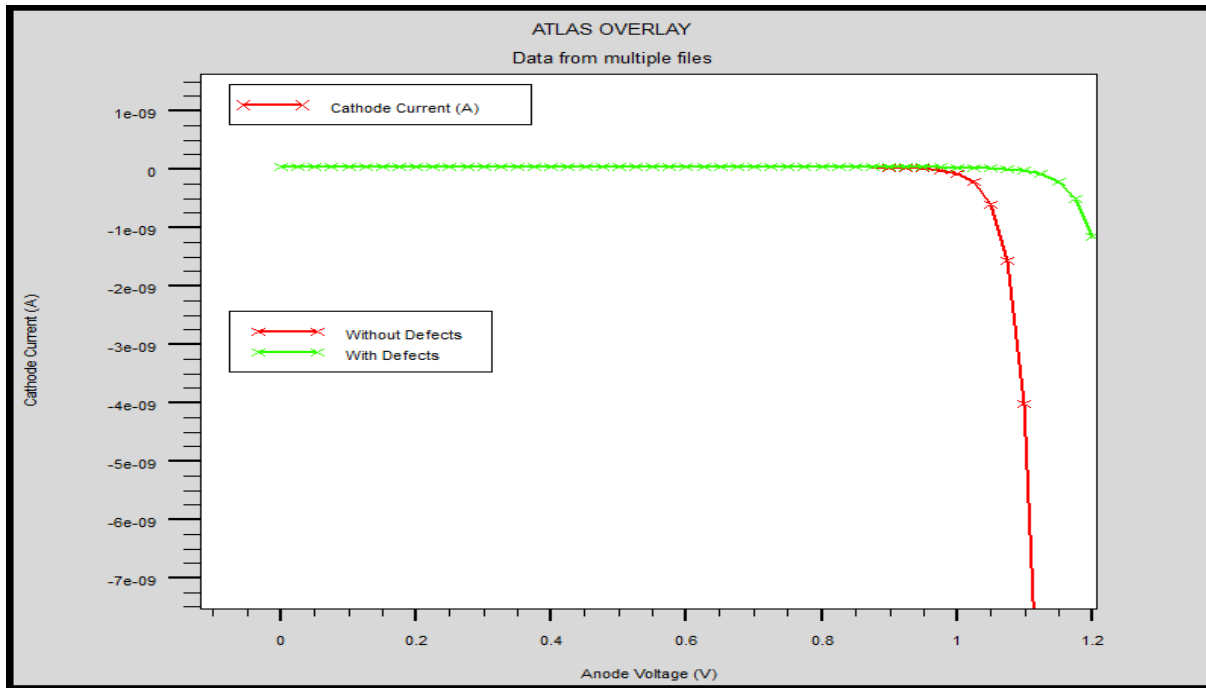
Figure 4:26: I-V curve for Eg = 1.7 eV
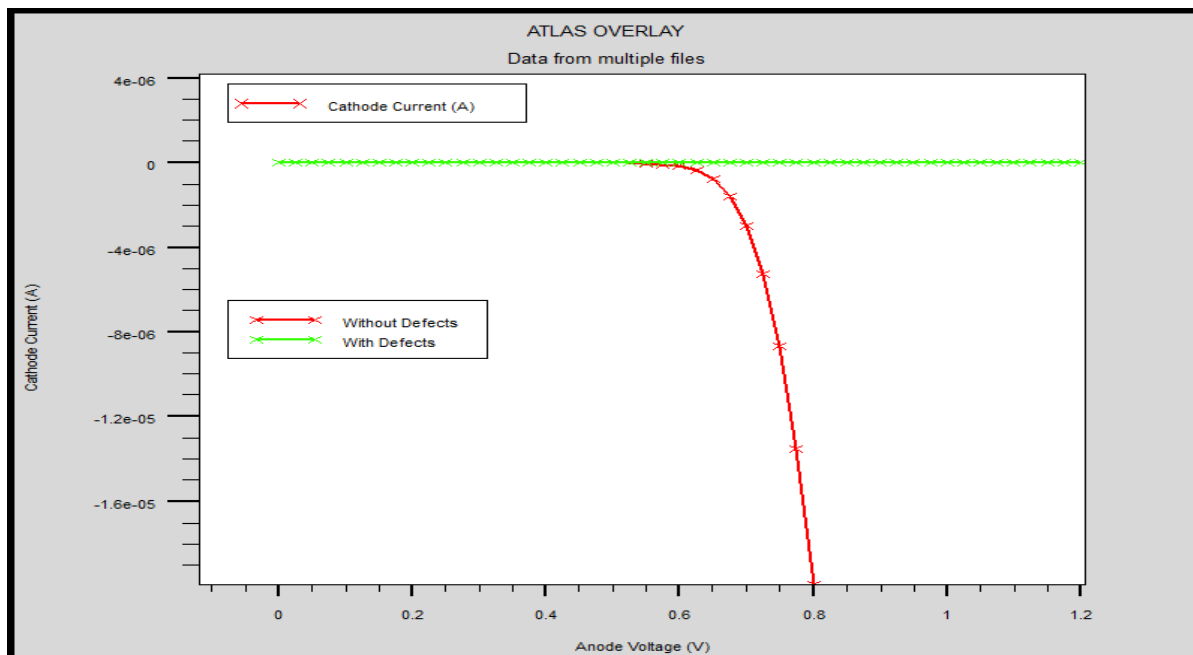
Figure 4:27: I-V Curve for Eg = 1.2 eV
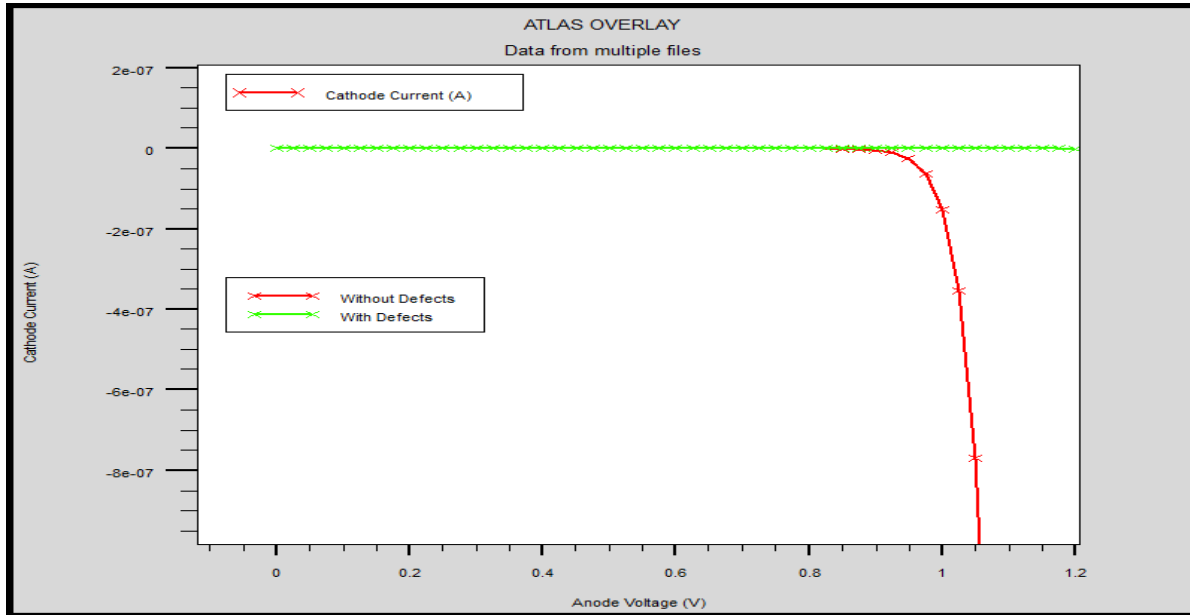
Figure 4:28: I-V Curve for Eg = 1.5 eV
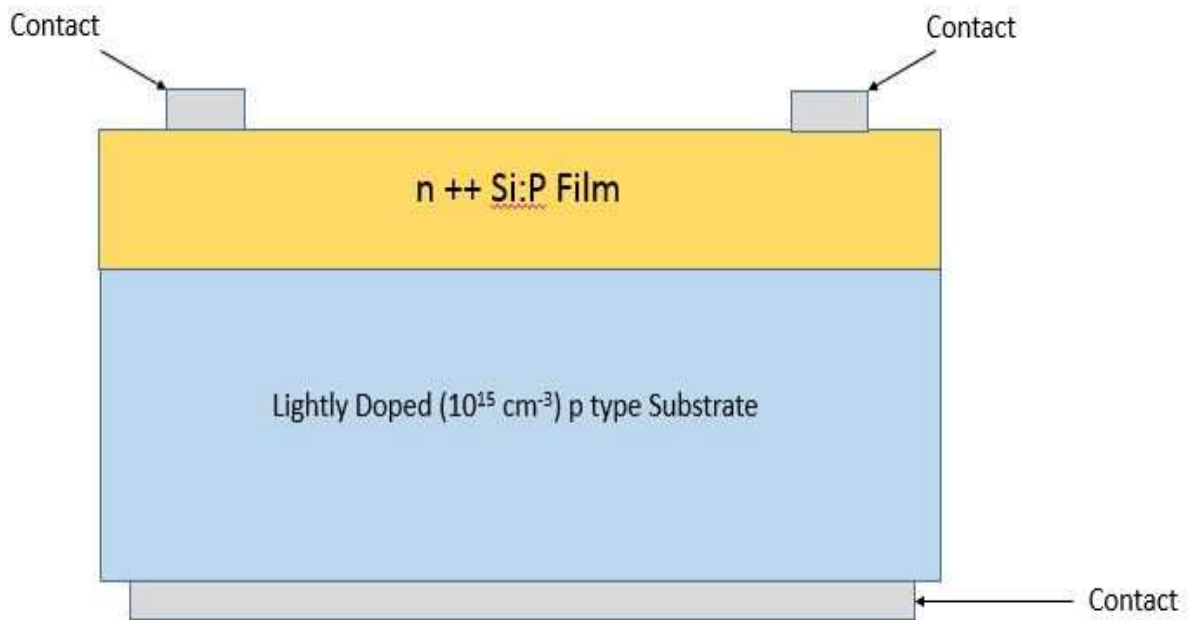
Figure 4:29: Solar Cell Cross Section

shown in Figure 4.30 has more similarity to a resistor than a diode. The first obvious assumption

is a large amount of leakage current likely due to poor contact formation. For a comparison, a

reference solar cell was measured, and the dark I-V is shown in Figure 4.31.
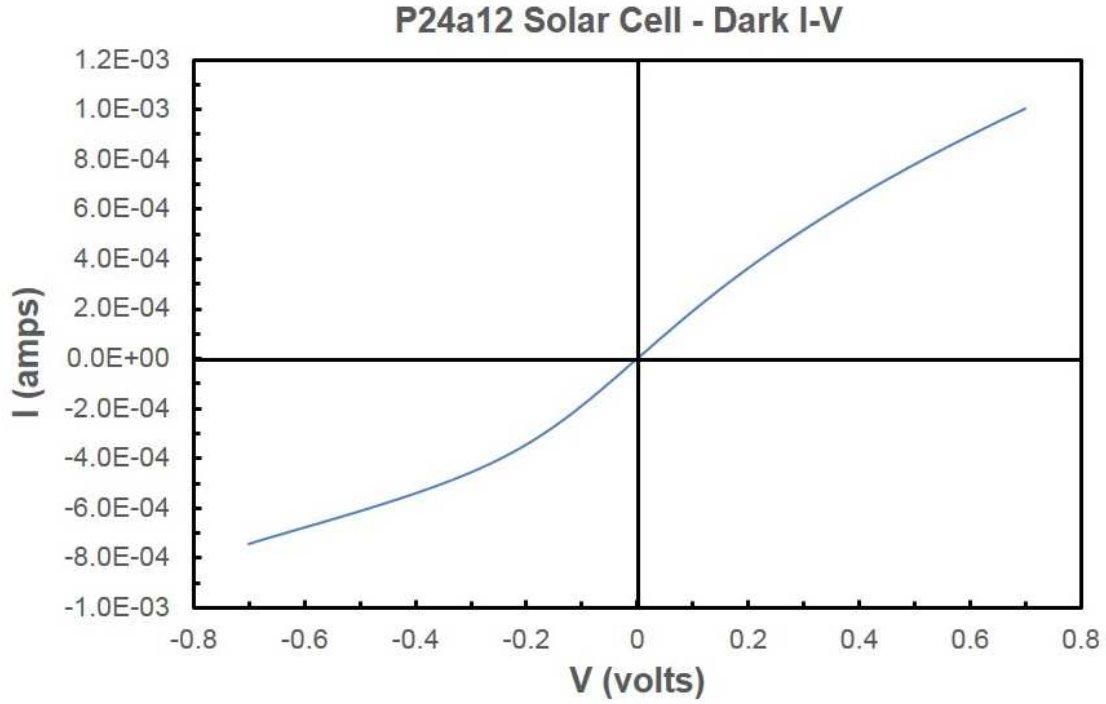
Figure 4:30: P24A12 Solar Cell Dark I-V
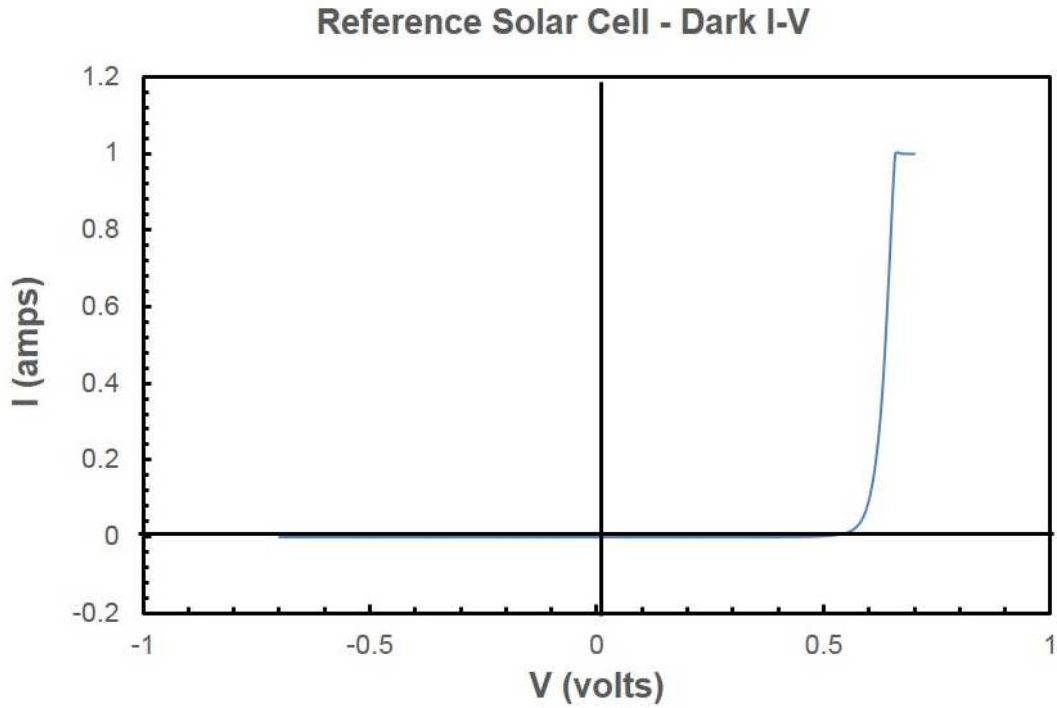
Figure 4:31: Reference Solar Cell Dark I-V

4.9. Crystal Structure

The characterization results demonstrate trends that may relate to various material models. The model must begin with crystalline silicon as this is the primary element. Crystalline silicon is formed in the diamond lattice configuration. To understand this configuration, a slightly simpler configuration, face-centered cubic (FCC), can be easily visualized and demonstrates the tight binding of atoms.

The FCC structure is the tightest crystal structure with an atomic packing fraction of 74%. The FCC crystal structure gives a perspective of how the unit cell will change the crystal structure of silicon. To achieve the diamond lattice of silicon from the FCC structure, four additional atoms are added to the unit cell in a tetrahedral configuration. The first pair are added in a plane that bisects the leftmost atom and the rightmost atom from top to bottom. The position of the left atom of the pair is centered between the top leftmost atom and the top center atom and down at an angle of 35.26°. The right atom of the pair is centered between the rightmost atom and the center atom and down 35.26°. This pair positioning is shown in Figure 4.32.

The second pair of atoms follow the same positioning as the first pair except on a plane rotated 90° from the first plane and bisecting the front most atom and rear most atom from top to bottom. The pair of atoms is positioned in a similar fashion except from the bottom of the unit cell. The front atom of the pair is positioned between the bottom front most atom and the bottom center atom and up 35.26°. The second atom of the pair is positioned between the bottom rear most atom and the bottom center atom and up 35.26°.

The positioning of the two pairs of atoms will change the size of the unit cell significantly. The atomic packing fraction of 74% of the FCC lattice will reduce to approximately 34% for the diamond cubic lattice structure resulting in a larger unit cell. The
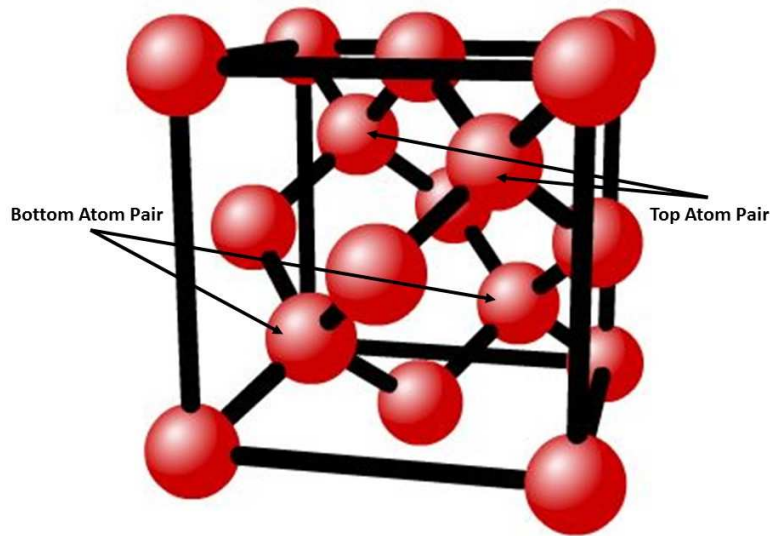
Figure 4:32: FCC Lattice with 4 Atoms Added

larger unit cell may be easily imagined as the atoms are squeezed into position as described above.

The final result of the diamond cubic lattice of crystalline silicon with a top view orientation is shown in Figure 4.33. The top view orientation enables a clear view of the two pair of atoms added to the FCC configuration and it is easily seen how the pairs lie in the planes with the alignment of the corner atoms as described above. In this view, the spacing between atoms is not to scale for the clarity of geometrical perspective.

The side view of crystalline silicon may now be more easily viewed with the proper geometrical perspective. An important realization of the crystalline silicon unit cell is the fact that the two pairs of atoms previously described are the only atoms fully contained within the unit cell. When calculating the atomic packing fraction, APF, the number of atoms contained in the unit cell must be known as shown in the relation for the atomic packing fraction in Equation below.
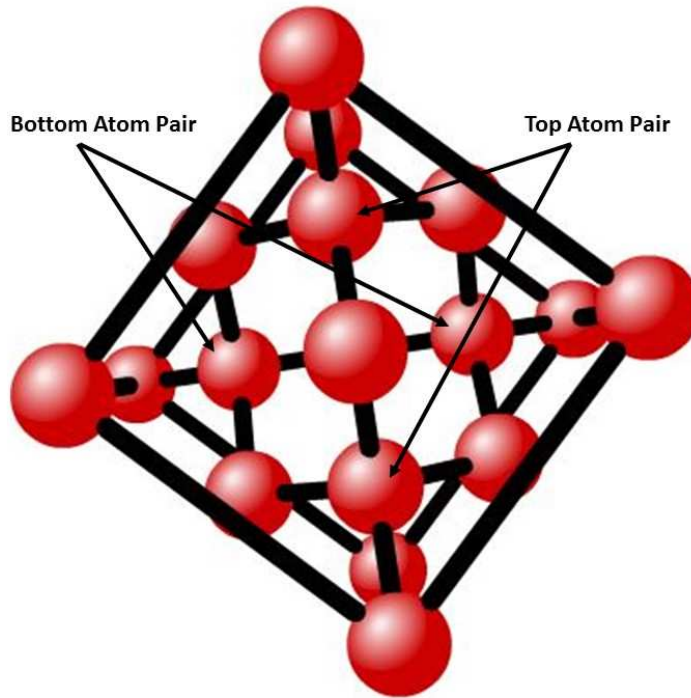
Figure 4:33: Top View Diamond Crystal Lattice

$$\text{APF} = \frac{Natoms * Vatoms}{Vcell} \qquad \text{(Equation 4.5)}$$

From Equation 4.5, N_{atoms} is the number of atoms contained in the unit cell. V_{atoms} is the

volume of the atom, which is the volume of a sphere, $(4/3)\,\pi\,r^3$, where r is the radius. V_{cell} is the

volume of the cell, which is the lattice constant cubed, a^3. For FCC crystal, the number of atoms

is 4, and the lattice constant is $2\sqrt{2}$ r. For silicon, the number of atoms is eight. This is

determined by the four fully contained, the six on each face that are half contained, and the eight

on the corners that are one-eight contained. The lattice constant is $(8\sqrt{3}/3)$ r. The side view of the

crystalline silicon lattice is shown in Figure 4.34.

The importance of recognizing the crystal structure of crystalline silicon is that any

changes made to the crystal begin from this configuration. The results of Hall measurements, X-
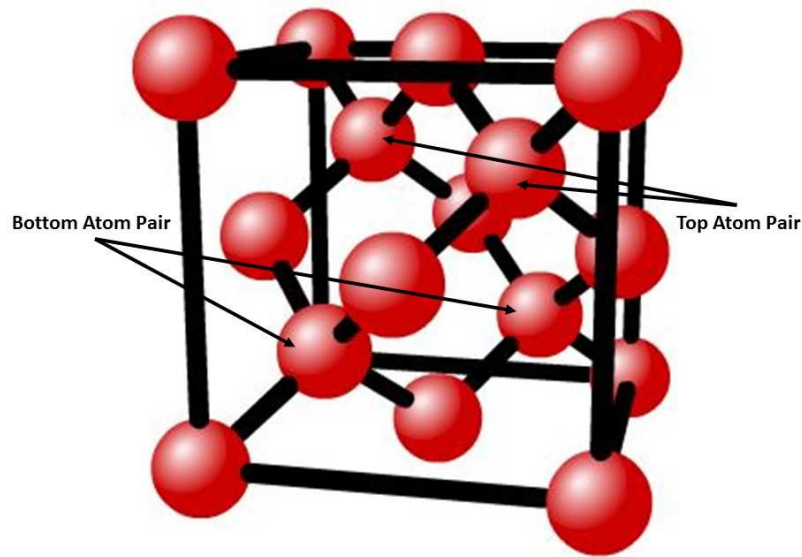
Figure 4:34: Side View of c-Si Lattice

ray diffraction characterization, Raman spectroscopy and spectroscopic ellipsometry are dependent on the crystal structure. With this understood, the next step is to understand what occurs when crystalline silicon is doped with phosphorus.

The process of doping the crystal with phosphorus is the replacement of at least one silicon atom in the crystal lattice with a phosphorus atom. Prior to the replacement of the silicon atom, the silicon atom has four valence electrons that are satisfied with each of the four covalent bonds. When the replacement occurs, the phosphorus atom with five valence electrons satisfies the same four covalent bonds, and the fifth electron is released as a free electron. This free electron makes the crystalline silicon n-type assuming no other change has occurred. Moreover, as the phosphorus is next to silicon in the periodic table of elements, it is easily known that the phosphorus atom is only about twenty percent smaller in size as the silicon atom. Because of this, the crystal lattice will have a small influence on its size. This configuration is demonstrated

with the replacement of one silicon atom in the bottom pair previously mentioned. The configuration is shown in Figure 4.35.
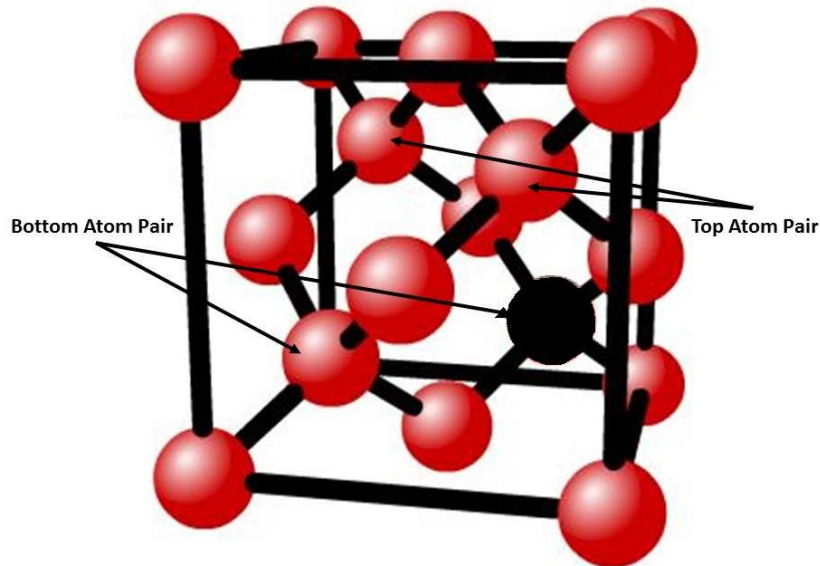
Figure 4:35: c-Silicon Lattice with One Phosphorus Atom

The configuration in Figure 4.35 is the replacement of one whole atom in a crystal lattice that contains eight atoms. If all unit cells within a material had this configuration, this would be a phosphorus concentration of 1/8 or 12.5%. In traditional growth methods, solid solubility limits the phosphorus concentration to 3.4%. To push the phosphorus concentration levels higher, non-traditional methods would have to be implemented.

The previous description of the crystal lattice configuration doped with phosphorus is a tetravalent configuration with the phosphorus at the center of the tetrahedral. This configuration is electrically activated with the release of a free electron, a process of phosphorus not naturally occurring. A more naturally occurring configuration of phosphorus is the trivalent bond that occurs with phosphine, PH_3. For a similar bond configuration to occur in the silicon crystal, a

pseudocubic lattice may form. It has been shown through first-principle calculations that a pseudocubic configuration will form the compound Si_3P_4. [19] This configuration is shown in Figure 4.36. In this configuration, each of the interior atoms is a phosphorus atom. Additionally, two face-centered atoms are removed as shown.
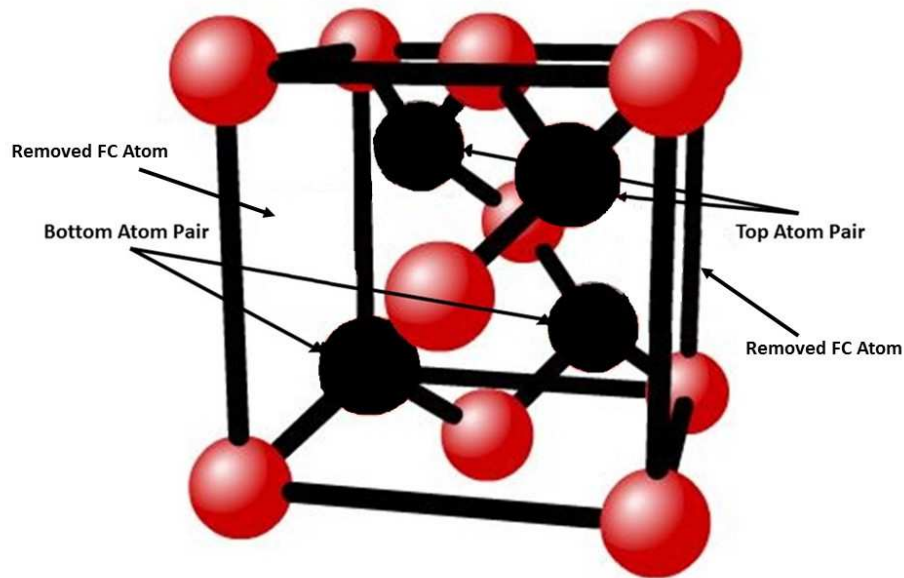
Figure 4:36: Pseudocubic Si_3P_4 Lattice [19]

The Si_3P_4 may form at multiple stages due to several characteristics. The electronic configuration of this molecule would have each silicon valence electron satisfied in a covalent bond and three of the phosphorous valence electrons satisfied in covalent bonds with silicon atoms and the remaining pair of valence electrons satisfied as a lone pair. This configuration would leave no free electrons and, therefore, no doping effect.

One model for the growth of the samples may include the formation of the Si_3P_4 molecule that precipitate from the diamond crystal form of crystalline silicon at the shift in trends that was noted in the Hall measurements. This would explain a decrease in charge carriers

as the phosphorus concentration was increased. Moreover, the spectroscopic ellipsometry results may also be explained by Si_3P_4 nanocrystalline being formed which added to the broadening of the peaks of the index of refraction.

5. Summary

The optical and electrical characteristics of highly-phosphorous doped silicon films were investigated while gaining many new skills and knowledge of semiconductor characterization technology. This new material approached new limits of low resistivity while maintaining a high level of crystallinity.

Characterization technology encompasses many tools and techniques. For this work, Hall measurement, X-ray diffraction, electrochemical capacitive-voltage profiling, Raman spectroscopy, photoluminescence characterization, and spectroscopic ellipsometry were the primary methods of characterizing phosphorus doped samples. A model was described that may explain the behavior of the new material and may lead to future research.

In addition to characterizing and analyzing the samples, a device constructed from the samples was simulated, fabricated, and characterized. The solar cell device was compared to similar material solar cells for a general comparison to reveal any new effect caused by the highly-phosphorous doped samples.

References

1   http://www.nanowerk.com/news/newsid=1452.php (Accessed 30 March 2015)

2   T. Ghani, M. Armstrong, C. Auth, M. Bost, P. Charvat, G. Glass, M. Bohr. (2003, December). "A 90nm high volume manufacturing logic technology featuring novel 45nm gate length strained silicon CMOS transistors." In Electron Devices Meeting, 2003. IEDM'03 Technical Digest. IEEE International (pp. 11-6). IEEE.

3   S. Chopra, Z. Ye, A Zojaji, Y. Kim, S. Kuppurao. "Heavily Phosphorus Doped Silicon Junctions for NMOS Applications". ECS Trans., 13 (1) 307-312 (2008).

4   Z. Ye, S. Chopra, R. Lapena, Y. Kim, S. Kuppurao. "High Tensile Strained In-Situ Phosphorus Doped Silicon Epitaxial Film for nMOS Applications." ECS Transactions 50.9 (2013): 1007-1011.

5   http://www.dawgsdk.org/crystal/ (Accessed 10 March 2015).

6   K.D. Weeks, S.G. Thomas, P. Dholabhai, J. Adams. "Characterization and analysis of epitaxial silicon phosphorus alloys for use in n-channel transistors". Thin Solid Films, 520 (2012) 3158-3162.

7   J. D. Plummer, M.D. Deal, P.B. Griffin. (2000) Silicon VLSI Technology, (1st Edition). (pg. 376) Upper Saddle River, NJ. Prentice Hall Publishing.

8   C.S. Smith, "Piezoresistance effect in germanium and silicon." Physical review 94.1 (1954): 42.

9   S.E. Thompson, G. Sun, Y.S. Choi. "Uniaxial-process-induced strained-Si: extending the CMOS roadmap." Electron Devices, IEEE Transactions on 53.5 (2006): 1010-1020.

10 S. Werner, U. Belledin, A. Kimmerle. "Doping-and carrier concentration profile characterization of highly phosphorus-doped emitters." Proceedings of the 25th European Photovoltaic Solar Energy Conference and Exhibition, Valencia, Spain. 2010.

11 https://www.memsnet.org/mems/processes/deposition.html, LPCVD. (Accessed 21 March 2015).

12 http://www.probion.fr/en/94-tutoriaux/144-ecvp-tutorial (Accessed 28 December 2014).

13 http://www.renishaw.com/en/a-basic-overview-of-raman-spectroscopy--25805 (Accessed 6 January 2014)

14 S.A. Al Ghetmiri, Nano Science and Engineering Institute, University of Arkansas, "Raman spectroscope setup," private communication, 2014.

15 J.A. Woollam Company, 645 M Street, Suite 102, Lincoln, NE

16 https://nationalmaglab.org/about/around-the-lab/what-the/faraday-cage. (Accessed 12 January 2015).

17 http://www.jawoollam.com/tutorial_1.html, (Accessed 12 January 2015)

18 Silvaco, Inc., 4701 Patrick Henry Drive, Bldg. 2, Santa Clara, CA

19 M. Huang, Y.P. Feng, ATL Lim, JC Zheng. "Structural and electronic properties of Si_3P_4." Physical Review B 69.5 (2004): 054112.

20 M.R. Zzchariah and C.F. Melius, "Theoretical calculation of thermochemistry for molecules in the Si-PH system," The Journal of Physical Chemistry A, vol. 101, pp. 913-918, 1997.

21 N. Hong, Ph.D., J.A. Woollam Company, Private Communication, October 9, 2014

Appendix A: Description of Research for Popular Publication

The need for new materials to sustain the technology revolution is at an all-time high. New materials for the foundational CMOS technology have been developed that may aid in continuing the revolution as predicted by Moore's law, an observation that has proven to be a predictor of an increase in the number of transistors in integrated circuits about every two years. Heavily phosphorus-doped silicon films have been produced by the ASM America Company claiming a phosphorus content beyond the solid solubility limit and resistivity levels below 0.3 mΩ-cm.

The claims of the heavily phosphorus-doped silicon films require many characterization techniques for confirmation and discovery of new properties of the material. Dr. Hameed Naseem, a professor in Electrical Engineering at the University of Arkansas, and master student Larry Cousar set out to characterize and analyze the new material of heavily phosphorus-doped silicon. In this work, Hall measurement, X-ray diffraction, Raman spectroscopy, photoluminescence, and spectroscopic ellipsometry characterization techniques were utilized for the discovery of electrical, optical, and material properties of the new material.

Hall measurement was utilized for identification of carrier concentration, resistivity, Hall mobility, and material n or p type. Results revealed carrier concentrations as high as 1.35×10^{21} cm^{-3} and resistivity as low as 0.23 mΩ-cm. Hall results were plotted versus phosphorus concentration and what resulted was far from expected. A dramatic shift in the carrier concentration trend as phosphorus increased was seen between six and seven percent.

Photoluminescence characterization revealed a similar shift in trend as seen in Hall measurement. Resolutions below 0.2 nm allowed for comparison of photoluminescence peaks

with respect to phosphorus concentration and a trend shift unexpected between six and seven percent.

Raman spectroscopy revealed, in samples with film thickness greater than 90 nm, Raman peaks indicative of possible silicon phosphorus bonds. Such Raman peaks are possible due to high content and crystallinity of some type of silicon phosphorus material.

Spectroscopic ellipsometry revealed possible nanocrystalline material as explained by increased UV absorption. Nanocrystalline material may explain trend shifts seen in carrier concentrations in Hall measurement and energy shift in photoluminescence characterizations. The result of Hall measurements with trends is shown in App. A Figure 1.
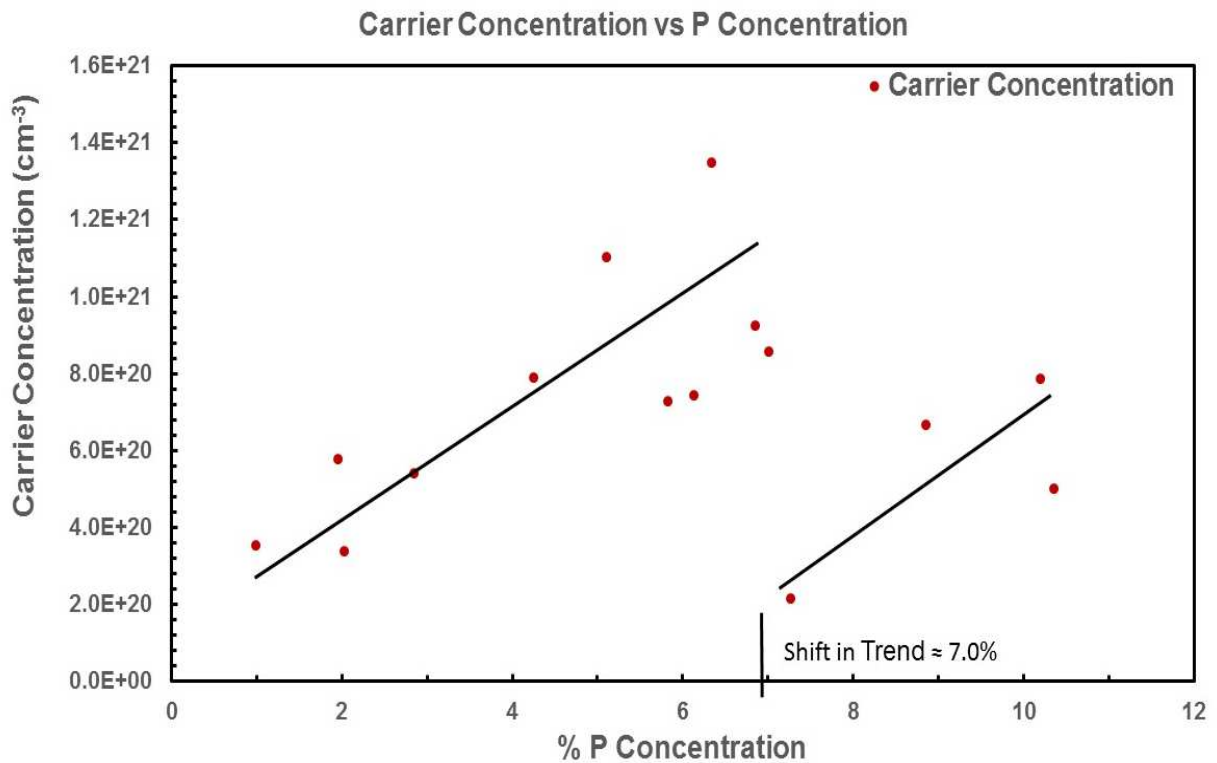
App. A Figure 1: Carrier Concentration vs. Phosphorus Concentration

Appendix B: Executive Summary of Newly Created Intellectual Property

The following item of new intellectual property items were created in the course of this research project.

1. The fabrication of a solar cell with a heavily-phosphorus doped silicon emitter on silicon substrate.

Appendix C: Potential Patent and Commercialization Aspects of listed Intellectual

Property Items

There are no potential patent and commercialization aspects of the listed intellectual property

item.

C.1 Patentability of Intellectual Property (Could Each Item be Patented)

There is no patentability of intellectual property in this research.

C.2 Commercialization Prospects (Should Each Item Be Patented)

There is no commercialization prospect in this research.

C.3 Possible Prior Disclosure of IP

There is no possible prior disclosure of IP in this research.

Appendix D: Broader Impact of Research

D.1 Applicability of Research Methods to Other Problems

Material growth and characterization is a standard process used in the electronic industry to move technology forward. This work used many characterization tools to identify physical, electrical and optical characteristics of the silicon phosphorus alloy. In addition to the characterization tools, a device was simulated, fabricated, and characterized to possibly expand the understanding of the new material. This method of research expands the standard process of research on electronic materials by seeking to fabricate a device that has applicability to current technology needs. The implementation of such methods may propel other areas of research to a more efficient method for problem solving.

D.2 Impact of Research Results on U.S. and Global Society

The new model described in this research may lead to the adoption of materials in CMOS technology that are less expensive and overcome barriers to CMOS feature size reduction. Additionally, the model may drive changes in material growth processes that may lead to new materials and devices for an even greater impact on technology.

D.3 Impact of Research Results on the Environment

The materials and processes used in this work are well researched materials with less impact on the environment than other exotic materials such as group III-V and other materials such as cadmium telluride.

Appendix E: Microsoft Project for MS MicroEP Degree Plan

		Task Mode	Task Name	Duration	Start	Finish	F
24			◢ **Write Thesis**	293.45 days	Mon 12/23/13	Tue 2/3/15	1
25			Chapter 1: Background of area	21 days	Mon 9/1/14	Mon 9/29/14	1
26			Chapter 2: Description of Experime	14 days	Mon 10/6/14	Thu 10/23/14	2
27			Chapter 3: Results	20 days	Mon 11/3/14	Wed 12/24/14	2
28			Chapter 4: Analysis	10 days	Mon 12/23/13	Tue 1/6/15	2
29			Chapter 5: Conclusion	10 days	Tue 1/6/15	Tue 1/20/15	2
30			Appendix	10 days	Tue 1/20/15	Tue 2/3/15	2
31			◢ **END GAME**	62.55 days	Mon 3/2/15	Tue 5/26/15	2
32			Review by Major Professor	2 wks	Mon 3/2/15	Fri 3/13/15	
33			Correct issues found	2 days	Mon 3/16/15	Tue 3/17/15	3
34			Send Title, Abstract & Scheduling II	1 day?	Mon 3/16/15	Mon 3/16/15	
35			Final approval by Major Professor	1 day	Thu 3/19/15	Thu 3/19/15	3
36			QC by μEP Director - permission to	1 day	Fri 3/20/15	Fri 3/20/15	3
37			Send thesis to committee member	1 day?	Mon 3/23/15	Mon 3/23/15	
38			Last Day for Public Presentation Ev	1 day	Mon 3/23/15	Mon 3/23/15	
39			Last day for Defense Before Comm	1 day	Tue 3/31/15	Tue 3/31/15	3
40			Graduate School Dead Line	0 days	Fri 4/24/15	Fri 4/24/15	
41			Dead Day	0 days	Fri 5/1/15	Fri 5/1/15	
42			Graduate	0 days	Sat 5/9/15	Sat 5/9/15	

Appendix F: Identification of All Software Used in Research and Thesis Generation

Computer #1:

       Model Number: x86-64Full_14S

       Serial Number: Dell 1707FP

       Location: ENRC

       Owner: Department of Electrical Engineering

Software #1:

Name: Microsoft Office 2013

Purchased by: Department of Electrical Engineering

Computer #2:

       Model Number: Laptop-Satellite A205-S5000

       Serial Number: 58247671K

       Location: Mobile

       Owner: Larry Cousar

Software #1:

       Name: Microsoft Office 2013

       Purchased by: UA Department of Electrical Engineering

Software #2:

       Name: Origin Pro 9.1 Student Version

       Purchased by: Larry Cousar

Software #3:

       Name: X'pert View XRD viewer

       Purchased by: Larry Cousar

Appendix G: All Publications Published, Submitted and Planned

There are no publications published for this thesis.

Appendix H: Silvaco Atlas Device Simulation Code

The code for the Si:P Solar Cell is shown in Table 6 below.

Table 6: Si:P Solar Cell Simulation Code

```
# Simulation of Si:P Solar Cell

# Si:P Solar Cell

go atlas

# Start mesh.  The AUTO parameter indicates that we will

# not specify y mesh lines directly but they will be inferred

# from the region specifications.

mesh auto

x.mesh loc=0.0 spacing=0.2

x.mesh loc=1.0 spacing=0.2

# This device will contain only 1 region of silicon

# bounded on top and bottom by ITO electrodes.

region material=Silicon

elec num=1 name=anode   y.max=0.05          material=ITO

elec num=2 name=cathode y.min=0.30 y.max=0.35 material=ITO

# Here we define a P-i-N diode.

doping uniform conc=1e14 n.type

doping gaus peak=0.05 char=0.01 conc=1e18 p.type dir=y

doping gaus peak=0.30 char=0.01 conc=1e18 n.type dir=y

# Here we override some of the default silicon parameter with
```

Table 6: Si:P Solar Cell Simulation Code (continued)
parameters that describe Si:P material.
material mat=Silicon mun=20 mup=1.5
material mat=Silicon nc300=2.5e20 nv300=2.5e20
material mat=Silicon eg300=1.9
Here we override some of the default silicon parameter with
parameters that describe SiP material.
material mat=Silicon imag.index=SiP_imaginary real.index=SiP_real
#material mat=Silicon taun=1e-6 taup=1e-6
Here we indicate that the default complex index of refraction for
ITO will use the data from the Sopra database
material mat=ITO sopra=Ito2.nk
#tonyplot
We include recombination models
models srh auger
Here we specify the optical source. In this case
we illuminate the device from above using normal
incidence (angle=90 default). We also indicate
that we will use the transfer matrix method to
model the optical propogation.
beam num=1 x.o=0.5 y.o=-2.0 AM1.5 verbose tr.matrix
Turn on the sun.
solve b1=1.0

Table 6: Si:P Solar Cell Simulation Code (continued)
We collect the IV characteristic to a file
log outf=solarex02_0.log
solve vanode=0.0 name=anode vstep=0.025 vfinal=1.2
We perform extraction of useful figures of merit
extract init infile="solarex02_0.log"
extract name="Jsc" y.val from curve(v."anode", i."anode") where x.val=0.0
extract name="Voc" x.val from curve(v."anode", i."anode") where y.val=0.0
extract name="P" curve(v."anode", (v."anode" * i."cathode")) outf="solarex02_3.log"
extract name="Pm" min(curve(v."anode", (v."anode" * i."anode")))
extract name="Vm" x.val from curve(v."anode", (v."anode"*i."anode")) \where y.val=$"Pm"
extract name="Im" $"Pm"/$"Vm"
extract name="FF" $"Pm"/($"Jsc"*$"Voc")
extract name="Eff_Si:P" 1e8*$Pm/0.1
#tonyplot
Silicon
go atlas
Start mesh. The AUTO parameter indicates that we will
not specify y mesh lines directly but they will be inferred
from the region specifications.
mesh auto
x.mesh loc=0.0 spacing=0.2
x.mesh loc=1.0 spacing=0.2

Table 6: Si:P Solar Cell Simulation Code (continued)
This device will contain only 1 region of crystalline silicon
bounded on top and bottom by ITO electrodes.
region material=Silicon
elec num=1 name=anode   y.max=0.05 material=ITO
elec num=2 name=cathode y.min=0.30 y.max=0.35 material=ITO
Here we define a P-i-N diode.
doping uniform conc=1e14 n.type
doping gaus peak=0.05 char=0.01 conc=1e18 p.type dir=y
doping gaus peak=0.30 char=0.01 conc=1e18 n.type dir=y
Here we override some of the default silicon parameter with
parameters that describe silicon phosphide material.
material mat=Silicon mun=20 mup=1.5 nc300=2.5e20 nv300=2.5e20 eg300=1.9
Here we indicate that the default complex index of refraction for
ITO will use the data from the Sopra database
material mat=ITO sopra=Ito2.nk
In this case we define defect states in the bandgap as would
exist in silicon materials.
defects nta=1.e21 ntd=1.e21 wta=0.033 wtd=0.049 \
We include recombination models
models srh auger
Here we specify the optical source. In this case
we illuminate the device from above using normal

Table 6: Si:P Solar Cell Simulation Code (continued)
incidence (angle=90 default). We also indicate
that we will use the transfer matrix method to
model the optical propogation.
beam num=1 x.o=0.5 y.o=-2.0 AM1.5 verbose tr.matrix
Turn on the sun.
solve b1=1.0
We collect the IV characteristic to a file
log outf=solarex02_1.log
solve vanode=0.0 name=anode vstep=0.025 vfinal=1.2
We perform extraction of useful figures of merit
extract init infile="solarex02_1.log"
extract name="Jsc" y.val from curve(v."anode", i."cathode") where x.val=0.0
extract name="Voc" x.val from curve(v."anode", i."cathode") where y.val=0.0
extract name="P" curve(v."anode", (v."anode" * i."cathode")) outf="solarex02_4.log"
extract name="Pm" max(curve(v."anode", (v."anode" * i."cathode")))
extract name="Vm" x.val from curve(v."anode", (v."anode"*i."cathode")) \
extract name="Im" $"Pm"/$"Vm"
extract name="FF" $"Pm"/($"Jsc"*$"Voc")
extract name="Eff" 1e8*$Pm/0.1
####tonyplot
Plot a comparison of the results with and without defects

Table 6: Si:P Solar Cell Simulation Code (continued)
tonyplot -overlay solarex02_0.log solarex02_1.log -set solarex02_0.set
Plot the defect states.
tonyplot solarex02_2.log -set solarex02_1.set\
Plot the power curves.
tonyplot -overlay solarex02_3.log solarex02_4.log
quit